COMPUTATIONAL ANALYSIS OF CODE-MULTIPLEXED COULTER SENSOR SIGNALS

A Dissertation
Presented to
The Academic Faculty

by

Ningquan Wang

In Partial Fulfillment
of the Requirements for the Degree
Doctor of Philosophy in the
School of Electrical and Computer Engineering

Georgia Institute of Technology
August 2021

COMPUTATIONAL ANALYSIS OF CODE-MULTIPLEXED
COULTER SENSOR SIGNALS

Approved by:

Dr. A. Fatih. Sarioglu, Advisor
School of Electrical and Computer
Engineering
Georgia Institute of Technology

Dr. David V. Anderson
School of Electrical and Computer
Engineering
Georgia Institute of Technology

Dr. Albert B. Frazier
School of Electrical and Computer
Engineering
Georgia Institute of Technology

Dr. Pamela T. Bhatti
School of Electrical and Computer
Engineering
Georgia Institute of Technology

Dr. Hang Lu
School of Chemical and Biomolecular
Engineering
Georgia Institute of Technology

Date Approved: April 26, 2021

To me

To my beloved family

ACKNOWLEDGEMENTS

I wouldn't have been able to finish my Ph.D. study without the support of the people who have helped me and inspired me during my Ph.D. life at Georgia Tech. I want to thank all of them.

First, I would like to express my deepest thanks to my advisor Prof. A. F. Sarioglu, who provided me research guidance and life principles. What I have learned from him will be my lifetime treasure and will definitely benefit my future career.

I would also like to give my appreciation to all my colleagues and friends at Georgia Tech. I shared my happiness and anxiety with them, and they encouraged me to go through the hard times. I hope we can all be lifetime friends.

Finally, I want to especially thank my family, who supported my decision to pursue a Ph.D. and gave me strength when I was trying to give up. Without your love, I could not finish this journey.

TABLE OF CONTENTS

LIST OF TABLES

LIST OF FIGURES

SUMMARY

A lab-on-a-chip (LoC) is a system that integrates laboratory functions on a single integrated circuit of only millimeters to a few square centimeters to achieve the same analysis that traditionally takes place in biological laboratories. Nowadays, LoC technology has been applied in a variety of applications because of its capability to perform accurate microscale manipulations of cells for point-of-care diagnostics. On the other hand, such a result is not readily available from an LoC device and typically still requires a post-inspection of the chip using traditional laboratory equipment such as a microscope, negating the advantages of the LoC technology.

To solve this dilemma, we have developed portable and disposable biosensors for interfacing with and digitizing the information from an LoC system. Our sensor platform, named Microfluidic CODES, integrated with multiple microfluidic impedance sensors, electrically monitors and tracks spatially-manipulated cells on a microfluidic device. The sensor platform compresses information from each sensor into a 1-dimensional electrical waveform, and therefore, further signal processing is required to recover the readout of each sensor. To achieve this multiplexing, we specifically design each sensor to produce a distinct sensor waveform and implement advanced signal processing techniques to extract information of detected cells like size, speed, and sensor identity (location).

My doctoral research mainly focuses on designing sensor multiplexing schemes and signal processing algorithms for the implementation of the Microfluidic CODES sensor platform. Currently, I have mainly developed three signal processing schemes for

this sensing technology. The first one is based on template correlation, the second one is based on the error-correction technique, and the third one is based on deep learning.

Thanks to the fast signal processing speed and high accuracy, the deep learning-based sensor platform also enables real-time cell measurements. Based on this, I also build a microfluidic feedback control system so that one could monitor and optimize the processing state within a microfluidic device.

Finally, through collaboration, I have employed computational tools I developed to build integrated microfluidic cytometers that characterize cell properties such as cell mechanical properties, cell membrane antigens, and cell surface expressions. These integrated microfluidic cytometers have the potential to enable various point-of-care assays for biomedical purposes.

CHAPTER 1.   INTRODUCTION

Over the past decades, the advancements in fabrication technologies have driven the miniaturization of microchips to the point they are ubiquitously available and increasingly pervasive in daily life. While the integrated circuits such as computer microprocessors, where billions of transistors are integrated onto a millimeter-square chip, are at the forefront of this revolution, it also leads to the development of Lab-on-a-Chip (LoC) systems, where nanoliters of samples are processed in lithographically-defined microfluidic channels essentially to perform the same analysis that traditionally takes place in biology laboratories. By performing a variety of plumbing processes such as fluid transport, mixing, separation, cell sorting, or heating on the chip, LoC systems have been applied in applications, such as point-of-care diagnostics [1], genomic research [2], on-chip immune tests [3], analytical chemistry assays [4], and environmental monitoring [5].

1.1   Microfluidic Devices for Cell Discrimination

At the heart of numerous LoC-based sample analysis are accurate microscale discriminations of cells within microfluidic devices. A typical microfluidic device is engineered to screen a heterogeneous population of cells and discriminate them based on a contrast in their biophysical or biochemical properties. As such, tracking spatially segregated cells (i.e., to detect the locations of the cells on the device) offers a way to identify detrimental cells or pathogens that may be mixed with normal cells in a sample to diagnose a disease. In fact, microfluidic devices are so efficient in identifying cells of different origin, they have been demonstrated to isolate a single cancer cell admixed with

1

billons of blood cells from the blood samples of cancer patients for early detection of cancers [6].

1.1.1   Cell Discrimination based on Biophysical Properties

Cell discrimination by biophysical properties, such as size, shape, mechanical property, and electrical property, are promising areas for real-time disease diagnostic and other biomedical applications [7]. Most of these discriminations use label-free approaches, which don't require antibody labeling or expensive chemical reagents, thus reducing sample preparation time while improving throughput and cell viability [51].

Size has been widely used as a biomarker for cell discriminations. Size-based cell separation is especially attractive as studies have reported that cancer cells are larger in size as compared to other hematologic cells [8]. Therefore, differences in cell size can be used for cancer cell selection without the knowledge of target cells' biochemical characteristics. Several methods have been introduced for size-based cell discrimination, including membrane filtration [7], inertial separation [9], deterministic lateral displacement (DLD) [10], pinched flow fractionation [11]. Size-based cell discrimination has been used for biomedical applications including isolation of leukocyte [12], plasma [13], CTCs [14], and waterborne pathogens [15].

Shape is another property for cell discriminations. For example, cancerous cells are morphologically characterized by large nucleus, having irregular sizes and shapes [16]. This is because in the development of cancer, alterations in the cell DNA give cells a property called pleomorphism, causing cells with different shapes and sizes. The main

method developed for shape-based cell discrimination is DLD [17]. Shape-based cell discrimination has been used for the isolation of bacteria [18] and RBCs [19].

The mechanical characterization of single cells is also an essential point for understanding cell properties. For example, mechanical property has been reported to be correlated with pathophysiological states in diseases, such as malaria and cancer. One of the methods developed for mechanical property-based cell discrimination is the DLD [17]. Hydrodynamic sorting [20] with constriction structures is also developed for the same purpose. Mechanical property-based cell discrimination has been used for the differentiation of HeLa cells [21] and CTCs [6].

Single-cell size-independent electrical properties, such as specific membrane capacitance and cytoplasm conductivity, are also intrinsic cellular parameters for evaluating the status of cells [22]. Therefore, cell electrical properties have emerged as promising electrical indicators for cell status evaluation. The main method developed for electrical property-based cell discrimination is dielectrophoresis (DEP) [23][24]. In a DEP system, force is induced on a dielectric particle when it is placed in a non-uniform electric field. In this situation, cells are polarized, and experience a corresponding translational force, called DEP force, which could further deflect cells. The polarization of a cell depends on its electrical properties, which can be characterized by the deflection of cells. Electrical property-based cell discrimination has been implemented in several biomedical applications including isolation of cancer cells [25], bacteria [26], pathogens [27], and immune cells [28].

Several other cell biophysical properties have also been used for cell discriminations, including density, compressibility, and intrinsic magnetic properties. Acoustophoresis-based cell discrimination [29][30] uses cell density and compressibility to distinguish different cell types and has been used, as an example, to distinguish CTCs and WBCs [31]. Specifically, in an acoustophoresis system, a force field provided by an acoustic source is implemented across a microfluidic chamber, and high-intensity sound waves interact with the chamber to generate pressure gradients that push cells into specific spatial locations. The magnitude of the force depends on the density and compressibility of the cell. As for intrinsic magnetic properties, applications have been demonstrated to separate RBCs and WBCs based on their distinct magnetic properties [32].

1.1.2   Cell Discrimination based on Biochemical Properties

Cell biochemical properties feature various cell surface markers (essential proteins or carbohydrates) involved in a variety of cell functions [33][34]. For example, surface antigens of a cell play an important role in the interactions with other cells and therefore serve as key biomarkers for pathological/physiological analysis [35]. As different cell types usually express different surface expressions, one can use cell surface markers as fingerprints to identify and classify cells. Furthermore, as the expression of cell surface markers keeps changing at different stages of a cell, one can also use cell surface markers to estimate cell stages [36]. Generally, a wide range of applications can be performed if one can identify cell surface markers or even manipulate cells based on surface markers. Currently, microfluidic biochemical properties-based cell discrimination can be categorized into fluorescence-activated cell sorting (FACS) [37], magnetic-activated cell sorting (MACS) [38], and affinity enrichment (biopanning) [39].

4

In traditional FACS, the target cells are first labeled with antibody-linked fluorescent dye [51]. Then an optical detection system is used to identify specific fluorescent markers, which is only presented in target cells. Whenever a target cell is identified, the cell is electrostatically deflected to a collection. FACS can be incorporated in a microfluidic device by implementing a switching mechanism to manipulate and sort individual cells instead of electrostatic charging and defection. Microfluidic-based FACS has been applied in hematopoiesis [40], oncology [41], and stem cell biology research [42].

Similar to FACS, MACS is also an antibody-labeled approach to enrich a cell subpopulation of interest in a heterogeneous mixture based on magnetophoresis [188][189]. Specifically, target cells are labeled with magnetic beads that are functionalized with antibodies specific to their membrane antigens. Immunomagnetically labeled cells are then differentially displaced in a microfluidic chamber under an external magnetic field based on their specific magnetic load. While magnetophoresis is typically employed for binary separations (i.e., magnetically labeled cells from unlabeled cells), separation of cells into multiple subpopulations based on their magnetic loads has also been demonstrated [43]. Microfluidic-based MACS has also been used in other cancer-related research [44][190].

Affinity enrichment is a cell isolation method where target cells flow through a surface that is functionalized with antibodies [45]. Due to antibody coupling, target cells are captured and bonded on the surface. This process can be generally divided into four steps. First, corresponding surfaces are functionalized with antibodies. Second, target cells are captured and bonded on the surface. Third, other cells, including low-affinity ones and non-target ones are washed away from the surface. Last, the antibodies are recovered for

the next round of cell capturing. On the other hand, low capture efficiency and purity levels keep this method from being widely used [51].

Affinity enrichment can be readily incorporated with microfluidic devices for a range of applications for cell characterizations [46]. Multiple innovations have also been introduced in these applications for an improvement of capture efficiency and yield purity. For example, Kurkuri et al. achieved a capture efficiency between 80% to 90% for cancer cells [47]. In this work, microposts are used as functioning surfaces for an increased surface area. An alternate way to increase surface area is introduced by Mitchell et al [48]. In this work, E-selectin-coated Halloysite nanotubes (HNT) were attached to the capture surface to increase the area for CTC isolation from leukocytes. Other than cancer cells, microfluidic affinity enrichment has also been used for isolation of leukocyte [49] and hematopoietic stem cells [50].

Furthermore, captured cells can be released with aptamer functionalized surface, so that target cells can be isolated and extracted [51]. For example, Zhang et al., introduce a device for the isolation of *E. coli* from a mixture with different bacterial species [52]. After the capturing stage, they heat the surface, and aptamer biding is disrupted, and captured *E. coli* cells are released. Different adhesion strengths on different cells can also be used for cell sorting. Bussonie et al. introduce a technique in which they first use a device to capture HEK293 and A7R5 cells and then use a surface acoustic wave to detach the cells so that they can efficiently sort HEK 293 from A7R5 cells [53].

1.1.3   Hybrid Cell Discrimination Methods

6

Cell discrimination techniques that simultaneously exploit both biophysical and/or biochemical properties have also been developed. As each single cell discrimination method has its own advantages and disadvantages, combining different methods in a single device can enhance the cell discrimination capability by achieving a greater specificity, allowing us to isolate cells with more nuanced differences. Hybrid methods are commonly used for separating cell targets from a mixture of multiple cell types [51].

Applications integrating multiple cell discrimination techniques have been introduced for cancer cell isolations. For example, Karabacak et al. has developed a microfluidic device with three stages for CTC isolation from whole blood [54]. In the first stage, based on cell biophysical properties, DLD is used to isolate WBCs and CTCs from other blood cells, given the RBCs are high deformable and platelets are small in size. In the second stage, still based on biophysical properties, isolated WBCs and CTCs are lined up using an inertial focusing chamber. Finally, in the last stage, magnetophoresis is used to separate WBCs, which have been magnetically labeled, from CTCs. The last stage is based on cell biochemical properties.

Still using hybrid methods for CTC isolation, Chu et al. have developed a monolithic 3D printed device with two compartments for the negative enrichment of CTCs directly from whole blood samples [55]. The first compartment consists of a stack of 32 microfluidic layers for leukocyte depletion based on the common leukocyte antigen (CD45). In the second compartment, based on the cell size differences between nucleated and anucleated cells, a micropore filter membrane is used to remove anucleated cells while retaining nucleated (CTCs) cells on the filter efficiently. This device combines

immunoaffinity capture of leukocytes and microfiltration to negatively enrich CTCs from clinically relevant volume of whole blood samples.

Applications integrating multiple cell discrimination techniques are also developed to isolate other types of cells. For example, Huang et al. have developed a technology for separating immature RBCs (NRBCs) from the blood of pregnant women [56]. In their device, the first stage, based on size contrast, separates NRBCs and WBCs from mature RBCs, and the second state performs separation on WBCs and NRBCs based on cell intrinsic magnetic properties. In another example, Kim et al. combine dielectrophoresis and magnetophoresis to separate three different strains of *E. coli* bacteria. In this work, Strain A bacteria were tagged with polystyrene beads and deflected away by DEP forces. Strain B bacteria were tagged with treptavidin-coated magnetic particles and captured by a magnet. Finally, Strain C bacteria, the unlabeled target, were isolated [57].

1.2   Sensing Systems for Microfluidic Devices

While highly effective in performing cell discriminations, microfluidic devices often lack a native sensing scheme and hence often act as upstream sample preparation elements prior to quantitative measurements, typically performed with off-chip sensing instruments such as an optical microscope [58] or a flow cytometer [59]. This disconnection between microfluidic manipulations and quantitative measurements is an important factor hampering the widespread adoption of these potentially revolutionary tools as quantitative assays outside of academic research laboratories, for example, in resource-limited or in point-of-care settings, where they can be truly transformative in healthcare delivery. An alternative sensing approach is on-chip sensing through integrated

sensors [60][61]. Capitalizing on the development of microfabrication techniques, integrated sensors with different sensing modalities can be patterned and integrated inside a microfluidic device, removing the need for bulky and expensive external hardware.

1.2.1   Off-chip Sensing

One of the most widely used methods for off-chip sensing is the image-based inspection of the microfluidic device, which has been implemented in a number of biomedical applications [62][63][64]. The image-based method creates a magnified image of a sample. This process generally consists of three steps. First, the sample is illuminated by a light source. Second, a compound of lenses, typically with an objective lens and an eyepiece, are used to magnify the sample image. Third, magnified sample images are brought to a detector, such as complementary metal-oxide-semiconductor (CMOS) cameras or charge-coupled devices (CCD). Image-based methods have been widely used in determining the growth status and growth rate of live cells [65][66][67], allowing for monitoring of individual cells over an extended period of time. On the other hand, during this process, excessive amounts of data are generated. To efficiently and accurately process these imaging data, an image processing algorithm can be designed and used. Heo et al. develop an image-based technology for label-free single-cell analysis [68]. In their work, a microscope and a high-speed camera are used to capture cell images and a deep learning-based image processing algorithm is introduced to classify K562 cells and human RBCs. In another work presented by Praljak et al. [69], sickle RBCs are automatically identified from high-resolution images captured by a microscope.

Fluorescence imaging is another widely used method for off-chip sensing. Fluorescence detection features its good selectivity and sensitivity [70]. In a fluorescence detection system, samples pass through an excitation source, and fluorescent emission is detected using optical sensors [71]. A variety of excitation sources can be used, such as a focused laser beam or scattered light. Laser-induced fluorescence system is most easily adapted to the dimensions of microfluidic devices. The reason is that the coherence and low divergence of a laser beam make it easy to focus on very small structures and to obtain high irradiation [72]. The light-based excitation system is less expensive but more flexible alternative in terms of the choice of the wavelength. The fluorescent analysis is so versatile and applicable that it has become a significant technique for detecting and analysis of different biomolecules. A recent work introduced by Guo et al. uses a fluorescence-based microscope to detect proteins [73]. In their work, ZnO nanowires are integrated inside microfluidic devices for enhanced fluorescence detection. Another example of using fluorescence detection on protein is introduced by Challa et al. [74]. In their work, proteins and protein complexes are visualized and sized in real-time. Other than protein, fluorescence-based detection has also been used for the detection of cells [75], virus [76], and DNA [77].

Acoustic sensing relies on the reflection of the acoustic wave (e.g., high-frequency ultrasound) from the sample to be detected. In such a system, the ultrasonic signal is measured by an external ultrasonic transducer. From the reflected signal spectrum from the particles, one could acquire particle information such as size and count. This technique can also be implemented on streaming parties, such as cell flowing in a microfluidic channel. With acoustic sensing, multiple applications have been developed for sample

characterization. Komatsu et al. have introduced a diagnostic method that uses high-frequency ultrasound (30 MHz) to measure polystyrene particles with two diameters (80 μm and 100 μm) [78]. The reflected spectrum from the particles shows local maximum values at either 80 μm or 100 μm, indicating the effectiveness of the technology on size characterization. Other examples include a direct quantification of analyte concentration by resonant acoustic profiling developed by Godber et al. [79] and photoacoustic flow cytometry developed for CTC detection [80].

Flow cytometry is another off-chip sensing technique that provides rapid multi-parametric analysis of particles in solution. A modern flow cytometer can analyze suspended particles at a rate of 50000 particles per second [82]. In a conventional flow cytometer, lasers are utilized to produce light signals that can be read by detectors such as photodiodes or photomultiplier tubes [81], and particles are driven through the laser beam on a one by one basis. Given this requirement, a particle concentration process is generally needed to avoid coincidences and interferences between particles. Therefore, given the capability in sample manipulation and focusing, microfluidic devices are perfect tools as an upstream sample-analyzing stage for flow cytometry [82]. For example, as shown by Oakey et al., inertial particle focusing is effective for flow cytometry analysis [83]. The authors in this work present a staged channel design consisting of both curved and straight sections that order particles into a single streamline, and they demonstrate excellent measurement precision and resolution from standard flow cytometry. Other than inertial focusing, flow cytometry also show effectiveness in combining with microfluidic devices that perform DEP [84] and hydrodynamic focusing [85].

Even though off-chip sensing features powerful equipment, the implementation of these external instruments comes with the penalty of bulkiness and high cost from the equipment, negating the portable and affordable advantages of microfluidic devices.

1.2.2 On-chip Sensing

On-chip sensing features integrated sensors that sense and detect samples within a microfluidic device. Much like the microfluidic devices themselves, the low cost, portable, and flexible nature of on-chip sensing make it an optimal interrogation technique for microfluidic devices. Based on the mode of sensing, microfluidic on-chip sensing can be mainly classified into electrical sensing [96], optical sensing [86], magnetic sensing [89], and mass spectrometry (MS) [92].

For on-chip optical sensing, CMOS image sensors (CIS) can be integrated within a microfluidic system, so that sample information can be optically measured within a microfluidic device [86][87]. However, most of these systems suffer from low resolution as there is no optical lens, and therefore, further image processing techniques, such as super-resolution (SR) processing, are required to recover the information. Huang et al. have introduced a lensless microfluidic imaging system, which directly integrates a microfluidic channel on a small CIS, and a white light source is used to illuminate the system from above [88]. In their work, to further enhance the low-resolution images captured by the CIS sensor, they have introduced a deep learning model to understand the correspondence between a low-resolution image and its high-resolution counterpart. Specifically, a low-resolution lensless cell image is processed by a trained deep learning model and a high-resolution cell image is outputted. The experimental results showed that the cell resolution

is improved by 4x. The system further enables lensless blood cell imaging and counting and the cell counting results matched well with a commercial flow cytometer.

Magnetic sensing is another commonly-used on-chip sensing technique. For example, the magnetoresistive (MR) sensor, also called a spin-valve sensor, is a type of magnetic sensor that can be integrated into microfluidic devices [89]. The integrated MR sensor is composed of a non-magnetic metal layer between two ferromagnetic metal layers. One of the ferromagnetic metal layers (the pinned layer) has its magnetization fixed by an adjacent antiferromagnetic layer, and the other one (the free layer) is free to rotate. When magnetic beads (or particles labeled with magnetic beads) flow through the area of the sensor, a corresponding change in the magnetic field results in a rotation of the free layer, which in turn causes the change of the sensor resistance. Integrated MR sensors have been applied to several applications. Albuquerque et al. have developed integrated MR sensors for the detection and monitoring of colorectal cancer [90]. In this work, MR sensors are coupled to a portable platform to detect carcinoembryonic antigen (CEA), which is a commonly used blood biomarker for colorectal cancer detection and stage monitoring in the clinical setting. Their detection reaches a sensitivity level of nanograms per milliliter. Low throughput is a common problem for MR sensors. To solve this limitation, Loureiro et al. developed an MR-based cytometer [91], which not only counts, but also determines the magnetic orientation, flowing height, and speed of single micron-sized magnetic beads moving with velocities of 8–35 mm/s.

Mass spectrometry (MS) is a technique that measures the mass of a molecule by measuring the mass-to-charge ratio of its ion [92]. MS allows the ionization of intact molecules to obtain a highly accurate molecular weight, making the identification of

molecules easier. The high sensitivity and selectivity make MS become an important analytical tool for the analysis of biomolecules. Multiple applications of integrating MS into microfluidic devices have been developed. Hardouin et al. have introduced a microfluidic device coupled with ion trap MS for the identification of protein [93]. The device can be used for identifying protein biomarkers, even expressed in very low levels. Other MS systems are also introduced. An LC-ESI-MS system is developed by Armenta et al. for multiple proteins detection from breast cancer cellular extract [94]. A chip-liquid chromatography LC-MS system is developed by Horvatovich et al. for label-free profiling of human serum [95].

Among all the on-chip sensing techniques, one of the most flexible sensing modalities is electrical sensing. Compared to other aforementioned sensing methods, electrical sensing is simple, easy to integrate into microfluidic devices, doesn't require particle labeling, and has a high throughput. These electrical sensors, also called Coulter counters [96], electrically detect impedance variations caused by suspended particles, transducing cell information into electrical signals that can be readily interpreted. This sensing scheme that Coulter counters employ is called resistive pulse sensing (RPS). In the original setting of an RPS system, a pore-bearing membrane is placed between two electrolyte-filled chambers. When the cells of interest, initially suspended in one of the chambers, are driven across the membrane through the pore, the electrical impedance is modulated. The number and sizes of cells can be determined from the number and the amplitudes of the intermittent changes in the electrical current, respectively. Coulter counters excel at rapid enumeration and sizing of suspended cells and therefore find widespread use in different applications such as hematology [97], oncology [96],

microbiology [99], pathology [100], pharmacology [101], industrial applications [102], and environmental monitoring [103].
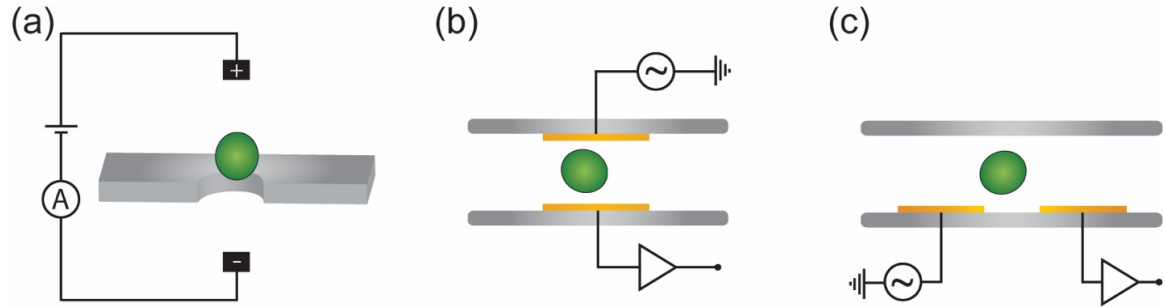
Figure 1 - Realization of the RPS scheme within a microfluidic system. (a) A pore structure. (b) Microfluidic channel with parallel electrodes. (c) Microfluidic channel with coplanar electrodes.

Through microfabrication techniques, the RPS scheme can be readily incorporated within a microfluidic system. One realization example is the use of a pore structure [104]. In such a device, an electric field is applied across a membrane with a micropore. The transient drop in the cross-membrane electric current is measured upon the translocation of particles through the pore (Figure 1a). Another realization of the RPS scheme is the use of microfluidic channels and electrodes. In such a device, suspended particles pass through microfluidic channels and interact with electrodes (parallel or coplanar) that provide the electric field (Figure 1b, 1c). The impedance variation in the sensing region of the microfluidic channel is detected by the electric field, and the corresponding electrical readout is acquired. Microfluidic Coulter counters have been implemented in the detection and analysis of cells [105][106], DNA molecules [107][108], proteins [109], and viruses [110].

1.3 Monitoring of Microfluidic Cell Discrimination with Integrated Sensors

When microfluidic devices differentiate cells into different locations based on their biophysical or biochemical properties, a spatiotemporal tracking of the manipulated cells (e.g. determining the microfluidic channel/chamber they are sorted into or the location where they are captured) transforms microfluidic devices into a flow cytometry performing various cellular and molecular assays. On the other hand, this spatiotemporal information is typically obtained through microscopic imaging of the chip, which constitutes a bottleneck in employing these microfluidic devices outside the laboratory. Therefore, a microfluidic device with integrated sensors that can spatiotemporally track manipulated particles can help realize a fully integrated, low-cost system that would especially be useful for analysis of samples in mobile and/or resource-limited settings.

Given the simplicity and flexibility of the electrical sensing modality, the Coulter counter would be an ideal choice for on-chip sensing. While a single Coulter counter provides a measurement at a single node on a microfluidic device, multiple Coulter counters, when allocated at different locations of interest, give a bigger picture of the device. At the same time, distributed Coulter counters also allow the monitoring of a microfluidic device with multiple layers, for which an optical sensor may not work well. For a microfluidic sensor network with multiple Coulter counters, an efficient multiplexing strategy among different sensors is a key issue to solve so that signals from each sensor can be acquired without increasing the complexity of external hardware. That is to say, we want to design a microfluidic device with multiple Coulter counters that share the same output channel so that we can monitor multiple nodes on the device without increasing the external hardware for signal acquisition.

16
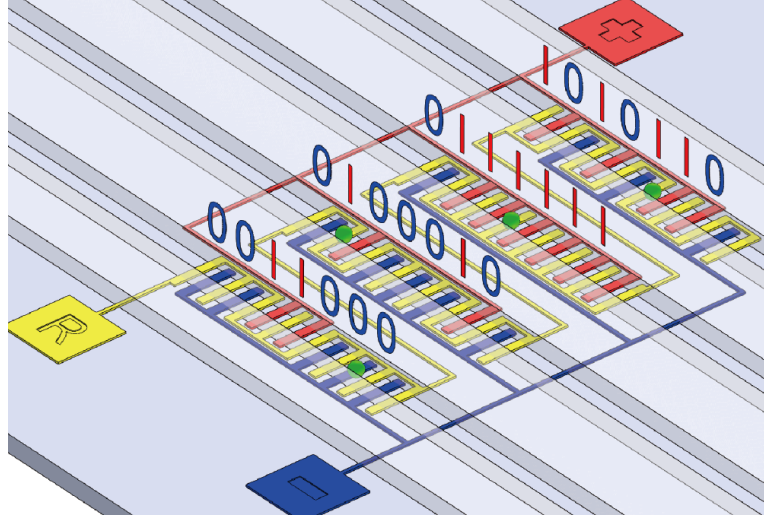
Figure 2 - Concept illustration of the Microfluidic CODES sensor platform. Coplanar electrodes are patterned to encode each sensor with a specific digital spreading code so that when cells pass through, each sensor produces a location-specific electrical signature waveform.

We have introduced a microfluidic Coulter sensor network, called Microfluidic CODES [111][112][113], that can transduce spatial manipulation of cells on a microfluidic device into an electrical signal in order to infer a variety of properties of a cell from its motion within the device. To multiplex distributed sensors in the network, we specifically design each sensor to produce a location-specific electrical signature waveform, similar to the principle of code-division multiple access (CDMA) [114], a spread spectrum telecommunications technique commonly used in telecommunication systems. In this case, by identifying these signature waveforms from individual measurement nodes through computational analysis of the sensor output, one can electrically track the motion of cells within the device in lieu of imaging for cytometric analysis. Specifically, to assign each distributed sensor a signature waveform, we micropattern coplanar electrodes so that different sensors have distinct underlying electrode patterns, following the specifically-designed digital spreading codes (Figure 2).

17
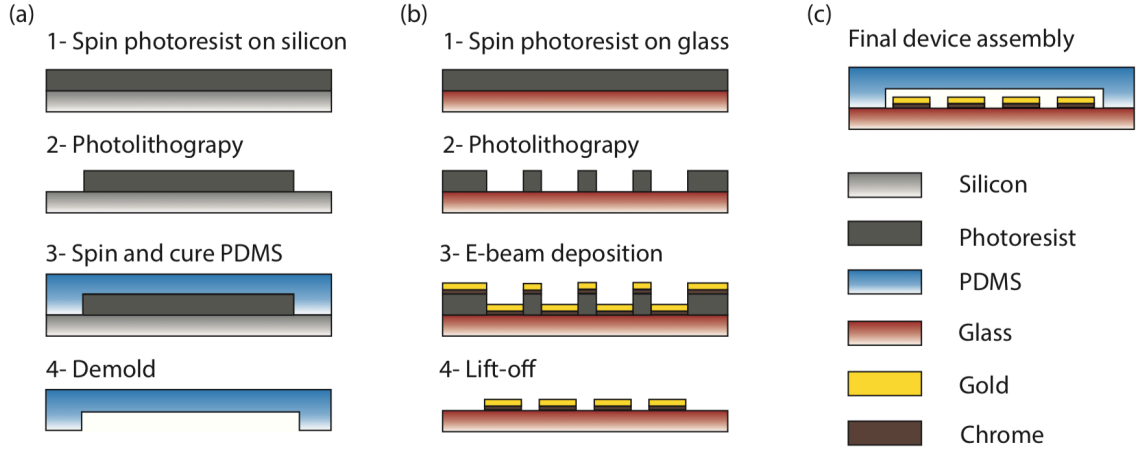
Figure 3 - Fabrication of the Microfluidic CODES device in terms of the (a) PDMS microfluidic layer, (b) surface electrodes layer, and (c) the final device.

The Microfluidic CODES device is composed of a glass substrate with micropatterned surface electrodes that generate digital codes and a polydimethylsiloxane (PDMS) microfluidic layer. We fabricate our device using conventional microfabrication techniques and soft lithography (Figure 3). We create surface electrodes on a glass wafer using a lift-off process. A 1.5 μm-thick negative photoresist is patterned using optical lithography followed by e-beam deposition of 20 nm-thick Cr and 80 nm-thick Au film stacks. The lift-off process is completed in acetone under mild sonication, and the patterned wafer is diced to create individual chips. The microfluidic layer is fabricated using soft lithography. A 15 μm-thick SU-8 photoresist is patterned on a silicon wafer using optical lithography to fabricate the mold. A PDMS prepolymer and crosslinker (Sylgard 184, Dow Corning) are mixed at a ratio of 10 : 1 and poured on the mold, degassed, and then cured at 65 °C for 4 hours. The Cured PDMS peeled off from the mold and glass substrate with surface electrodes are activated in oxygen plasma, aligned, and bonded to create the final device.

How reliably and rapidly the code-multiplexed information from the Coulter sensor network can be processed directly determines the capability of the technology. During this process, several challenges need to be solved. First, cells with different sizes will induce sensor waveforms with different powers, which can be analogous to the near-far problem in a telecommunication system. Second, multiple cells could simultaneously interact with the same sensor, causing same-sensor interferences, which can be analogous to the situation when a user signal in a telecommunication system can be reflected by buildings and reach the base station as an inference. Third, cells arrive at the sensing region randomly without any regulations, which can be analogous to the asynchronization between users in the telecommunication system.

Facing all of the above challenges, my Ph.D. work mainly focuses on designing signal multiplexing/demultiplexing schemes and algorithms for the Microfluidic CODES sensor platform and then applying Microfluidic CODES for biomedical applications. Given this purpose, this thesis is organized into the following chapters.

In CHAPTER 2, I explore literature on several categories of signal demultiplexing/separation algorithms, some of which are applied for the analysis of code-multiplexed Coulter signals. In Section 2.1, traditional signal multiplexing/demultiplexing techniques used in telecommunication systems are illustrated. In Section 2.2, several statistical signal separation algorithms are discussed. Section 2.3 focuses on deep learning-based signal separation methods.

In CHAPTER 3, I present different signal processing schemes for Microfluidic CODES sensor platforms that I developed. The first signal processing scheme of the

Microfluidic CODES utilizes a template-based correlation algorithm to increase accuracy in resolving interferences [111][112][113] (Section 3.1). The second signal processing scheme utilizes a built-in error correction signal for distributed Coulter sensing, relaxing sensor design constraints [115][116] (Section 3.2). The third signal processing scheme is based on a deep learning model, increasing design flexibilities and enabling real-time applications [117][118][119] (Section 3.3). Other than these, I have also investigated the application of independent component analysis (ICA) and frequency-division multiplexing access (FDMA) in the Microfluidic CODES technology [118] (Section 3.4 and Section 3.5).

In CHAPTER 4, I demonstrate an adaptive microfluidic system based on the Microfluidic CODES technology [121]. While conventionally, a microfluidic platform is typically designed to function under optimized conditions [122][123][124], which rarely account for specimen heterogeneity and internal/external perturbations, the introduced adaptive system will not only be less prone to artifacts due to sample heterogeneity, but also offer new capabilities for performing experiments/measurements under closed-loop controlled stimuli for basic research.

Finally, in CHAPTER 5, I demonstrate several Microfluidic CODES-enabled integrated cytometers that utilize the computational approaches that I developed. These applications include cell mechanophenotyping [125] (Section 5.1), cell immunophenotyping [126][127][128] (Section 5.2), and cell membrane antigen expression profiling [129]-[132] (Section 5.3).

CHAPTER 2.   LITERATURE SURVEY

2.1   Signal Multiplexing / Demultiplexing

Signal multiplexing is the process of combining information from multiple sources into a single signal. The advantage of signal multiplexing is that by transmitting a large number of signals with a single medium, we save transmission cost. Even though the transmissions occur on the same channel, they do not necessarily occur at the same instant/frequency. This gives us flexibility in how to combine different signals together. In this case, in order to transmit these signals over a common channel, it is essential to implement specific methods to keep these signals apart or separable to avoid permanent information loss, so that they can be further recovered at the receiving side, which performs signal demultiplexing based on the multiplexing strategy.

2.1.1   Time-division Multiplexing

Time-division multiplexing (TDM) [134][138] is the first version multiplexing scheme that has been developed and employed in real-life applications such as wired and wireless networks. In the TDM, at the transmitter side, signals from different sources are allocated over non-overlapping short time slots to share the same communication medium, and all the signals operate at the same frequency band. At the receiver side, by detecting and connecting distinct time slots, the desired signals can be recovered. As these time slots are small, data transmission appears to be parallel in this case.

One of the key problems to solve in TDM is the synchronization between the multiplexer (transmitter) and demultiplexer (receiver). The multiplexer and the

demultiplexer have to be properly synchronized so that there will be no cross-talk among different channels (signals). Therefore, synchronization bits are generally added at the beginning of each time frame as an indication, which also allows the demultiplexer to separate the incoming time slots accurately. Based on the corresponding synchronization strategy, TDM can be categorized into synchronous TDM and asynchronous TDM. Shortly, In the synchronous TDM, the time slots are arranged in a round-robin manner [136]. That is to say, if there are N source signals, then a single time frame consists of N time slots, no matter whether there is data from a particular source or not. This will cause empty time slots, which cause waste. On the other hand, asynchronous TDM is designed to overcome this limitation, where time slots are dynamically allocated on demand [137].

2.1.2   *Frequency-division Multiplexing*

In the frequency-division multiplexing (FDM) [133][135], the total frequency bandwidth available in a communication medium is divided into a series of non-overlapping frequency bands, and each source signal is allocated in a distinct frequency band. Therefore, even though all the source signals are transmitted within a single channel at the same time, ideally, no overlapping happens among them in the frequency domain. At the receiver side, the demultiplexer employs proper filters to extract the desired signal in each bandwidth. The extracted bandpass signals will be converted to baseband signals with further processes at destinations. FDM has been used in multiple applications, including the first generation of cellular telephones [139], cable television [140], and FM radio broadcasting [141].

FDM has several advantages. First, FDM is simple to set up, especially on the transmitter side. This kind of multiplexing is popularly used with many real-life applications mentioned above. FDM also is not sensitive to propagation delays that might happen in the transmission process. Furthermore, it allows maximum transmission link usage. On the other hand, in FDM, the need for filters at the receiver side results in expensive and complicated construct design. Also, as FDM is a technique for analog signal and analog signal has limited frequency range, implementation of linear amplifiers in FDM systems is sometimes necessary.

2.1.3   Code-division Multiplexing

Code division multiplexing (CDM) [114], also called the spread-spectrum technique, is a type of multiplexing technique in which the multiplexer encodes each source signal with a unique code (spreading sequence) that is generated by a pseudorandom sequence generator or other generators. In this process, a narrowband signal is spread over a large band of frequency, so CDM takes full advantage of the available spectrum. Encoded source signals share a common transmission channel and are decoded at the demultiplexer. To achieve that, the demultiplexer also needs to know the same spreading sequence used at the transmitter side.

Choosing a well-defined code plays a critical role in the spreading process. Mathematically, the similarity between two discrete spreading sequences is defined by the correlation between them. For optimal performance, the set of spreading sequences should be designed to be orthogonal. That is, the correlation between two spreading sequences (i.e., cross-correlation) is zero, while the correlation of the digital spreading code with itself

(i.e., autocorrelation) is maximized. Several well-established spreading sequence sets include the Gold code [142][191] and Walsh code [143].

Several developed demultiplexing schemes for CDM include parallel interference cancelation (PIC) [144], successive interference cancelation (SIC) [145]. Both of them are correlation-based algorithms, relying on the correlation property among encoded user information. In a standard correlation-based CDM detector, a matched filter bank [146][148] is implemented for all the users, and user information is estimated. For the PIC, given a specific user, the interferences produced by other users are simultaneously removed. For the SIC, given a specific user, the interferences produced by other users are removed in succession regarding the power of the component (starting from the strongest signal). Therefore, For the PIC, as compared with the SIC, the delay required to complete the whole operation is decreased. On the other hand, the SIC structure is not only simpler, requiring less hardware, but is also more robust in doing the cancellation [147].

2.2   Statistical Signal Separation

Statistical signal separation is the process of solving blind source separation (BSS) [149] problems using statistical methods. In a BSS problem, we separate a set of source signals from a set of mixed signals, without the need for information about the source signals or the mixing process. A classical blind signal separation problem is the so-called cocktail party problem, with N people in a room talking simultaneously to N different microphones. The goal is to recover each speech signal from the N microphone outputs. The human brain can handle this sort of auditory source separation problem, but it is a difficult problem in signal processing. Mathematically, a BSS problem can be modeled by

an n-dimensional random variable X=AS, where S is a vector whose coordinates are independent random variables corresponding to each people [150]. The objective is to recover the matrix A given random samples from X. Several methods have been developed to solve this problem.

2.2.1 *Independent Component Analysis*

Independent component analysis (ICA) is a computational technique for separating independent source signals from a mixed one, which is a linear combination of each source signal [151][152]. ICA attempts to find the underlying source signals by some simple assumptions of their statistical properties. First, the underlying source signals are assumed to be independent of each other, which is realistic if they correspond to distinct physical identities (like different persons). Second, it is assumed that each source signal has a non-Gaussian distribution, which is crucial for recovering the underlying components that created the data. Furthermore, ICA typically requires that the number of observations (mixed signals) is equal to or larger than the number of contained source signals.

ICA can be categorized into an unsupervised learning method as it takes the input data in the form of a single data matrix and does not necessarily know the desired output (or label) of the system [153]. This is in contrast to classical methods in regression or classification, where each data point needs to be labeled. In this way, ICA can be used to investigate the underlying structure. ICA has been used for the separation of artifacts in magnetoencephalography (MEG) data [154], finding hidden factors in financial data [155], and reducing noises in images [156].

2.2.2 *Principle Component Analysis*

Principal component analysis (PCA) [157] is a technique for reducing the dimensionality of high-dimensional datasets, increasing interpretability but at the same time minimizing information loss. More specifically, given a dataset, PCA finds the component vectors that explain the maximum amount of variance by N linearly transformed components. In this case, the first principal component is the projection on the direction in which the variance of the projection is maximized. PCA can be used to reduce the dimension of data to remove unwanted components in the signal. By using a few components, each data point can be represented by fewer numbers of variables (instead of maybe thousands of variables). Data points can then be plotted, making it easier to visually assess similarities and differences between data points. In practice, PCA has been implemented in areas such as image processing [158], quantitative finance [159], and neuroscience [160].

Mathematical derivation shows that PCA can be performed as the solving of an eigenvalue decomposition problem (EVD) or, alternatively, from the singular value decomposition (SVD) of the centered data matrix [161]. PCA can be based on either the covariance matrix or the correlation matrix. SVD is a widely used technique to decompose a matrix into several component matrices, exposing useful properties of the original matrix, including rank and singular value.

2.2.3 Non-negative Matrix Factorization

Non-negative matrix factorization (NMF) methods have received a lot of attention in the audio processing community, particularly because of their good performance in solving signal separation problems and their ability to automatically extract sparse and

26

interpretable factors [162]. In NMF, using low-rank matrix approximation, an input matrix X is factorized into two sub-matrices W and H, where X = WH. Each column of W is a basis element and is the fundamental building blocks from which we can reconstruct approximations to the original data. Each column of H is the coordinates of a data point in the basis defined by W. That is to say, H tells us how to reconstruct an approximation of an original data point from a linear combination of columns in W.

Traditional NMF algorithms consist of two separate stages. In the first stage, the training stage, a generative model is learned. In the second stage, the testing stage, the pre-learned model is used for a variety of high-level tasks. Currently, NMF has been used in applications including image processing [163], text processing [164], and audio processing [165].

2.3   Deep Learning-based Signal Processing / Separation

Machine learning (ML) is a key research area in data analysis and signal processing. Unlike model-based signal processing, ML focuses on providing a machine with the ability to learn from experience without being explicitly programmed. More specifically, ML-based algorithms update and optimize their internal parameters by learning from an existing dataset (training data) and make predictions on a future unseen dataset (testing data). Currently, ML has been widely used in areas including material science [199], computer science [200] and healthcare [201].

Among various ML models, deep learning is a popular learning model for complex pattern recognition tasks [202]. Deep learning is a representation learning method that is originally inspired by the biological neural network that constitutes human brains. Like the

vast network of neurons in a brain, a deep learning model, also named an artificial neural network (ANN), is based on a collection of interconnected nodes called artificial neurons. These artificial neurons make up multiple computational layers, and each layer performs a nonlinear transformation on the output of the previous layer. To draw an appropriate representation in each layer, the ANN uses the backpropagation algorithm to tune its internal parameters (weights), which are used to compute the representation. In this way, the input signal is approximated by a hierarchy of features from low level to high level layer by layer. Because of this nonlinear multilayer structure, deep learning has great potential in representing very complex functions and solving highly nonlinear problems [203][204][205]. Deep learning has been implemented in various signal separation tasks, including independent source number estimation [184], single-channel speech separation [183], music source separation [186], and image denoising [187].

The adoption of deep learning in processing sensor signals has gained much attention and development. Compared to traditional signal processing methods, deep learning models have a greater potential in signal modeling. Furthermore, the efficiency of deep learning structures also enables real-time applications. Currently, three categories of deep learning structures are commonly used for processing sensor signals, namely the feedforward neural network, the convolutional neural network, and the recurrent neural network.

2.3.1 Feedforward Neural Networks

A feedforward neural network (FNN), also known as a multilayer perceptron, is the simplest type of ANN and forms the basis of other ANN architectures [202]. In an FNN,

signals only flow forward, from the input layer, through the hidden layers, to the output layer. Each neuron in one layer performs a weighted summation of neuron values in the previous layer. Then a nonlinear function is applied to the summed value for a nonlinear activation.

To implement the FNN to process sensor signals, a feature extraction process is typically required, and extracted features are then used as the input to the FNN. Hu et al. have introduced an FNN for Electrocardiogram (ECG) signal classification [166]. To enhance the classification result, an adaptive multilayer perceptron structure is used for feature (QRS) detection. Extracted QRS complexes are further used for the ECG classification. Other feature extraction methods for sensor signals include wavelet transformation, Fourier transform, and independent component analysis. FNN has also been used in the study of Electroencephalography (EEG) signals such as EEG classification [167], brain tumor detection [168], and emotion detection [169]. FNN has also been used for signal separation problems [170].

2.3.2   Convolutional Neural Networks

The convolutional neural network (ConvNet) is often used when the input signal presents local saliences [202]. A typical ConvNet consists of several artificial neuron layers, including convolutional layers, activation layers, and pooling layers. The convolutional layer extracts local saliences and features from the input signal using multiple sliding feature detectors (kernels with specific weights). These kernels promise the ability of the ConvNet to be invariant to the transformation and shift of features in the input signal. After each convolutional layer, an activation layer is usually added,

introducing nonlinear properties to the model by applying a specific activation function. The pooling layers are usually placed in-between two convolutional layers. They successively down-sample and input signal, reducing the number of parameters and computations in the network. Pooling layers also give ConvNets the ability to detect features at different sizes.

A major advantage of the ConvNet compared with the FNN is that the ConvNet combines both feature extraction and pattern recognition into a single body. During the training process, each kernel in a ConvNet learns to extract optimized features directly from the input data. This scheme is extremely useful for unstructured input data such as electrical signals, images, and videos, where feature extraction and feature engineering can be troublesome. Examples of using ConvNets on sensor signals include hand gesture classifications from electromyographic (EMG) signals [171], diabetes predictions [172], and atrial fibrillation detection from ECG signals [173]. ConvNet has also been used for various of signal separation applications including monoaural audio source separation [174] and vocals and musical separation [175].

2.3.3 Recurrent Neural Networks

Stemming from the need for analyzing input data with sequential and temporal features, recurrent neural network (RNN) is one of the prominent research subjects in deep learning [202]. The RNN is distinguished by its "memory" as it can memorize information from previous predictions and use it for current and future predictions. Such a closed-loop setting in the network creates a feedback mechanism, allowing the model to make appropriate predictions based on a prior. Another advance that builds upon the RNN is the

long short-term memory (LSTM) [202]. An LSTM unit is typically composed of a cell, an input gate, an output gate, and a forget gate. These gates are highly effective in forgetting insignificant information, keeping relevant information, and conveying them to the next state. The LSTM solves several drawbacks of the traditional RNN structure, such as the exploding/vanishing gradient and limitation to short-term dependencies.

RNN has demonstrated great effectiveness in areas such as speech recognition, machine translation, handwriting recognition, and video understanding. Research has also been done in applying the RNN for biomedical sensor signals. Several ECG-related applications have been introduced [176][177]. Meanwhile, RNN has also been applied for processing EEG signals for depression prediction [178], epilepsy seizure detection [179], and sleep stage classifications [180]. RNN/LSTM has also been used for various of speech signal separation applications [181][182][183].

CHAPTER 3.   PROCESSING OF CODE-MULTIPLEXED SIGNALS

In the Microfluidic CODES sensor platform, each sensor in the network is formed by a distinctly-patterned array of coplanar electrodes and therefore produces a signal distinguishable from other sensors' when it detects a particle. As all the distributed sensors share a single electrical output, when multiple sensors activate at the same time (multiple cells occupy the sensing volume simultaneously), individual sensor waveforms (signature waveforms) interfere with each other, and a signal processing algorithm is required to further demultiplex sensor readout.

With the goal of designing algorithms with better performance, we have mainly introduced three signal processing schemes, namely the correlation-based processing, the error-correction-based processing, and the deep learning-based processing. We also investigated the implementation of FDMA and ICA in designing the algorithm.

3.1   Correlation-based Processing of Microfluidic CODES Signals

The first signal processing scheme for the Microfluidic CODES utilizes a correlation-based signal processing algorithm to decode sensor signals. The digital code for each distributed sensor is specifically designed to have good correlation properties, similar to the orthogonal digital spreading sequences used in traditional CDMA communication networks to differentiate between cell phone users. In this case, sensor signature waveforms can easily be distinguished through computation (correlation) even when they interfere with each other.

3.1.1   Hardware Design

3.1.1.1 Design of Orthogonal Digital Codes

We consider two aspects when designing the digital codes. First, they should be mutually-orthogonal. Second, they have good timing properties. As cells arrive at microfluidic channels at random times, our digital codes should work (maintain good correlation properties) even when they are misaligned with random phase shifts. In this case, while it is not possible to always maintain perfectly orthogonality, various quasi-orthogonal digital spreading sequences have been designed for telecommunication systems. Among these, Gold codes [142][189] are commonly used to minimize multi-user interference in CDMA communication since they have both desirable autocorrelation and cross-correlation properties. Therefore, in this work, we used Gold codes to encode distributed sensors.

We generated four 7-bit long Gold codes to encode four distributed sensors in our device. Since a full review of the mathematical framework to generate Gold codes is beyond the scope of this dissertation and can be found elsewhere [112], we therefore briefly outline our design process: First, we used two linear feedback shift-registers representing two primitive polynomials ($x^3 + x^2 + 1$ and $x^3 + x + 1$) to generate a preferred pair of 7-bit maximal length pseudorandom noise sequences (m-sequences). Second, cyclic shifts of the preferred pair of m-sequences (m1 = 1001011 and m2 = 1110100) were added in mod 2 to generate four distinct Gold codes, specifically g1 = 1010110, g2 = 0111111, g3 = 0100010 and g4 = 0011000. Finally, we validated the Gold codes by analyzing their autocorrelation and periodic cross-correlation properties (Figure 4).
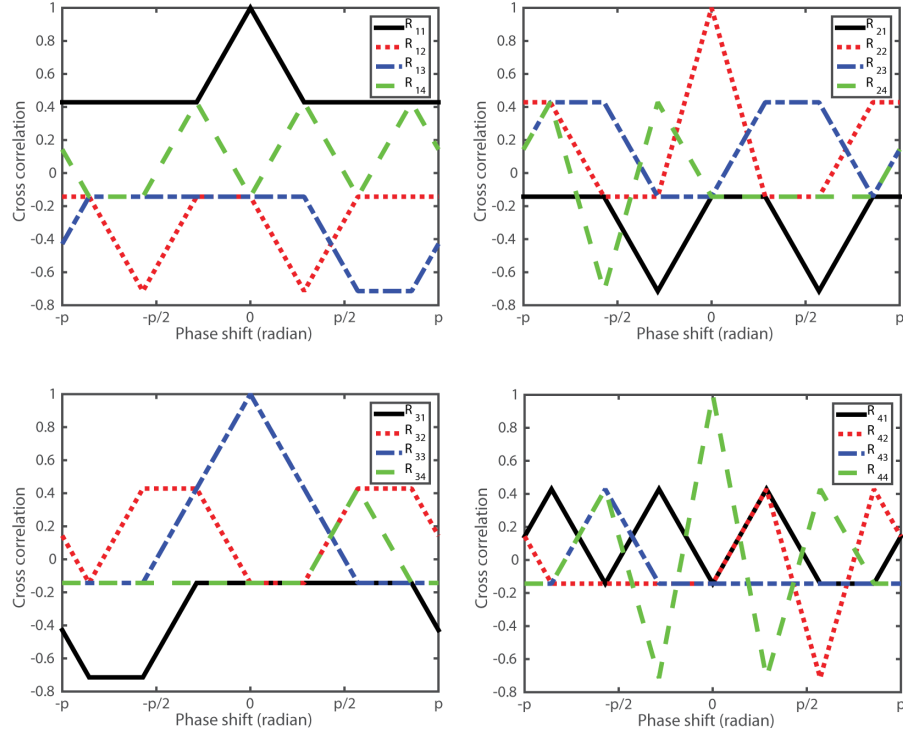
Figure 4 - Periodic auto- and cross-correlation of four 7-bit Gold codes. Auto-correlation peak can be identified when a code correlates with itself.

3.1.1.2   Design of the Microfluidic Device

As proof of principle, we designed a microfluidic device with four Coulter sensors, each of which was encoded by the aforementioned 7-bit long Gold code. In the device, three coplanar electrodes were micropatterned to construct the sensor. We first placed positive and negative electrodes on opposite sides of each microfluidic channel. These electrodes each extended into the microfluidic channel through 10 μm-wide electrode fingers. For each microfluidic channel, positive and negative fingers were ordered to follow the unique digital code. Second, the common electrode fingers were placed in between the positive and negative electrode fingers, leaving 10 μm-wide gaps between any two fingers. In this configuration, each bit spatially corresponds to a center-to-center distance between common electrode fingers, while the

electrode finger in between determined the bit polarity. Finally, to minimize undesired conduction in the microfluidic channels outside the coding region, we placed positive and negative electrode traces far from the outer common electrode fingers (Figure 5). A close-up view of the sensor structure is demonstrated in Figure 6.

Microfluidic CODES using correlation-based signal processing scheme is easily scalable. More sensors can be incorporated in the device when designed to produce output signals distinguishable from the rest. One way to expand the sensor network is to design sensors based on larger orthogonal code sets with longer digital codes. Longer orthogonal codes with more bits provide higher processing gain in decoding and can be distinguished from each other when there is interference. Based on this, we also designed a microfluidic device with 10 channels, each encoded with a 31-bit long Gold code (Figure 7, Figure 10, Figure 11).
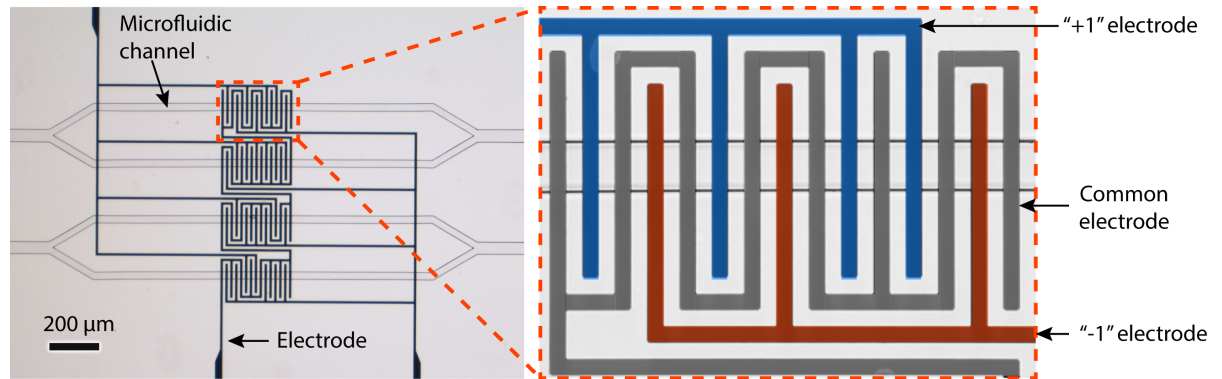
Figure 5 - Electrode design of the Microfluidic CODES using correlation-based signal processing scheme. Each sensor is encoded with a 7-bit Gold code. Left: Image of the electrode patterns on four channels. Right: We add different colors on different electrodes to demonstrate the sensing principle.
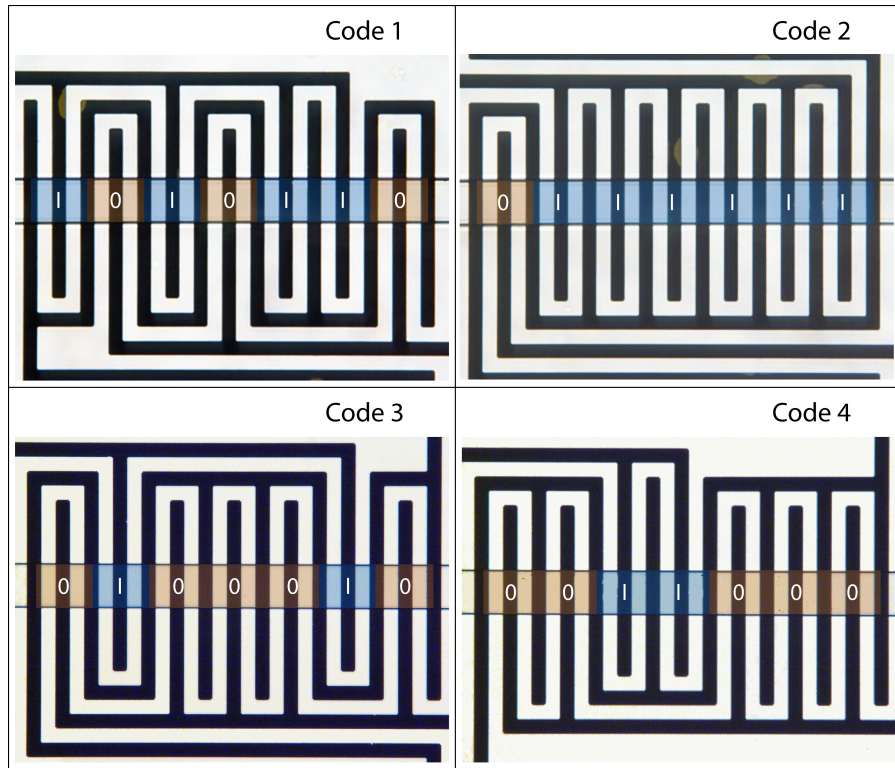
Figure 6 - Close-up image showing the structure and corresponding code of each sensor in the Microfluidic CODES. Code 1: 1010110; Code 2: 0111111; Code 3: 0100010; Code 4: 0011000.
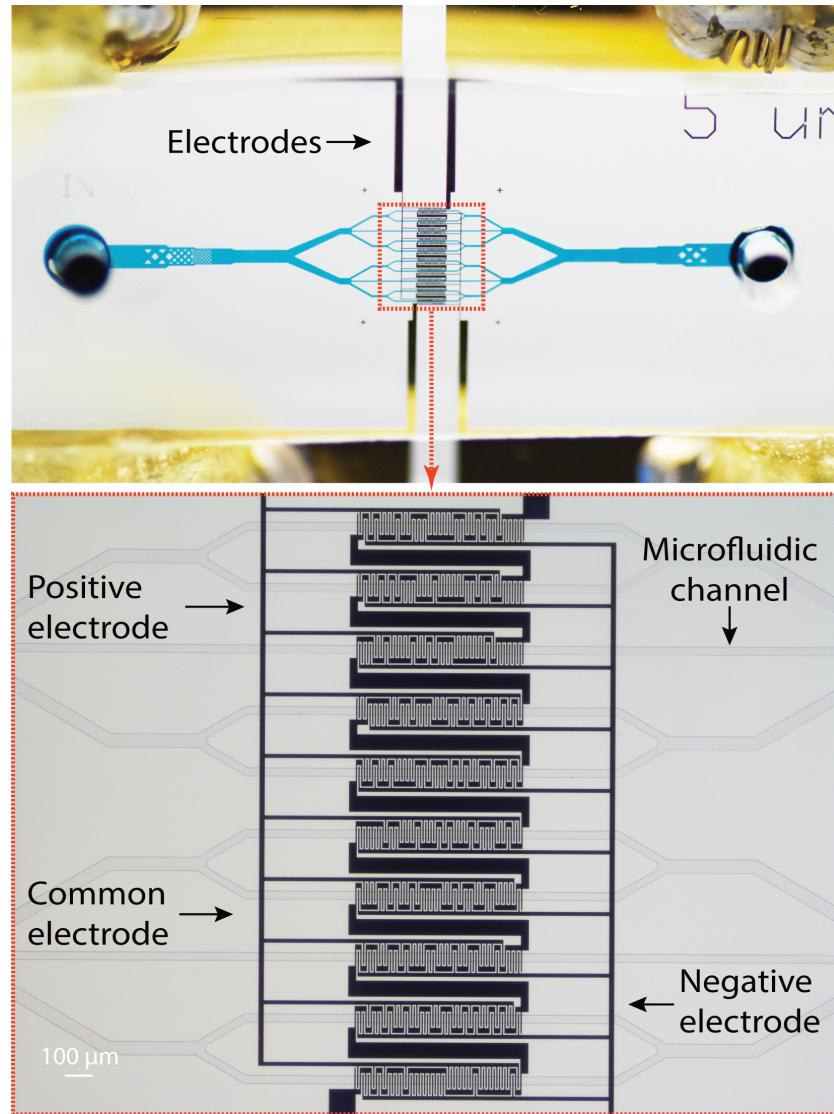
Figure 7 - Design and picture of the 10-channel Microfluidic CODES using correlation-based signal processing scheme. Each sensor is encoded with a 31-bit Gold code. Top: Picture of the 10-channel device. Bottom: Image of the electrode patterns on 10 channels.

Our experimental setup consisted of a syringe pump for driving the biological sample through the microfluidic chip, electronic hardware for data acquisition and processing of raw sensor signals, and an optical microscope equipped with a highspeed camera for the visual analysis of cell flow in the microfluidic channels (Figure 8).
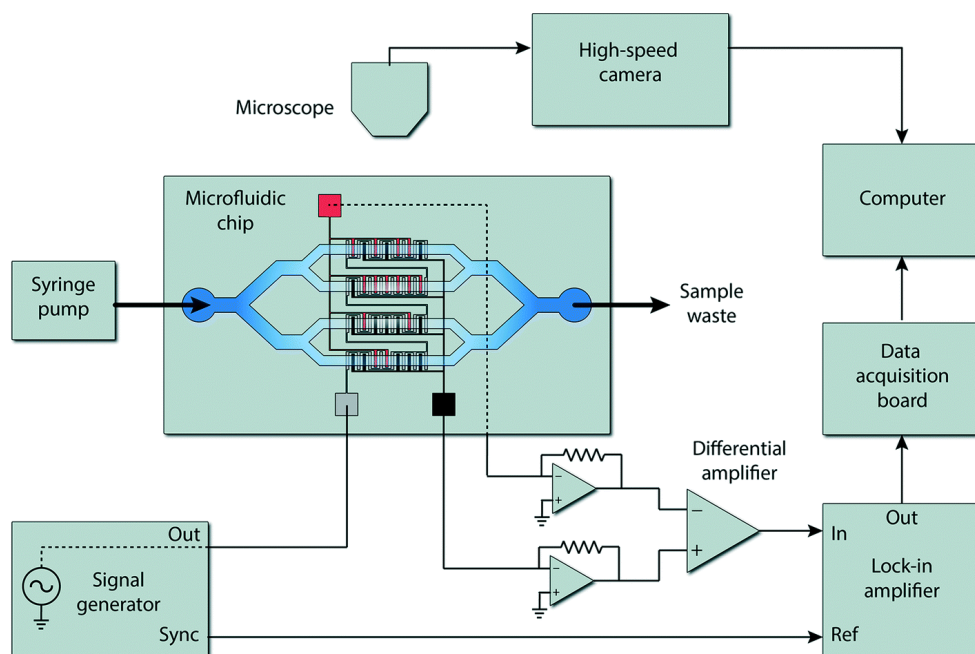
Figure 8 - Experimental setup for sensor characterizing in the Microfluidic CODES. Excitation signal is applied to the common electrodes, and the output signal is acquired from the sensing electrodes and followed a signal path comprised of transimpedance amplifiers and a differential amplifier. A lock-in amplifier is used to demodulate the signal.

A 400 kHz sine wave, specifically chosen to bypass the double layer capacitance at the electrode-liquid interface, was applied to the common electrodes to excite the Coulter sensor network, and the output signal was acquired from the sensing electrodes and followed a signal path comprised of transimpedance amplifiers and a differential amplifier. Specifically, the differential amplifier was used to subtract the positive electrode signal from the negative electrode signal so that the resultant electrical current would lead to positive peaks in the output. A lock-in amplifier (HF2LI, Zurich Instruments) was used to demodulate the signal, and the demodulated signal was sampled into a computer with a sampling rate of 1M Hz for processing.

38
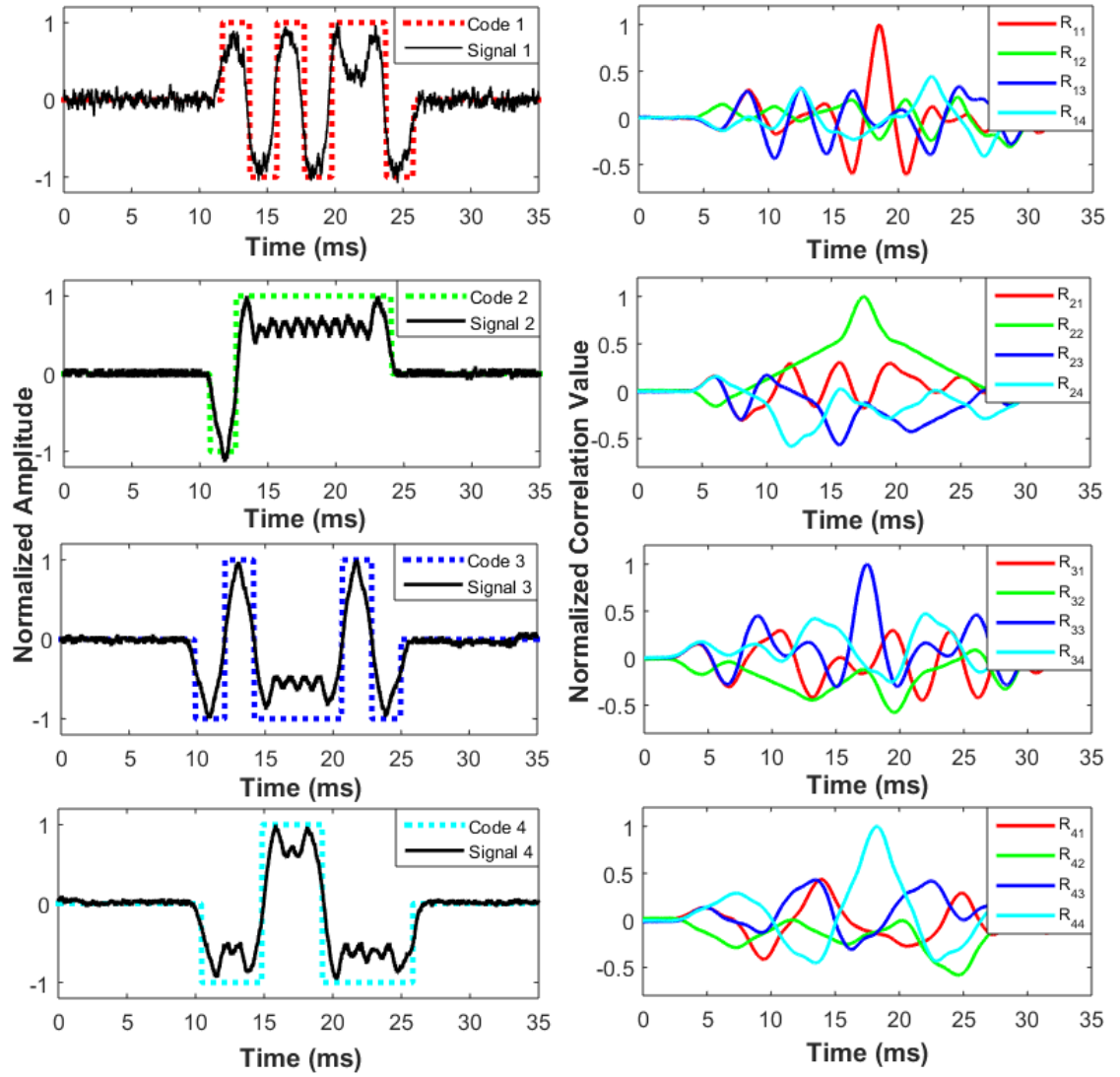
Figure 9 - Measured electrical signals (left) and their correlations (right) for the Microfluidic CODES using correlation-based signal processing scheme. Auto-correlation peak can be identified when the signal correlates with the template corresponding to itself.

3.1.2   Software Design

We designed a LabVIEW program to process sensor network data (Figure 12). Our data signal was initially oversampled (50 kHz) to prevent aliasing. Then a low-pass-filtered (with a cut-off frequency of 5 kHz) was applied to eliminate the high-frequency noise. The next step was extracting the activate section form the raw data stream, so that idle time frames with no sensor activity was eliminated to increase the efficiency of the decoding process. To identify activate sections, the zero-crossing rate (ZCR) was used as the discrimination parameter, as ZCR for noise is expected to be greater than that of sensor signals. Specifically, for this experiment, we calculated ZCR every 200 samples (about 20% of the estimated particle transit time based on the flow rate), and we treated time frames with ZCR < 0.2 as activate section (containing sensor signals).

Recorded electrical signals corresponding to four individual sensors are shown with associated ideal digital codes in Figure 9. Recorded signals closely match with the ideal square pulses, while small deviations do exist. Such deviations result from a combination of several factors including the non-uniform electric field between coplanar electrodes, coupling between different electrode pairs, spherical shape of cells, as well as the constant flow speed of cells in microfluidic channels. We created a template library based on the recoded sensor signals (details in the next paragraph). By correlating the recorded signals with all of the templates in the library, we determined a template that produced the maximum correlation peak (Figure 9, right), which is also the auto-correlation peak. As the digital codes for microfluidic channels are designed to be orthogonal to each other, a dominant auto-correlation peak could robustly be identified in this process. Using this approach, we could computationally determine the microfluidic channel the cell passed

through, the duration of the sensor signal, and therefore the flow speed of the cell. 31-bit sensor signals are shown in Figure 10, and corresponding correlation results are shown in Figure 11. Compared with 7-bit correlation results, 31-bit codes provide higher processing gain.
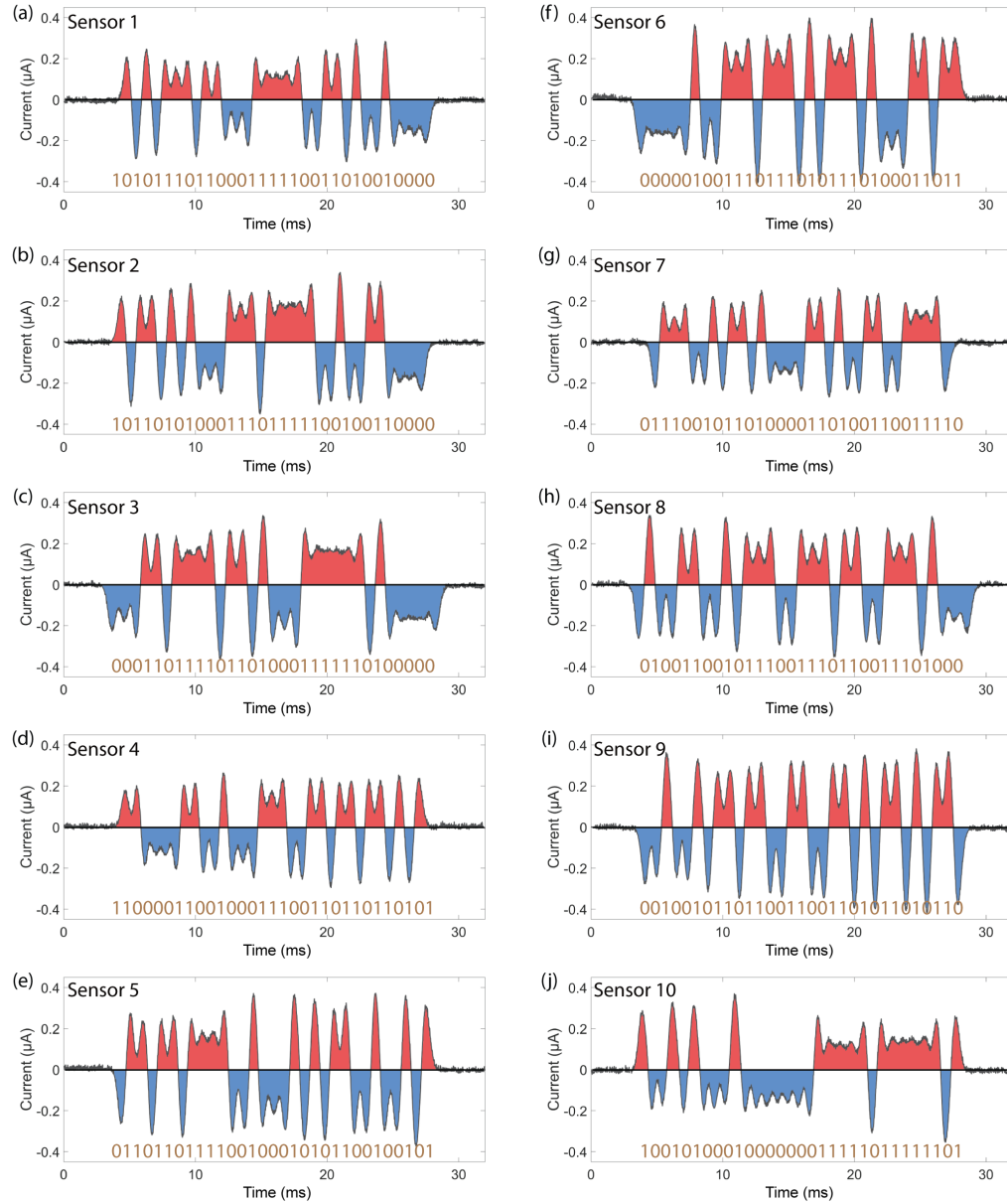
Figure 10 - Measured 31-bit electrical signals and corresponding Gold code sequences.
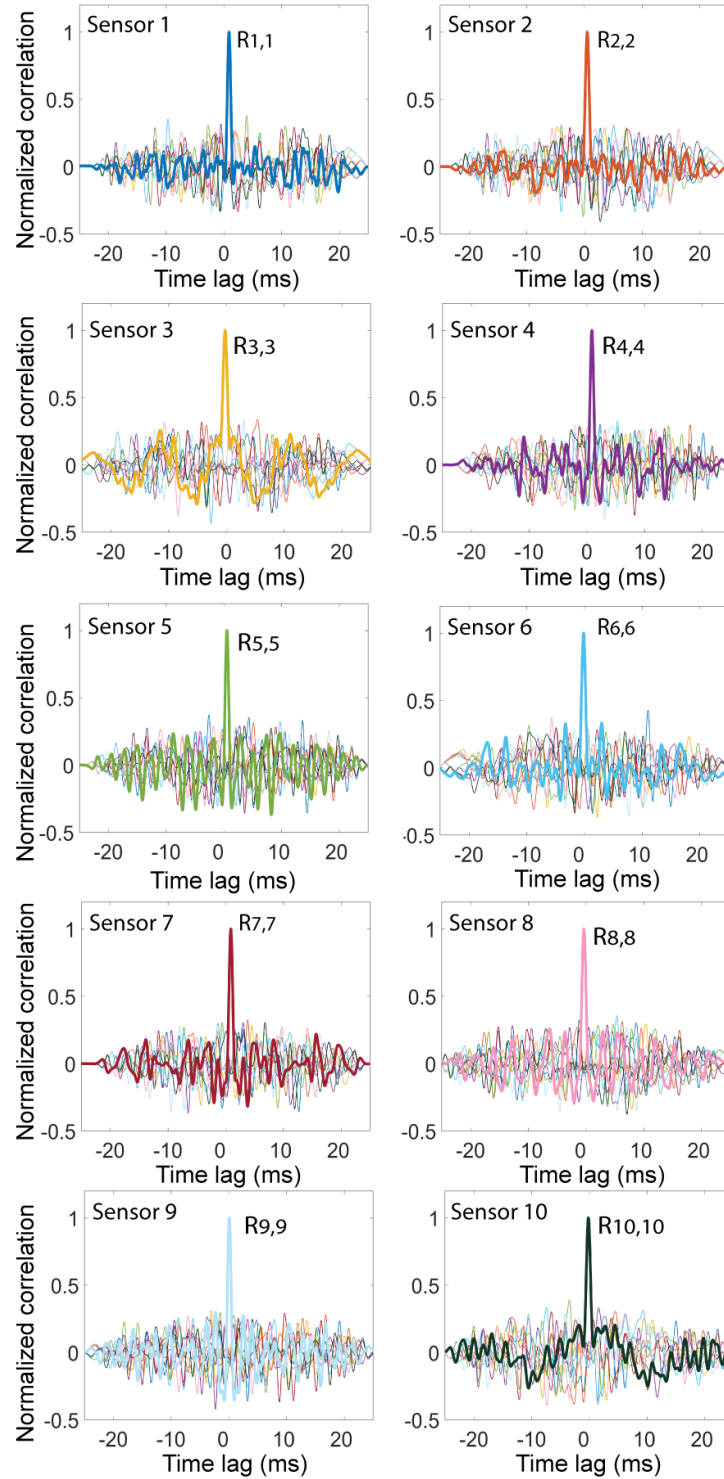
Figure 11 - Correlation of 31-bit electrical signals. Auto-correlation peak can be identified when the signal correlates with the template corresponding to itself.
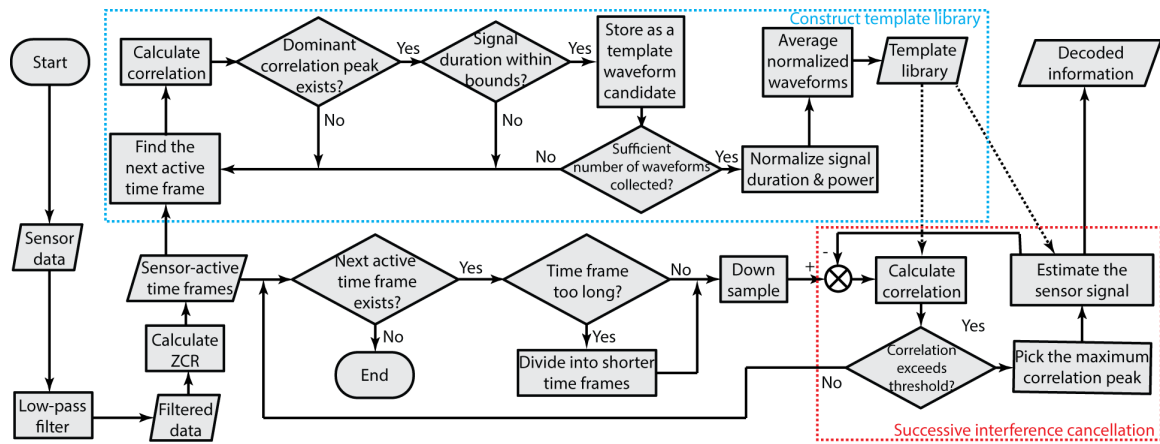
Figure 12 - Signal processing workflow of the correlation-based signal processing algorithm. A LabView program is implemented to process sensor signals. Sensor waveforms are first identified and extracted from raw sensor data. SIC is then used to decode each sensor waveform.

Each template in the template library used for correlation calculation is an average of multiple non-interfering sensor waveforms from one of the sensors. We designed a program to automatically search non-interfering sensor waveforms from the raw data stream. A waveform is treated as a template waveform if it meets two conditions: (1) the correlation produces a dominant correlation peak with one of the codes in the codeset. Here the "dominant" means the amplitude of the largest correlation peak is at least twice of that of the secondary correlation peak.; (2) the duration of the waveform agrees with the one calculated based on the expected particle flow speed. Here the "agrees" means the signal duration is within 150% of the estimated signal duration. These two conditions simultaneously ensure that the sensor waveform is a non-interfering waveform. Selected non-interfering sensor waveforms (n>20) were then grouped for individual sensors, normalized in terms for duration and power, and then averaged. Using the experimental data to construct the template library allows us to accommodate variations in the sensor signals due to artifacts in device fabrication.

43

Given an identified sensor waveform, we correlated it with all of the templates in the template library. By finding the specific template that yields the maximum correlation peak, we first determined the sensor identity of the sensor waveform. Then from the duration of the template that yielded the maximum correlation peak, we could further determine the duration of the sensor waveform, which corresponds to cell residence time on the sensing region, thus the cell flow speed. Third, from the value of the maximum correlation peak, we estimated the power of the sensor waveform, which corresponded to the size of the cell.

The correlation-based signal processing scheme can resolve situations when multiple cells simultaneously interact with coding electrodes. When such overlaps occur, multiple sensor waveforms will overlay and interfere in the time domain, causing the final sensor waveform deformed and deviate from the original shape determined by the underlying spreading sequence. In this case, the resultant waveform cannot readily be associated with any single template corresponding to a specific sensor. Accurately decoding such overlapping signals is particularly important for reliable processing high-density, where interferences are more likely to occur.
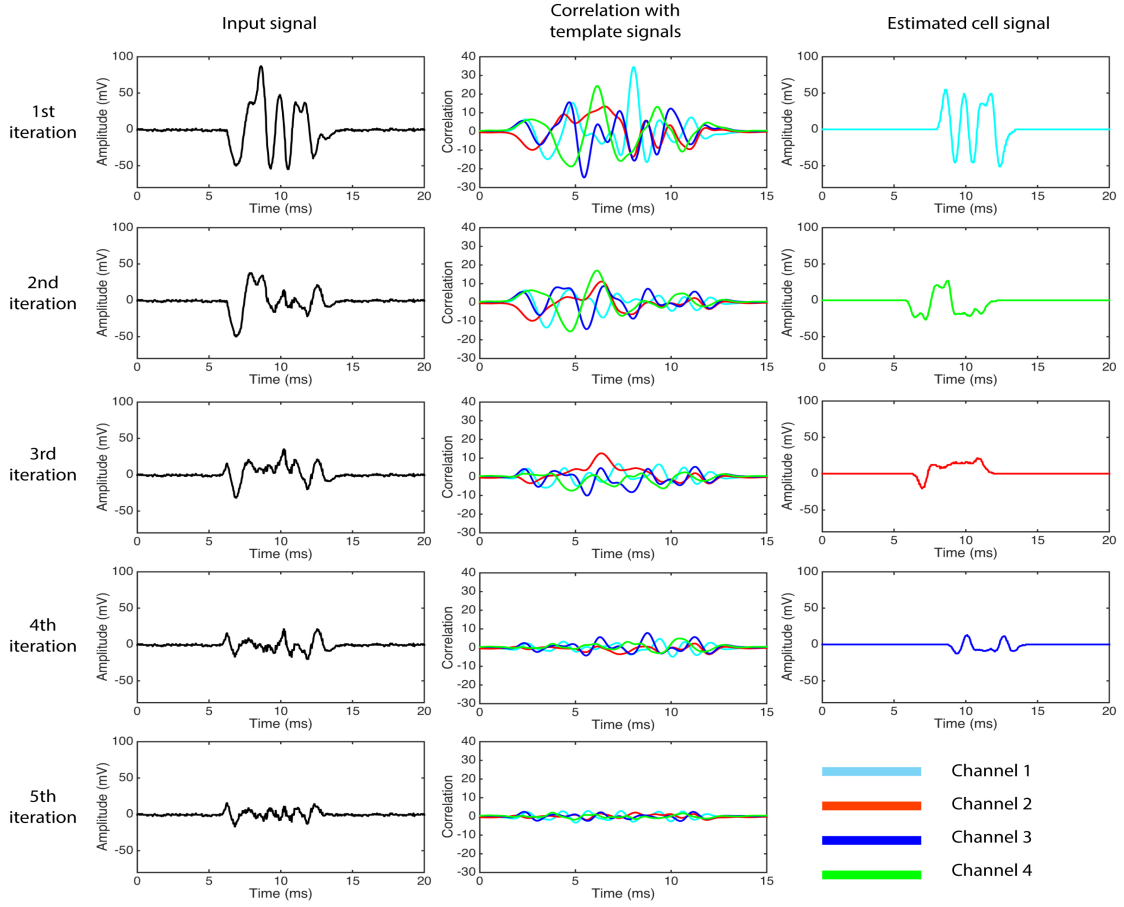
Figure 13 - Signal processing of the correlation-based algorithm based on successive interference cancellation (SIC). Given an interfering sensor waveform, signal components are successive identified and subtracted from the input.

To resolve interfering sensor signals, we developed an iterative approach based on a successive interference cancellation (SIC) scheme used for multi-user detection in CDMA. First, we determined the dominant autocorrelation peak corresponding to the strongest interfering signal by correlating the recorded waveform with the template library (Figure 13, 1st row, 2nd plot). Using the amplitude and time of the autocorrelation peak as well as the template used, we estimated the signal due to this specific cell (Figure 13, 1st row, 3rd plot). This estimated signal was then subtracted from the original signal, effectively removing the interference due to the largest cell (Figure 13, 2nd row, 1st plot). This process

45

iterated until the correlation of the template library with the residual signal did not produce

a clear autocorrelation peak for any channel (Figure 13, 5th row, 2nd plot).
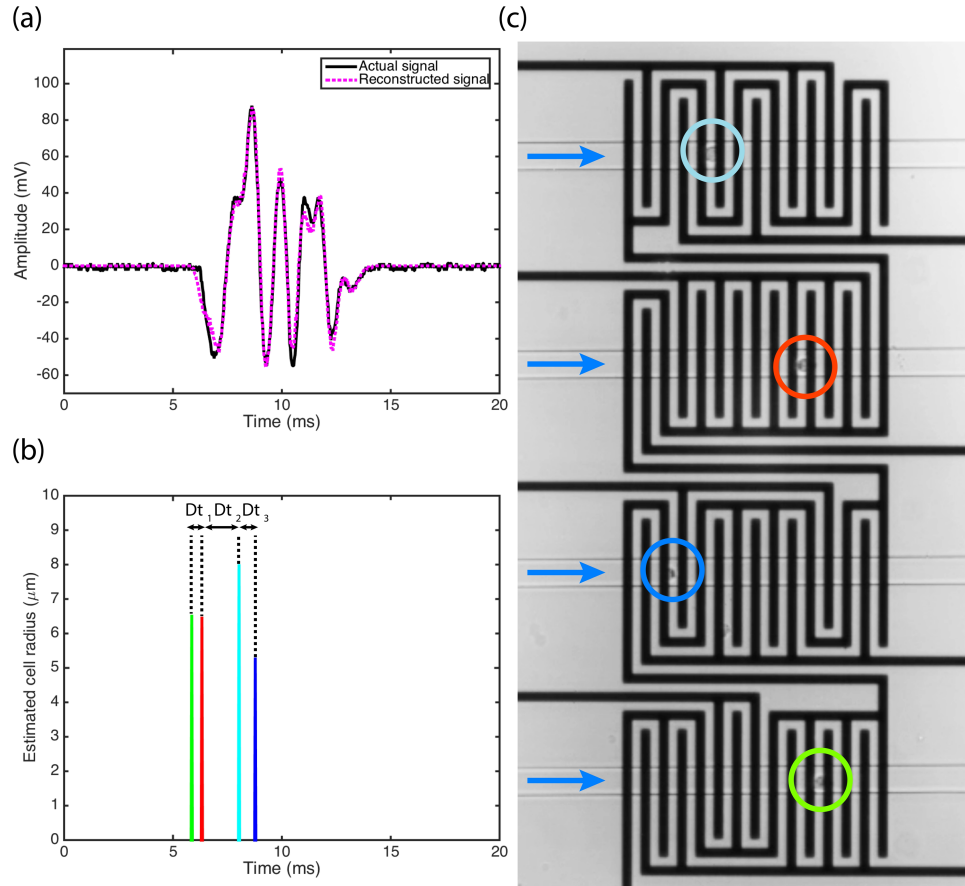
Figure 14 - Validation of the coincident signal decoding by the correlation-based algorithm. Decoding result is validated by video. (a) Reconstructed signal with original signal. (b) Estimation for the amplitude, duration, and relative timing of each estimated sensor signal. (c) Video record used for validation of the decoding result.

Following the termination of the interference cancellation process, we

reconstructed an estimation of the waveform by combining all the estimated signals from

each iteration (Figure 14a). Using an optimization process based on a least squares

approximation to minimize the mean square error between the original waveform and the

reconstructed signal, we updated our estimates for the amplitude, duration, and relative

timing of individual sensor code signals (Figure 14b). We also estimated the size of the

cells detected based on the amplitude of the estimated individual sensor signals. To achieve this, we calibrated the electrical signal amplitudes with optically measured cell sizes using linear regression (Figure 15). Figure 14c shows the simultaneously recorded high-speed microscopy image used for validating the decoding result.
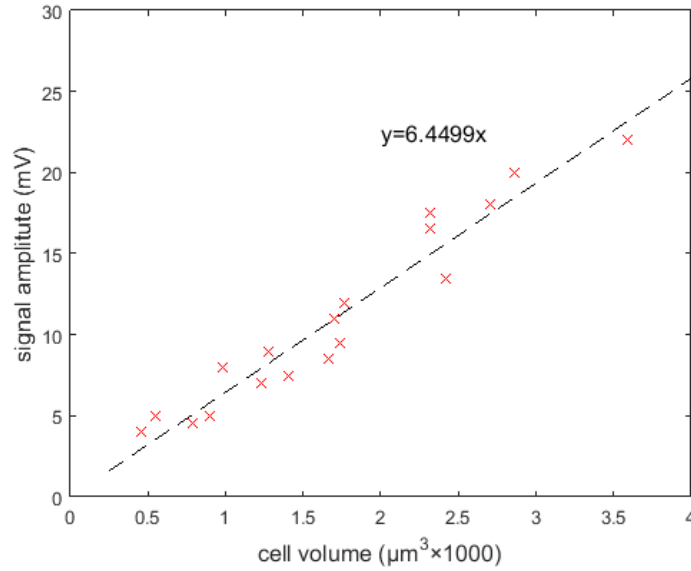
Figure 15 - Calibration between signal amplitude and cell volume. Based on the Coulter principle, there is a linear relation between cell volume and signal amplitude. MATLAB is used for fitting the parameters.

The introduced SIC approach is essential in processing samples containing particles with varying sizes such as biological cells and other particles. Successively canceling interference from signals with higher power to lower power ensures the detection and estimation of small signals, which are otherwise buried in strong interfering signals from larger cells. Furthermore, we have demonstrated that SIC is capable of solving coincident cells from different sensors, it should be noted that coincident cells from the same sensor can also be resolved, as coincident cells from the same sensor simply corresponds to

47

interference of the same digital code with its time-shifted form. With SIC, correlation can still extract the components one by one.

A comparison of our results from the Correlation-based algorithm with the information obtained from the simultaneously recorded high speed microscope images shows that the cell size and speed can be accurately measured, which validates our results (Table 1).

Table 1 - Comparison of electrically and optically measured parameters for a signal acquired by the Microfluidic CODES using correlation-based signal processing scheme in Figure 13.

Measurement type	r_{ch1} (µm)	r_{ch2} (µm)	r_{ch3} (µm)	r_{ch4} (µm)	Δt_1 (ms)	Δt_2 (ms)	Δt_3 (ms)
Electrical	8.01	6.49	5.30	6.55	0.465	1.705	0.744
Optical	8.32	6.77	5.68	7.04	0.375	1.625	0.750

The timing of the cells entering through each sensor can also be determined using SIC. When performing correlation with a shifting window, the time point at which we get the autocorrelation peak corresponds to the starting point of the corresponding sensor waveform. Therefore, during the decoding process, we could also estimate the time delay between each detected cell. A comparison of our estimates using Microfluidic CODES with the information obtained from the simultaneously recorded high-speed video with a known frame rate shows that the time delay differences between the coincident cells in Figure 14 can accurately be determined (Table 1).

48
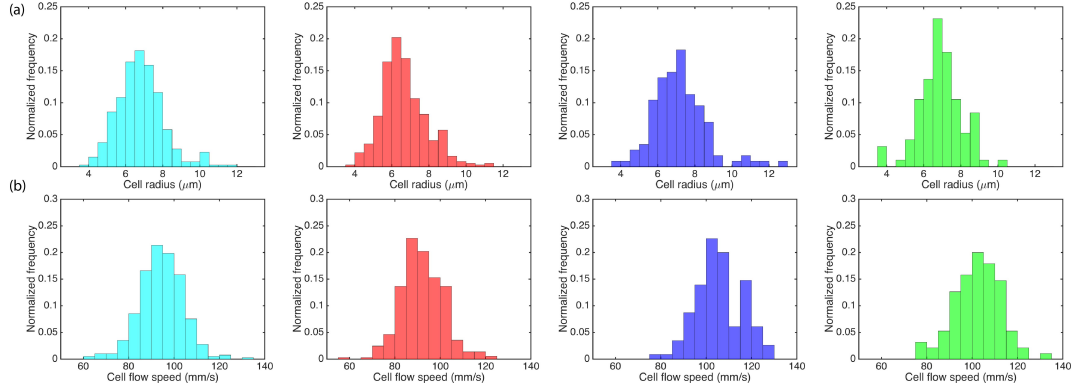
Figure 16 - Measured cell radius and speed for each sensor through the Microfluidic CODES using correlation-based signal processing scheme.

To demonstrate the reproducibility of our results and also the performance of the correlation-based algorithm for a high throughput sample processing, we analyzed electrical signals corresponding to >1,000 cells. The signals were automatically decoded in MATLAB by running the algorithm explained above and the accuracy of our results was evaluated by directly comparing our results with optical data from simultaneously recorded high-speed video. Our analysis indicates that electrical signals from 96.15% of cells (973/1,012) are accurately decoded. Success rate for decoding non-overlapping and overlapping cell signals is 98.71% (688/697) and 90.48% (285/315), respectively. Using calibration parameters (Figure 15), we also measured the size and flow speed of cells in our analysis (Figure 16). Our cell size measurement results match with the optically measured cell size distribution (Figure 17).

49

(a)

(b)
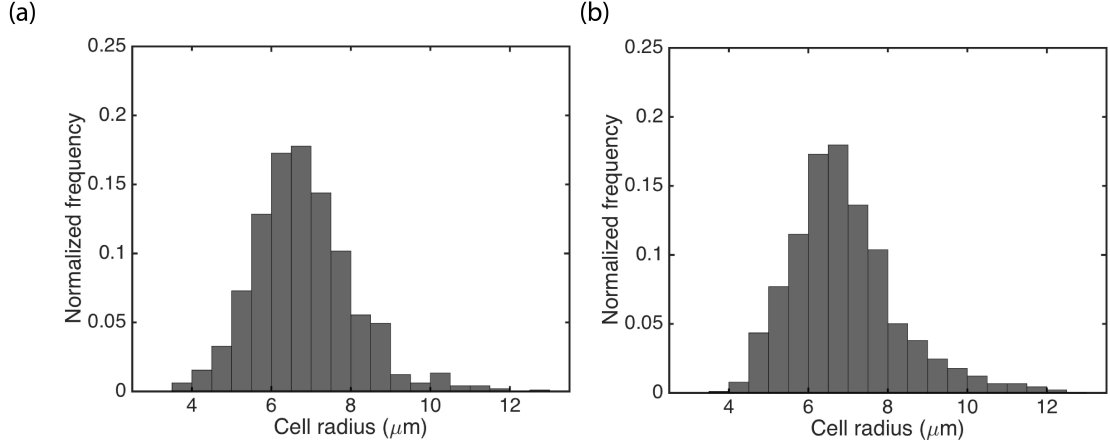
Figure 17 - Comparison of electrically (a) and optically (b) measured cell size distribution of HeyA8 human ovarian cancer cell line r through the correlation-based algorithm. They match with each other.

We have shown that with the correlation-based scheme, Microfluidic CODES is easily scalable with longer digital codes. Longer orthogonal codes with more bits provide higher processing gain in decoding and can be distinguished from each other when there is interference. On the other hand, longer Gold codes in the device also means larger sensing volume, which increases the expected number of interfering sensors. Likewise, increasing the number of sensors for a given sample density will lead to more particles overlapping due to an increase in the overall sensing volume. As such, the density of the particles in the sample is a critical parameter that needs to be considered in using the Microfluidic CODES technology. The maximum particle density that can be resolved (in analogy with the channel capacity of a CDMA telecommunications network) depends on several factors such as the individual sensor signals and their relation, the decoding scheme, layout of the microfluidic device, and the electronic noise level. Depending on the application, the sample can be diluted to reach a particle density that produces an acceptable error rate.

From signal processing perspective, decoding of time waveforms using the correlation-based algorithm is not computationally intensive using current systems as evidenced by the fact that cell phone communications on a CDMA network can be demultiplexed in real time. Furthermore, the physical events to be decoded in microfluidic devices happen much slower than bit transmission rate in cell phone communications allowing us to use more advanced and time-consuming algorithms such as SIC and an optimization processes, which we use to iteratively resolve overlapping signals from sensors.

Taken together, with the correlation-based processing scheme, Microfluidic CODES is a versatile, scalable electronic sensing technology that can be readily integrated into various microfluidic devices to realize quantitative assays by tracking particles as they are processed on the chip. The technology is very easy to implement, because (1) it is very simple from a hardware perspective (2) it is directly compatible with the soft lithography (3) it provides a direct electronic read-out without any active on-chip component, and (4) it relies on simple computational algorithms for signal processing and data interpretation.

3.2   Error-correction-based Processing of Microfluidic CODES Signals

The second signal processing scheme for the Microfluidic CODES utilizes an error-correction-based signal processing algorithm to decode sensor signals. An important feature of the error-correction-based signal processing is that the Microfluidic CODES sensor network introduced in this work uses unipolar non-orthogonal digital codes to increase the multiplexing capacity [115][116]. Employing orthogonal codes (Gold codes) to encode Coulter sensors at different locations introduces challenges in scaling the sensor network.

Specifically, larger sensor networks require encoding different sensors with longer orthogonal waveforms, leading to (1) more complex electrode layout [192] and (2) more sensor interference due to coincident cells [193][194]. Alternatively, more information can be packed into a waveform for a given signal duration (i.e., bandwidth) if non-orthogonal waveforms are used. However, the disadvantage of using non-orthogonal waveforms compared to orthogonal ones is the additional ambiguity in the decoding process. Specifically, the interference between sensors in the network from coincident cells causes output signals to be underdetermined for decoding due to the non-optimized crosstalk between non-orthogonal sensor waveforms.

To alleviate the ambiguity in the decoding of interfering non-orthogonal waveforms from sensors, we integrate redundancy in our sensor design for error correction/mitigation, which is a technique commonly used in data compression/transmission [195]. Specifically, in our design, each sensor in the network shares an extra detector with a dedicated output in addition to the code-generating electrodes micromachined to produce distinct electrical waveforms linked to specific locations on the microfluidic chip (Figure 18a). This extra detector is a conventional Coulter sensor and generates a single-bit pulse signal (error-correction signal) that contains information on count, size, and speed of cells detected in a given time-window (Figure 18b). In the decoding process, this extra information is then used to prevent the misinterpretation of the code-multiplexed signal by eliminating erroneous outcomes that conflict with the error-correction signal (Figure 18c). Because of its smaller footprint, the error-correction sensor is less prone to sensor interference from coincident cells and effectively sets the multiplexing capacity of the code-multiplexed sensor network. Importantly, our approach decouples sensor network multiplexing

capacity from the code complexity and allows the use of smaller sensors with less chance of coincidence while ensuring reliable recovery of information in the presence of interference.
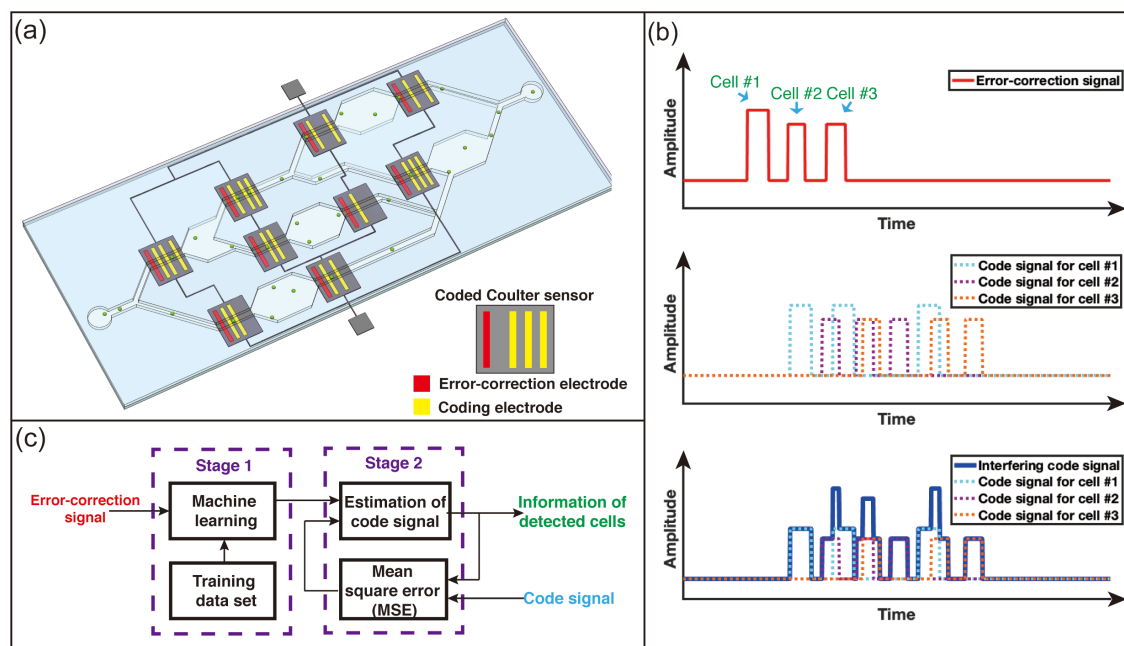
Figure 18 - Concept illustration of the Microfluidic CODES using error-correction-based signal processing scheme. (a) Concept device. Each sensor has an error-correction electrode and a coding electrode. (b) Concept sensor signal. (c) Block diagram showing the signal processing.

3.2.1   Hardware Design

For experimental testing of our sensors, we designed and fabricated an analytical microfluidic device integrated with a network of 10 code-multiplexed Coulter sensors (Figure 19a). In our sensor network, three coplanar electrodes, a common electrode, two sensing electrodes (an error-correction electrode and a coding electrode) were micropatterned to form an error-correction section and a coding section for each sensor. In

the designed layout, the common electrode was used to drive the entire sensor network with a voltage source, and the error-correction and the coding electrodes were used to measure the cell-induced impedance changes in the network by measuring changes in the electrical current flow.
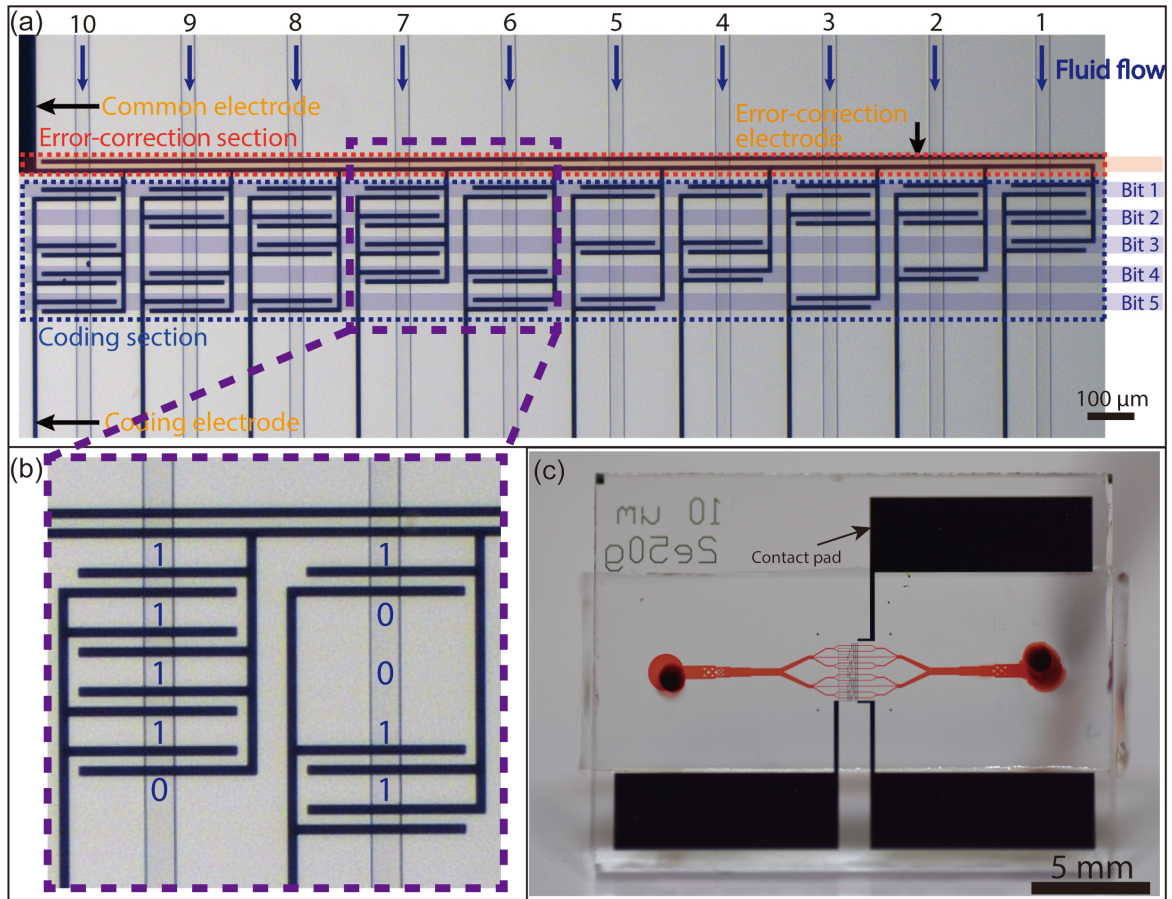
Figure 19 - Design of the Microfluidic CODES using error-correction-based signal processing scheme. (a) A 10-channel device. (b) Close-up of the electrode design on two channels. (c) Device image.

While the minimum binary code length needed to distinguish 10 sensors is 4 bits, as $2^3 < 10 < 2^4$, we chose to encode each sensor in the network with 5-bit binary codes. This is because longer codes carried more information and could be identified with less ambiguity in the decoding process. On the other hand, sensor codes cannot be extended

excessively as decoding longer codes will lead to higher device complexity, more sensor interference, and additional computation time.

To implement these codes in the device, common and coding electrode traces are routed along opposite sides of a microfluidic channel and wherever a positive bit ("1") is needed, two 10 μm-wide electrode fingers, one from each trace, are extended into the microfluidic channel such that there is 10 μm gap between the two electrode fingers. Likewise, the absence of an electrode finger pair is interpreted as a negative bit ("0"), effectively creating sensors with assigned unipolar digital codes (Figure 19b). Once interdigitated electrode patterns are aligned with microfluidic channels, the electrical current flow is confined to sections of the electrolyte-filled microfluidic channels that fall in between oppositely-charged electrodes. Therefore, it is only when cells occupied these electrically-active locations, that the electrical impedance is modulated, and the sensor output signal is produced.

In operation, cells flowing in microfluidic channels sequentially occupy electrically-active regions, producing a unipolar pulse sequence based on the underlying electrode pattern at that location. We specifically designed the electrode layout to generate isolated bit pulses in the code signals. First, we set the distance between adjacent electrode pairs, i.e., bits, to be larger than but close to the average cell diameter. This is because an excessively large gap would lower sensitivity and produce a less pronounced bit pulse. Second, we designed the neighboring fingers of adjacent electrode pairs to have the same polarity, i.e., both to be common or sensing electrodes. This layout ensures no electric field is present in between signal-generating electrode pairs. In addition, we designed the microfluidic channel height to be close to the average cell diameter to maximize sensitivity

and also minimize variations in the cell-to-electrode distance. Nevertheless, this constraint could be relaxed to accommodate cell populations with large variations in size either by designing a higher microfluidic channel as small cells occupying a fraction of the channel height could still be detected, or by vertically focusing cells to the floor of the microfluidic channel [196], which would guarantee high sensitivity and also minimize undesired variations the in the cell-to-electrode distance. A finished sensor platform is shown in Figure 19c.
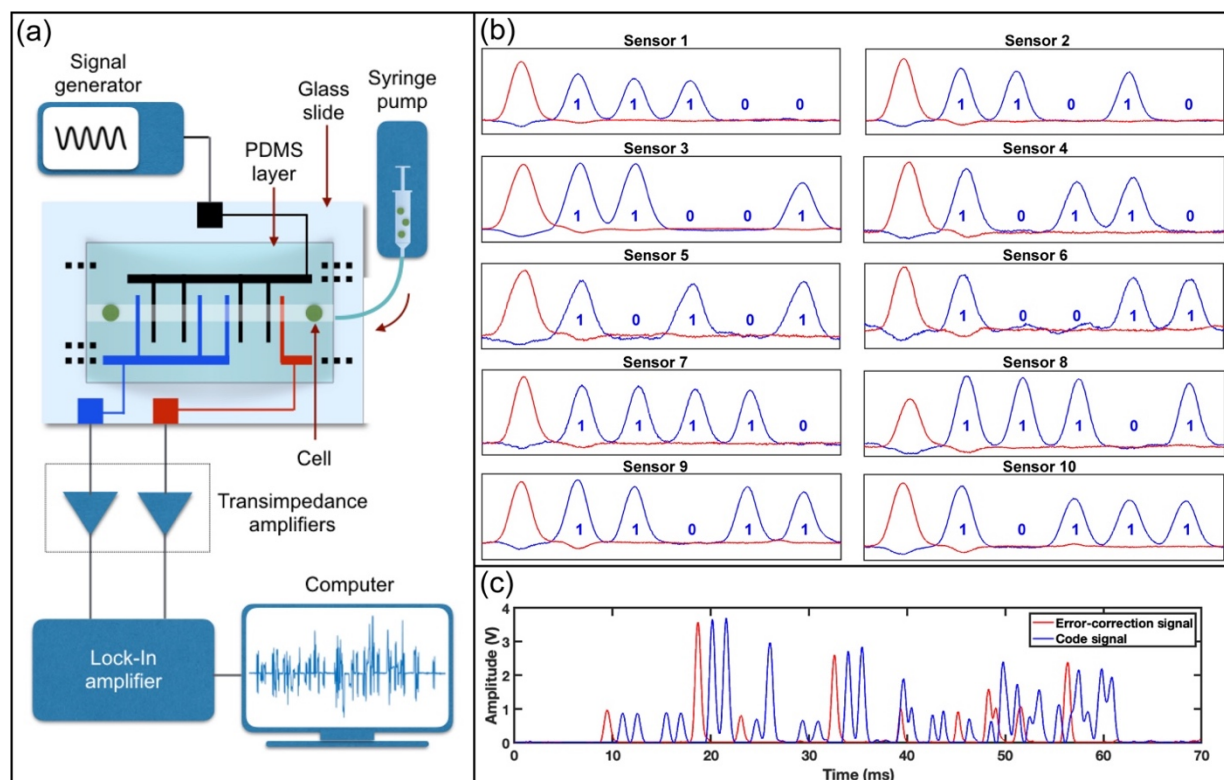
Figure 20 - Data acquisition and sample signals of the Microfluidic CODES using error-correction-based signal processing scheme. (a) Experimental setup. (b) Signals from each sensor follows the corresponding code. (c) An interfering signal.

3.2.2   Software Design

3.2.2.1   <u>Sensor Testing and Data Acquisition</u>

To acquire the sensor response to cells flowing in the microfluidic channels, we excited the sensor network with an AC signal and measure the resulting current amplitude with a lock-in amplifier (Figure 20a). The sensor network was excited from the common electrode with a 2-Vpp, 500-kHz sinusoid signal with a function generator. Electrical current signals from the error-correction and the coding electrodes were each converted into voltage signals using a transimpedance amplifier, and the signal amplitudes are measured by the two-channel lock-in amplifier. Signal amplitude information was then sampled at 50 kHz into the computer through a data acquisition board (PCIe-6361, National Instruments). It should also be noted that the sensor network could be driven at multiple frequencies simultaneously. This multi-frequency approach would then allow simultaneous measurements of cell size, speed, location along with dielectric properties (i.e., frequency response).

To characterize our sensor network, we analyzed error-correction and code signals from all sensors in the network (Figure 20b). As expected, both signals were synchronized with the code signal pulses lagging the error-correction pulses with a delay that depends on the cell flow speed. Moreover, amplitudes of individual pulses increased with the size of the detected cell as the change in the impedance is proportional to the displaced volume of the electrolyte, according to the Coulter principle. Sensor code signals corresponding to detections of single cells were isolated from each other in the recorded output waveform and could directly be recognized as they closely matched the digital codes used to encode each sensor (Figure 20b). For samples with high cell density, multiple cells coincidentally

57

detected by the sensor network lead to interferences of sensor waveforms and require

further analysis to recover sensor identities, as will be explained later (Figure 20c).
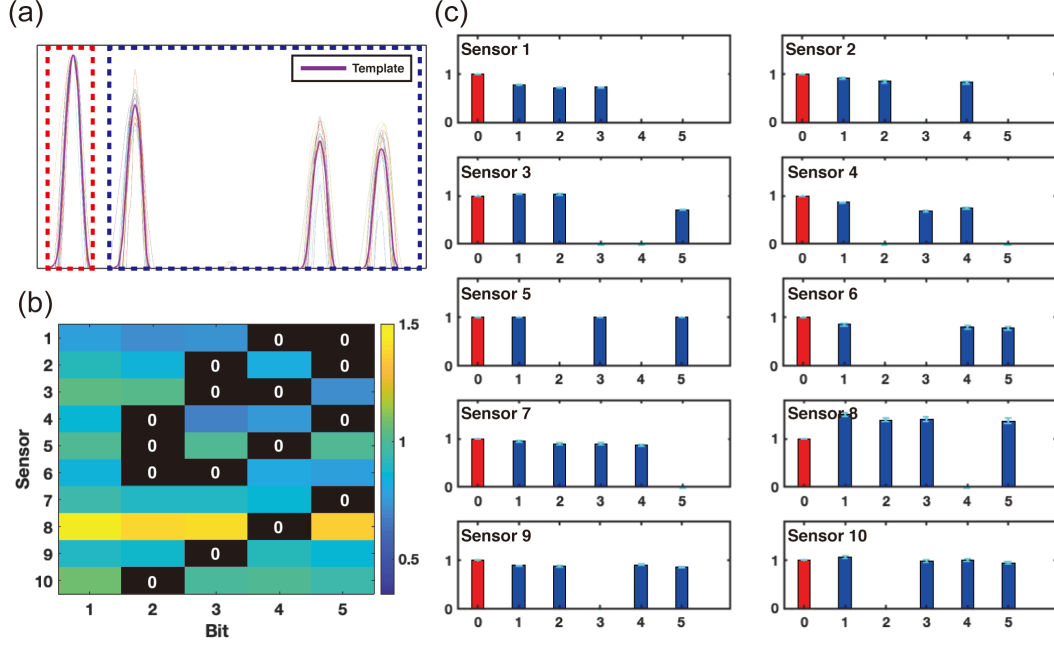
Figure 21 - Template generation of the Microfluidic CODES using error-correction-based signal processing scheme. (a) Template generation of a signal. (b) Bit amplitude variation. (c) Template for each sensor.

We also characterized the sensor code waveforms in terms of their uniformity. By

comparing sensor code signals obtained from hundreds of cells for each sensor, we find

that the amplitudes of pulses produced by the same cell varied from one bit to another

(Figure 21a). To investigate the signal variation across the sensor network, we fabricated

microfluidic devices with a serpentine microfluidic channel (Figure 22a), where a cell

sequentially interacted with all the sensors in the network and allowed direct comparisons

between waveforms from different sensors in response to the same cell (Figure 22b). By

averaging normalized amplitudes for each bit in those recorded code signals, we were able

to determine bit amplitude variation patterns across the sensor network (Figure 21b).

Furthermore, we observed these bit amplitude variation patterns to change in different devices with identical electrode patterns, a result we considered to be due to fabrication-related differences (Figure 22c). On the other hand, the relative amplitudes of bits within a code signal were observed to not change significantly for different cells detected by the same sensor. For all sensors in the network, we measured the standard deviations for the relative amplitude of individual bits in normalized signals between different events (Figure 21c) and concluded that the mean normalized amplitudes of bits for the sensor network could be used to construct a template library from recorded data to accommodate device- and sample-specific variations.

3.2.2.2 Interpretation of Error-correction Signals

We analyzed the error-correction pulses to estimate the arrival time, size, and flow speed of cells. Among these parameters, the arrival time information was readily accessible as an error-correction pulse was produced each time a cell is detected by our sensor network. The cell size was estimated from the peak amplitude of the error-correction pulse according to the Coulter principle. We calibrated the electrical data through linear regression of the cubic root of the error-correction pulse amplitude versus the cell radius measured by high-speed microscopy. Estimation of the cell flow speed was achieved by analyzing the full profile of the error-correcting pulse as described below since the pulse duration could not directly be attributed to cell flow speed and was also affected by the cell size and the electrode geometry.
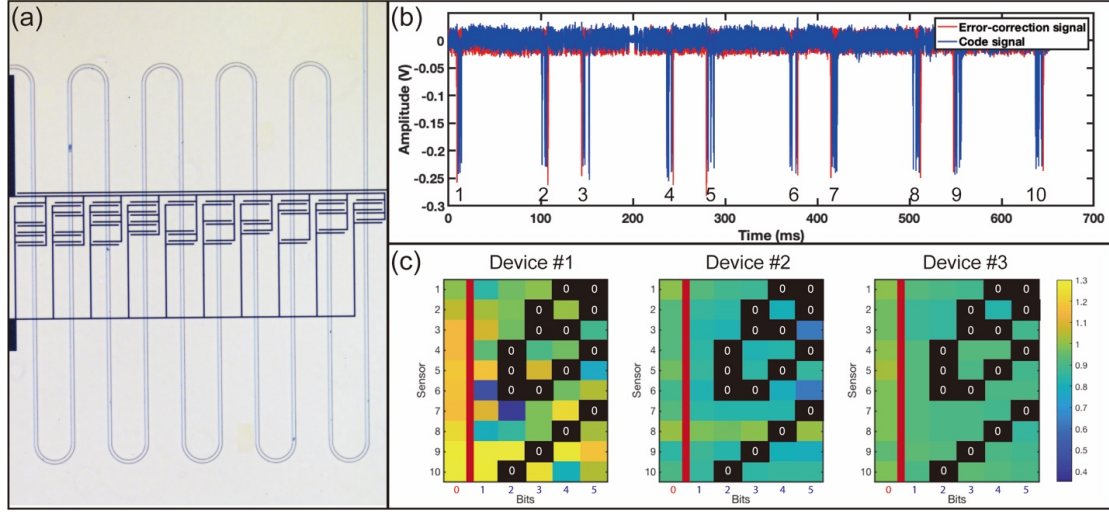
Figure 22 - Characterization of cross-sensor and cross-platform signal variation of the Microfluidic CODES using error-correction-based signal processing scheme. (a) A device with a serpentine channel. (b) 10 signals generated by one cell flowing through the serpentine channel. (c) Template bit maps of three devices.
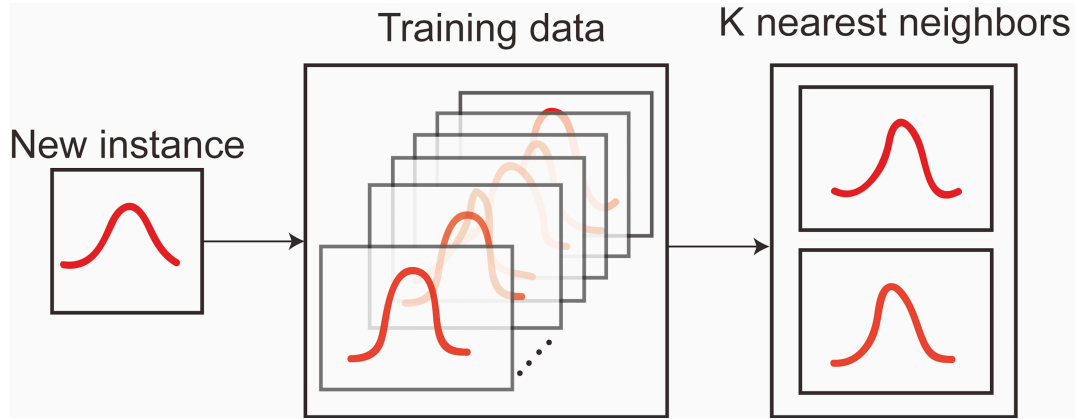
Figure 23 - Concept of the KNN algorithm.

We developed a machine learning-based model to predict the cell flow speed from the profile of the error-correction pulse. Our model employs the K-nearest neighbors (K-NN) algorithm [197], which searches the training data set for the K most similar (i.e., minimum Euclidean distance) instances and averages their values to make a prediction (Figure 23). To represent the error-correction pulse profile, we extracted four features (X_1, X_2, X_3, and X_4 representing the peak amplitude and the pulse width at ¾, ½, and ¼ of the

peak amplitude, respectively) (Figure 23b). We chose the cell travel time from the error-correction section to the coding section (Y) as the property to be estimated. Combining the predicted cell travel time with known sensor dimensions, we could calculate the cell flow speed (60 μm / Y) and estimate the duration of the code waveform (4*Y) (Figure 24).
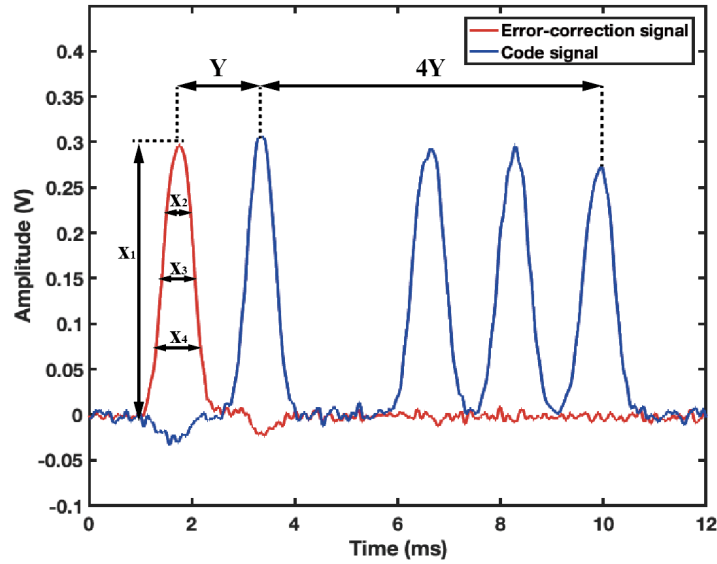
Figure 24 - Feature extraction of the error-correction signal for the KNN algorithm. Four features are extracted from the error-correction signal for a prediction of cell speed (signal duration).
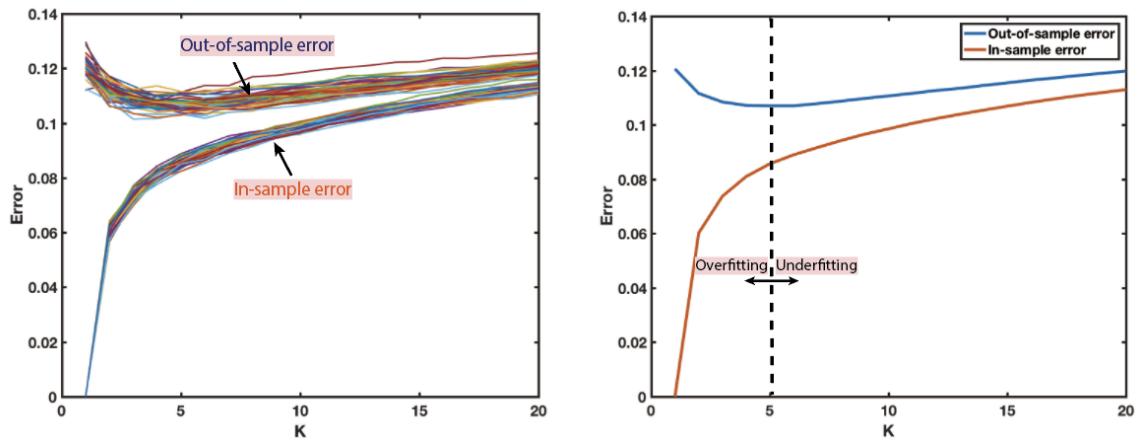
Figure 25 - Use cross validation to determine the optimal K for the KNN algorithm. The optimal K is determined to be 5.

To test the accuracy of the K-NN model, we trained our machine-learning algorithm, evaluated its error rate under varying parameters, and optimized the computational design based on characterization results. To train our model, we constructed a dataset with >1000 sensor waveforms, which was aggregated by automatically screening the raw sensor network data and identifying timeframes with sensor activity. For each cell detected, we directly extracted four features from the error-correction pulse (X_1 to X_4) and recorded the corresponding travel time (Y). To evaluate the performance of our K-NN model, we used the two-fold cross-validation. Briefly, we first randomly split the dataset into two equal halves. Then we evaluated the model by training the model on one half and testing on the same half (i.e., in-sample testing) and also by training the model on one half while testing on the other half (i.e., out-of-sample testing). In this process, each signal in the testing subset was treated as a new instance, and the cell travel time (Y) was predicted by searching and averaging the K nearest neighbors in the training subset. An overall error rate was calculated from the average deviation of the prediction from the actual value. This process was performed for K values ranging from 1 to 20 and repeated for 50 times for statistical power (Figure 25, left). We found that lower K values make the model with high-variance and more noise-prone (i.e., overfitting), while increasing the K value excessively makes the model biased and prevents it from catching subtle differences (i.e., underfitting). The optimal value of K was determined as five, which yields the minimum average out-of-sample error rate (10.5%) (Figure 25, right). When tested, the optimized algorithm is able to find five error-correction pulses that matched well in profile to the sensor data and average cell speed values associated with these pulses to predict cell flow speed (Figure 26).
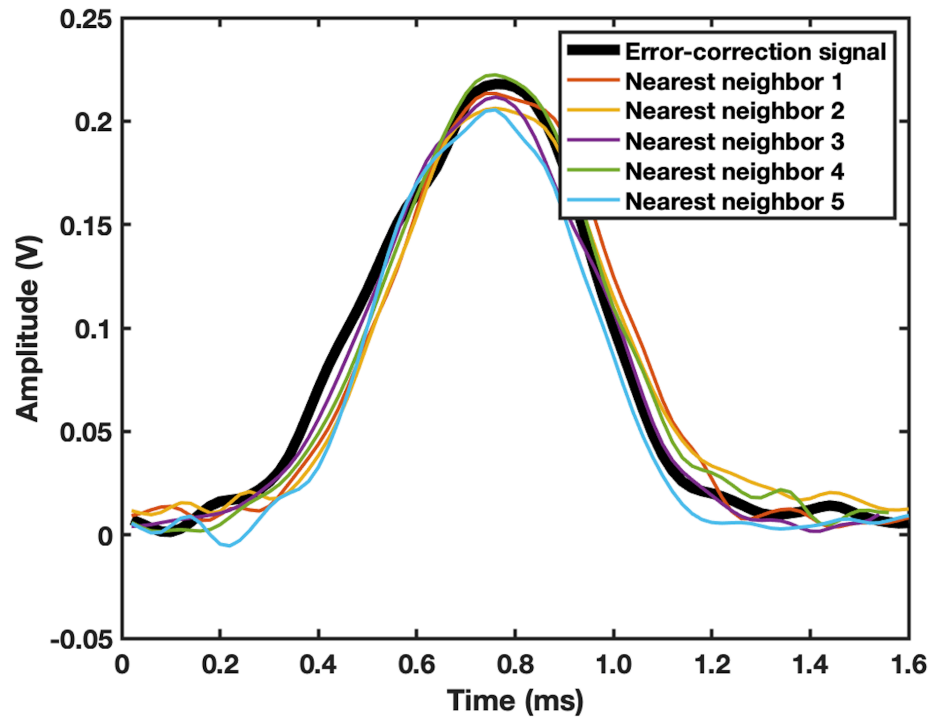
Figure 26 - An error-correction signal with its five nearest neighbors identified by the KNN algorithm. Their shapes almost align with each other.

3.2.2.3   Interpretation of Code Signals

We analyzed the coded sensor data to recover signals from individual sensors in the network based on the template libraries and information acquired from the analysis of the error-correction signal. In this decoding process, for each error-correction pulse, we first generated 10 signature waveforms accounting for all sensor codes in the network (Figure

63

27). When generating these candidate signals, (1) the peak amplitudes were determined based on the cell size estimated from the error-correction pulse and also on the previously generated template library, which provides the ratios between amplitudes of different pulses in the candidate waveform, (2) the candidate waveform duration and the delay between signals were set based on the estimated cell flow speed. Computer-generated waveforms were then compared with the actual signal, and the one yielding the minimum mean square error (MMSE) was identified as a match to determine the sensor identity. This analysis scheme is also successful in decoding interfering sensor signals due to coincident cells. To decode interfering code signals, error-correction pulses were first used to determine the number, sizes, and flow speeds of coincident cells (Figure 27a), and 10^N different signal combinations (Figure 27b) were evaluated to find the matching combination with MMSE, where N is the number of cells coincidently detected in a given time interval.
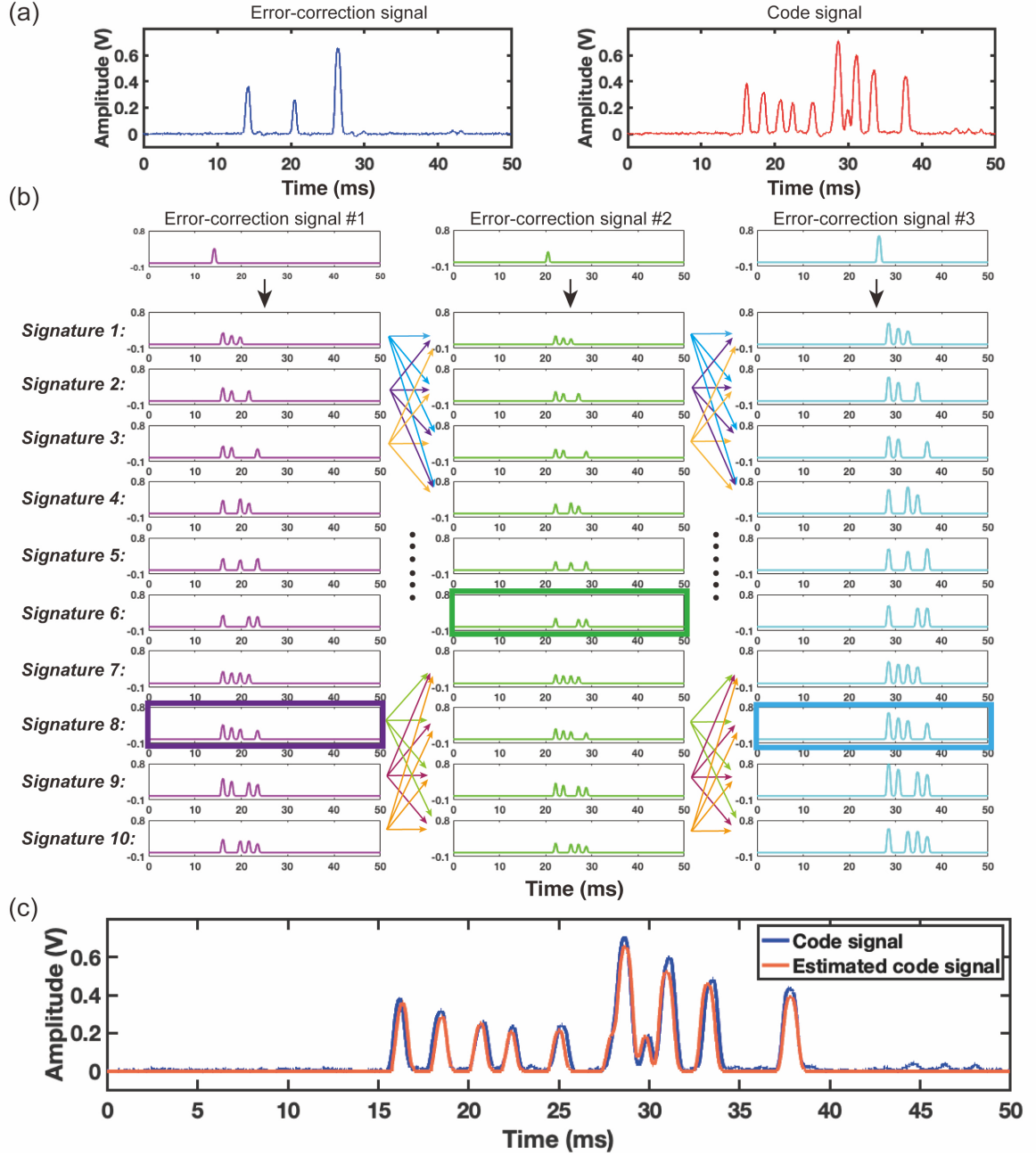
Figure 27 - Interpretation process of code signals of the Microfluidic CODES using error-correction-based signal processing scheme (a) A 3-cell interfering sensor signal. (b) Each error-correction signal generates 10 possibilities and combine with those generate by other error-correction signals. (c) The estimated code signal matches with the original code signal.

Figure 28a shows a recorded pre-coding sensor signal and the code signal from 10 cells flowed over the sensor network in a duration of 60 ms. In the decoding process, 10 pre-coding sensor pulses were first analyzed by the machine learning stage to estimate the

65

speed of each cell. Based on these estimations, each pre-coding pulse was used to generate 10 possible code signals based on the templates (i.e., pulse scaling factors) created for the 10 sensors in the network. All possible combinations of these estimated code signals for 10 pre-coding sensor pulses were analyzed and the combination yielding the MMSE fit to the recorded code signal is identified as the optimal solution. The output from our decoding algorithm and the recorded code signal closely matched (Figure 28b). Our result indicated that 10 cells flow through different microfluidic channels in the following order: 8, 7, 8, 6, 6, 7, 8, 7, 9, 7. We validated this result using the high-speed optical microscopy images.
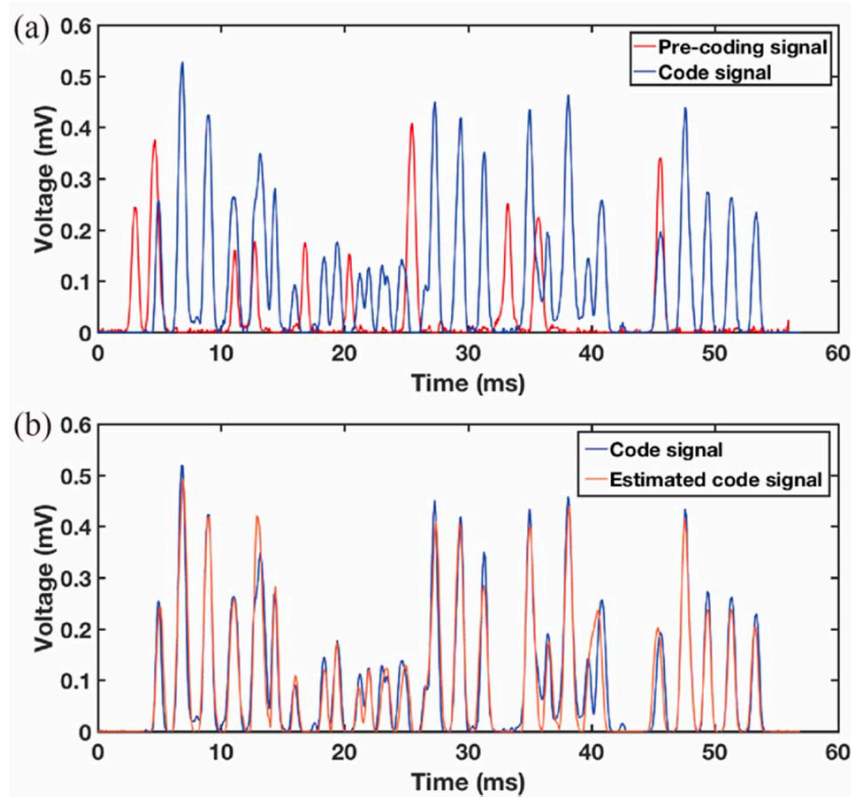
Figure 28 - Interpretation of a code signal generated by 10 cells from the Microfluidic CODES using error-correction-based signal processing scheme. (a) An interfering signal generated by 10 cells. (b) The estimated code signal matches with the original code signal, indicating the correctness.
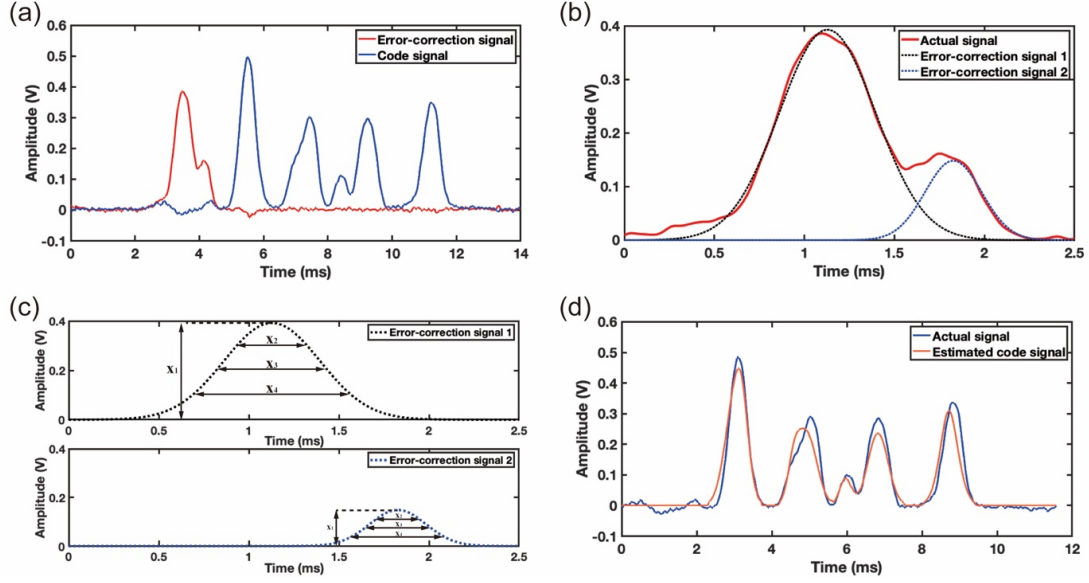
Figure 29 - Interpretation of code signals with interfering error-correction signals of the Microfluidic CODES using error-correction-based signal processing scheme. (a) A representative recorded signal from two coincident cells with the interfering error-correction pulses. (b)Estimation of individual error-correction pulses via curve fitting. (c) Feature extraction of estimated error-correction signals. (d) The recorded code signal overlaid with the estimated code signal.

Besides interfering code waveforms, we observeed cases, where error-correction pulses from different sensors also interfered (Figure 29a). In these cases, high cell density in the suspension led to multiple cells coincidentally interacting with error-correction electrodes despite their significantly smaller footprint than coding electrodes. To recover data in those instances, we first deconvolved interfering error-correction pulses. First, a peak-search algorithm was used to determine the number of contained individual pulses in the error-correction signal. Second, a curve-fitting algorithm was used to fit the interfering error-correction signal with a certain number of individual Gaussian-shaped pulses with different amplitudes and durations (Figure 29b). Gaussian-shaped pulses were specifically chosen in this fitting process because the profile of a resistive pulse followed a Gaussian profile [198]. Estimated error-correction pulses were then analyzed individually according

to the decoding process explained earlier to estimate cell size and speed (Figure 29c), and

based on these parameters, the corresponding code signal was estimated (Figure 29d).
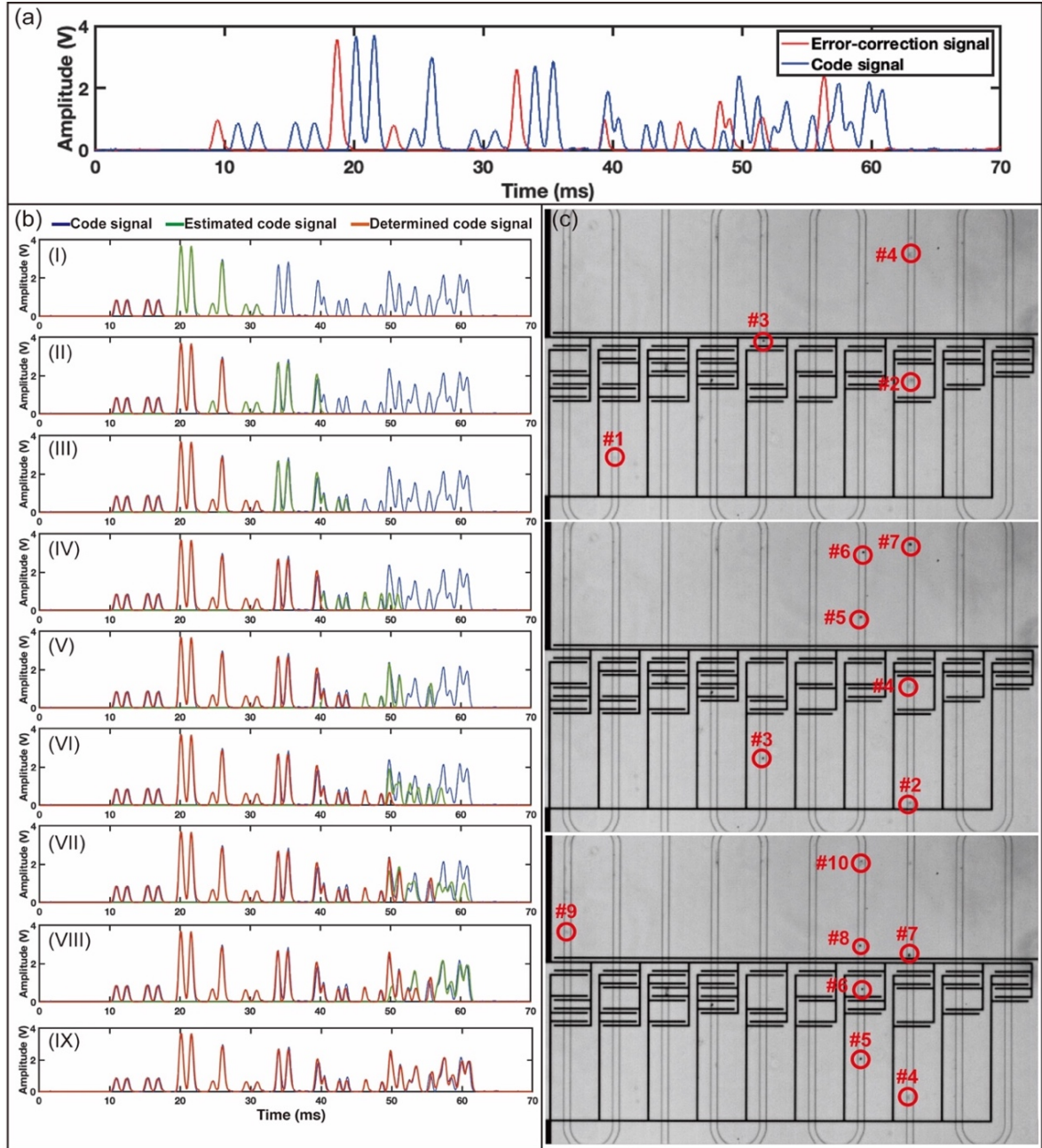
Figure 30 - Combining the MMSE fitting with a moving-window approach for signal processing of the Microfluidic CODES using error-correction-based signal processing scheme. (a) A section of a recorded output signal that contains data from 10 cells. (b) Iterative decoding of the sensor waveform through a sliding window. (c). The data from the images matched the results from the sensor network.

To evaluate the accuracy of our sensor network, we compared the results from the decoded electrical data stream to the simultaneously recorded microscope images, regarded as the ground truth, and calculated the error rate in our measurements. In order to capture fast-flowing cells, images were acquired by employing an optical microscope equipped with a high-speed camera set to record cell flow across the whole sensor network at 1000 frames per second.

To automatically analyze the electrical data from the sensor network, we implemented our decoding algorithm in MATLAB. To perform the decoding of sensor waveforms on a continuous data stream, we combined the MMSE fitting with a moving-window approach. Briefly, we processed the output signal three error-correction pulses at a time. Once the decoding of a timeframe is completed, the window was shifted by one error-correction pulse, and the process was iterated until the whole data stream is decoded. The computational complexity of this process scales as $O((N-M+1)*10^M)$, where 10 is the number of code-multiplexed sensors, N is the total number of cells detected in the time interval, and M is the number of cells analyzed at a time within the moving window, respectively.

A direct comparison of processed sensor signal blocks with corresponding microscope images shows successful tracking of cells over the sensor network (Figure 30). We investigated step-by-step decoding of a 70 ms-long time interval that contains data from 10 cells (Figure 30a) as an example to illustrate coherence between electrical and visual data. Starting with the first window containing the first three error-correction pulses and sliding one pulse at a time, we were able to find a closely-matching estimation with

69

the recorded experimental signal (Figure 30b). Both sensor identities and the sequence of cell flow obtained from the decoded data agree with the high-speed microscopy data (Figure 30c).
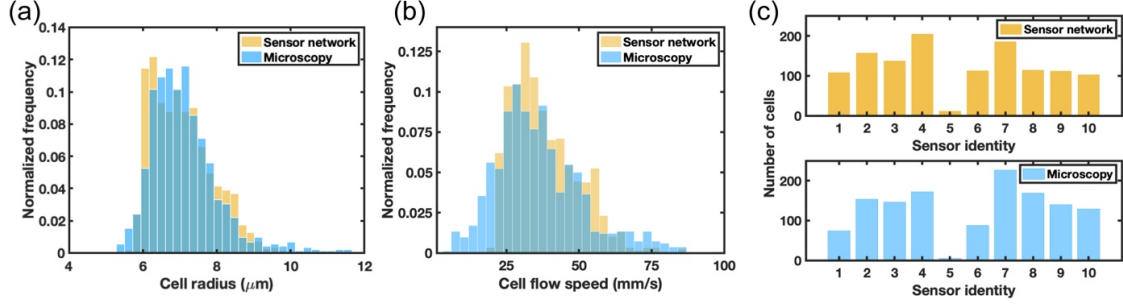
Figure 31 - Benchmarking sensor network results of the Microfluidic CODES using error-correction-based signal processing scheme against microscopy. (a) Cell size. (b) Cell flow speed. (c) Cell sensor identity.

To quantitively characterize the sensor network performance, we compared cell speed and sensor identity measurements from the electrical waveform and the associated high-speed video footage corresponding to >1200 cells. Due to the limited resolution of high-speed videos, we performed image-based cell size measurements with the ImageJ software on still, high-resolution microscope images of a surrogate cell population sampled from the same tissue culture (Figure 31). Optically-measured cell size distribution closely matches with that acquired from our sensor network (Figure 31a), with the Kullback–Leibler (KL) divergence between these two distributions calculated to be 0.044. Besides the errors introduced by the computational decoding process, the small divergence between the prediction and the ground truth comes from the fact that the cells analyzed by the sensor platform and microscope are not the same population. Optically-measured cell flow speed distribution matches well with that acquired from the sensor platform, especially for flow speeds between 20 and 70 mm/s. (Figure 31b). Higher KL divergence (0.435) is mainly due to the mismatch in the lower end of the cell flow speed. Loss of accuracy with lower

cell speed is due to the training dataset lacking cells with lower flow speeds, which could be improved by expanding the dataset to include a wider range of cell flow speeds. As for the accuracy of predicting sensor identity (i.e., spatial information), the success rate is measured as 90.07%, demonstrating cells could accurately be tracked with the on-chip sensor network (Figure 31c).

3.3 Deep Learning-based Processing of Microfluidic CODES Signals

The deep learning-based signal processing scheme of the Microfluidic CODES uses deep neural networks to recognize sensor signals. The technology doesn't rely on orthogonality among digital spreading codes, but on recognizing the specific waveform patterns (bipolar digital codes) of sensor signals. The workflow of the entire system developed in this work can be divided into three blocks (Figure 32). Specifically, deep neural networks are designed and trained to interpret the output waveform. Trained neural networks provide the size, flow speed, and sensor identity for each particle detected on the microfluidic chip.
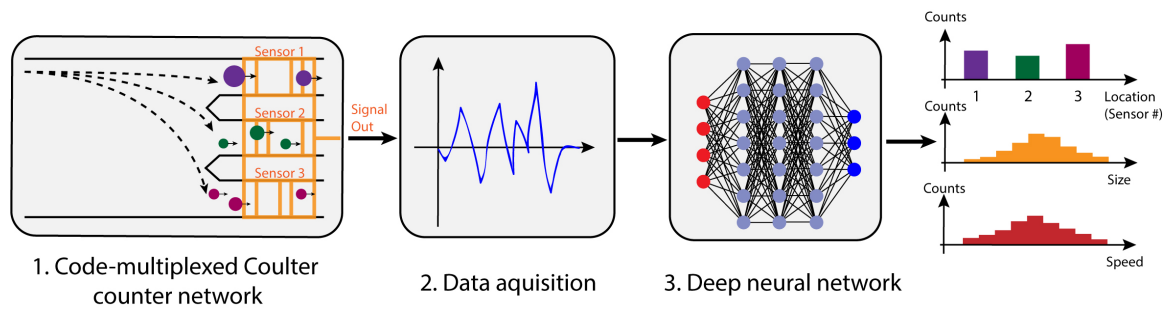
Figure 32 - Concept illustration of the deep learning-based processing of the Microfluidic CODES. Sensor signal is interpreted by a deep neural network to get the information of cell size, speed, and location.

3.3.1 Hardware Design

As a test platform, we designed a code-multiplexed Coulter sensor network with ten sensors (Figure 33). Each sensor was designed to produce a distinct but non-orthogonal waveform. To create the spreading codes, we generated ten 15-bit bipolar code sequences, where each bit was treated as a Bernoulli random variable with $p = 0.5$. The design and fabrication process of the microfluidic device was the same as the Correlation-based Microfluidic CODES, where three electrodes were patterned to encode different channels a specific spreading code. Specifically, the generated code sequences are: Sensor 1: 010101011000101; Sensor 2: 111110001001100; Sensor 3: 100010100101100; Sensor 4: 000101110011011; Sensor 5: 101111001001000; Sensor 6: 110000100110100; Sensor 7: 110100011111110; Sensor 8: 111011000011010; Sensor 9: 110011111001111; Sensor 10: 100111110101110.
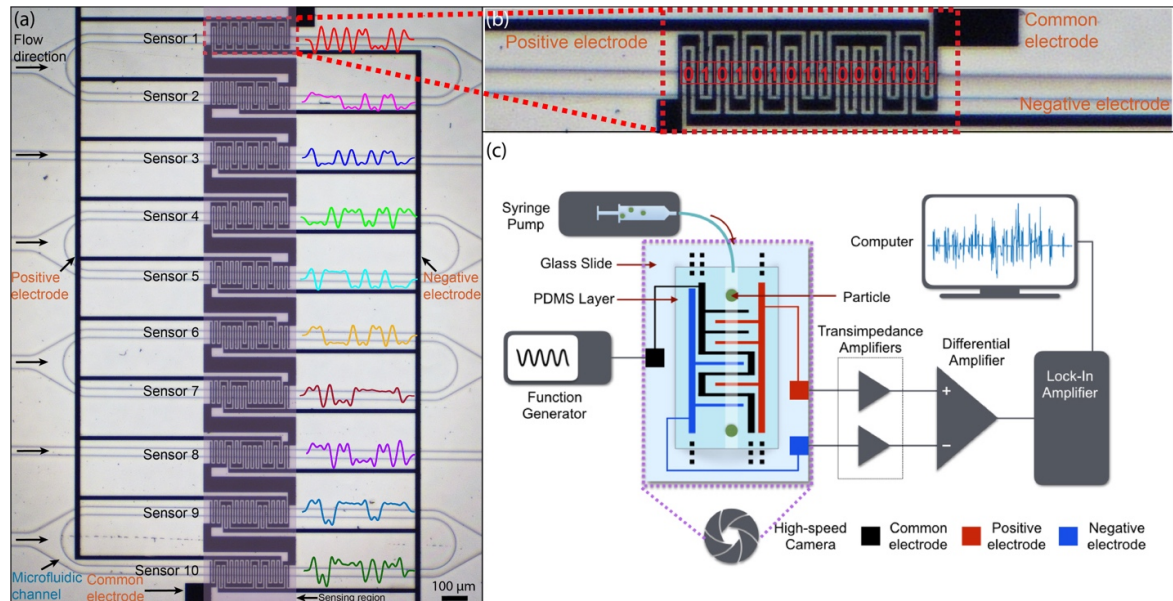
Figure 33 - Design and experimental setup of the Microfluidic CODES using deep learning-based signal processing scheme. (a) Electrode design of the device. Each sensor is encoded with a randomly-generated sequence. (b) A close-up image for the first sensor. (c) Experimental setup.

3.3.2   Data Augmentation

We first processed recorded sensor waveforms to construct the training data for ConvNets. To extract representative sensor waveforms from the raw sensor output signal, we developed a signal-identification program. With this program, sensor waveforms were discovered by computing the signal variance within a sliding window as the window traversed the entire raw sensor output signal. The sole purpose of this process is to identify and mark the regions of interest in the raw sensor output signal with potential sensor activity to be used in subsequent operations.

To automatically label each identified sensor waveform with the corresponding sensor identity, we implemented a correlation-based algorithm. By computing the cross-correlation between each extracted sensor waveform with a template library containing all code sequences, the algorithm obtained two vital pieces of information about each waveform. First, it determined if the waveform is a non-interfering sensor waveform (i.e., contains only one signature waveform), or an interference sensor waveform, which contained multiple signature waveforms interfering with each other. This differentiation was achieved by comparing the amplitude of the primary correlation peak to that of the secondary correlation peak. Second, for each non-interfering sensor waveform, the algorithm identified and labeled its corresponding sensor identity based on the code template that produced the primary correlation peak. At the same time, the power and duration of each labeled non-interfering sensor waveform were also calculated. Labeled

non-interfering sensor waveforms were first manually checked for an accuracy assertion, then normalized, and used to construct the training data.

To increase the number of waveforms available for constructing the training data, and thereby improve the performance of our ConvNets, we employed a data augmentation process on the labeled non-interfering sensor waveforms. We first randomly picked waveforms from the dataset and then scaled their power and duration in the digital domain to simulate signals for cells that have different sizes and speeds, respectively. In this process, the power and duration of a waveform were treated as random variables, whose distributions were ensured to match those of the original dataset. Additive white Gaussian noise (SNR = 30 dB, to mimic experimental noise level) was then added to each augmented waveform to introduce variation in the training data set against potential overfitting. We repeated this pick-and-vary process and create a waveform database of 1,000,000 augmented non-interfering sensor waveforms to be used for training data construction.

Besides the non-interfering sensor waveforms, we also generated a database of interfering sensor waveforms to train our algorithm for resolving data from coincident cells. We created interfering sensor waveforms in the digital domain by adding two non-interfering sensor waveforms of known amplitudes and durations with a certain time delay. We repeated this process by randomly drawing different pairs of non-interfering sensor waveforms from the waveform database and adding them with a randomly-determined time delay to create a large database that covers different coincidence scenarios. For this work, we randomly picked 150,000 signals from the waveform database to construct a database of non-interfering sensor waveforms and used the remaining 850,000 to construct a database of interfering sensor waveforms.

74

3.3.3 Software Design (V1) - based on Interference Cancellation

3.3.3.1 ConvNet Design
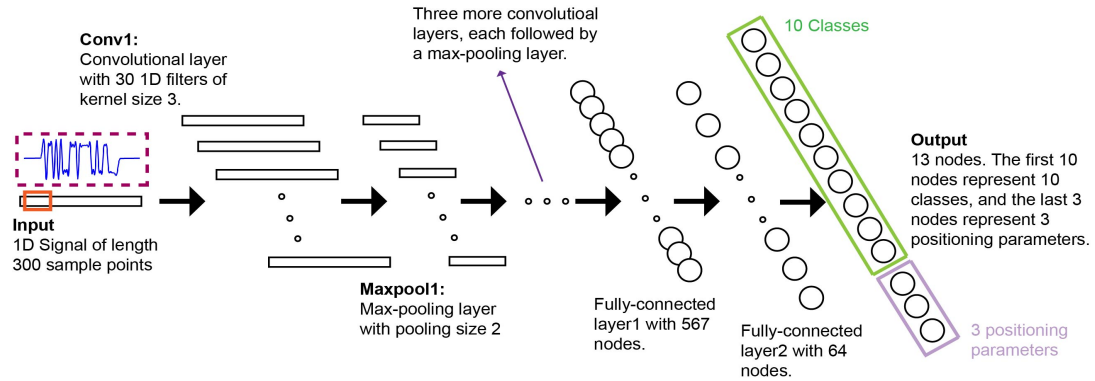
Figure 34 - Concept and ConvNet design of the Microfluidic CODES using the first version deep learning-based signal processing scheme. The deep learning model predicts the position and class of the signal component with the highest power.

In the first version deep learning-based signal processing scheme, a ConvNet is trained to predict the position and sensor identity of the signal component with the highest power in an input sensor waveform. This signal is then estimated and subtracted from the input sensor waveform. Specifically, we designed a ConvNet with 4 convolutional layers, each of which is followed by a max-pooling layer and ReLU nonlinearities (Figure 34). Following the convolutional layers are two fully-connected layers and the output layer. The output layer has 13 nodes, where the first 10 nodes represent 10 classes (sensors) and the last 3 nodes represent the positioning parameters, including start time, amplitude, and duration of the signal. Given an input signal, the ConvNet detects the sensor signal contained in it, along with the corresponding positioning parameters. The positioning parameters are then used to calculate the flow speed and the size of the particle. Specifically, when the input signal is an overlapping sensor signal (contains multiple sensor signals overlaid with each other), the ConvNet will first detect the dominant sensor signal, and an

estimation of the dominant sensor signal will be reconstructed and subtracted from the original input signal. The residue signal will be fed into the same ConvNet for further detection.
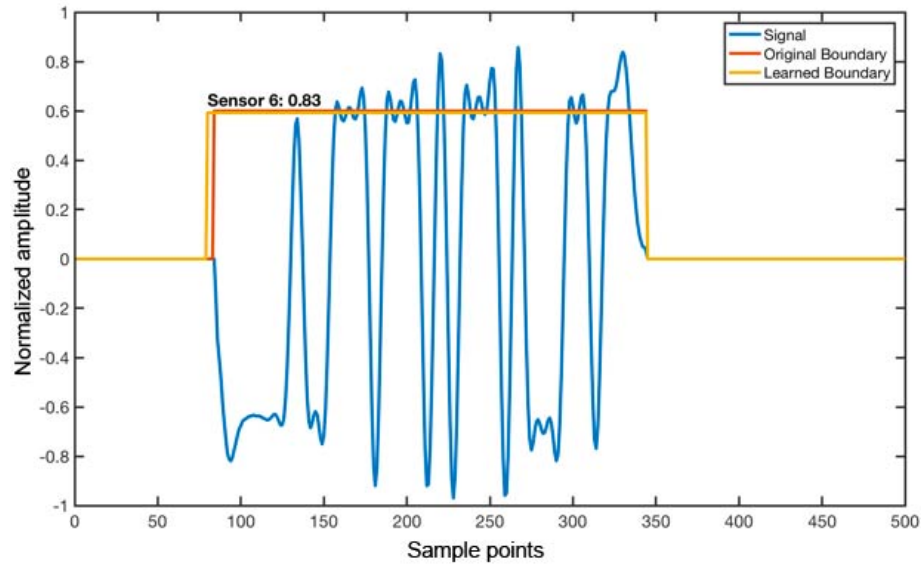
Figure 35 - Processing of non-interfering signals through the first version deep learning-based signal processing scheme

3.3.3.2   ConvNet Querying

Given a non-interfering signal, the ConvNet outputs the probability with which the input belongs to each sensor in the network. The identity of the sensor with highest probability is determined as the classification result (sensor 6 with a probability of 83% in this specific example). The ConvNet also output the bounding parameters, which are used to build a bounding box for the signal.

Given an interference signal, the strongest sensor signal is first detected and reconstructed based on the sensor identity and the bounding parameters. The reconstructed

76

signal is then subtracted from the original signal. The residue signal is then fed into the

ConvNet for further processing.
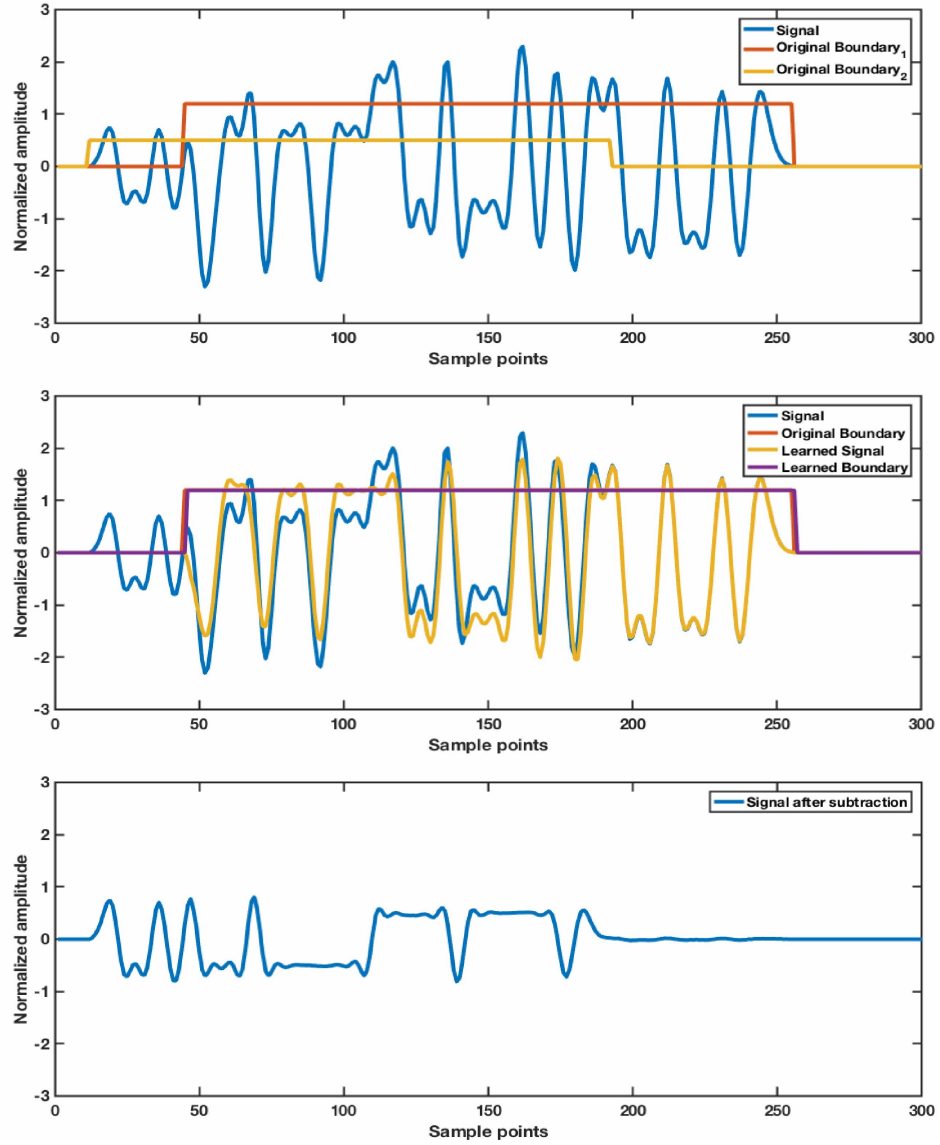
Figure 36 - Processing of interfering signals through the second version deep learning-based signal processing scheme for the Microfluidic CODES. Given an interfering sensor waveform (top), the signal component with the higher power (middle) is estimated and subtracted from the input (bottom).
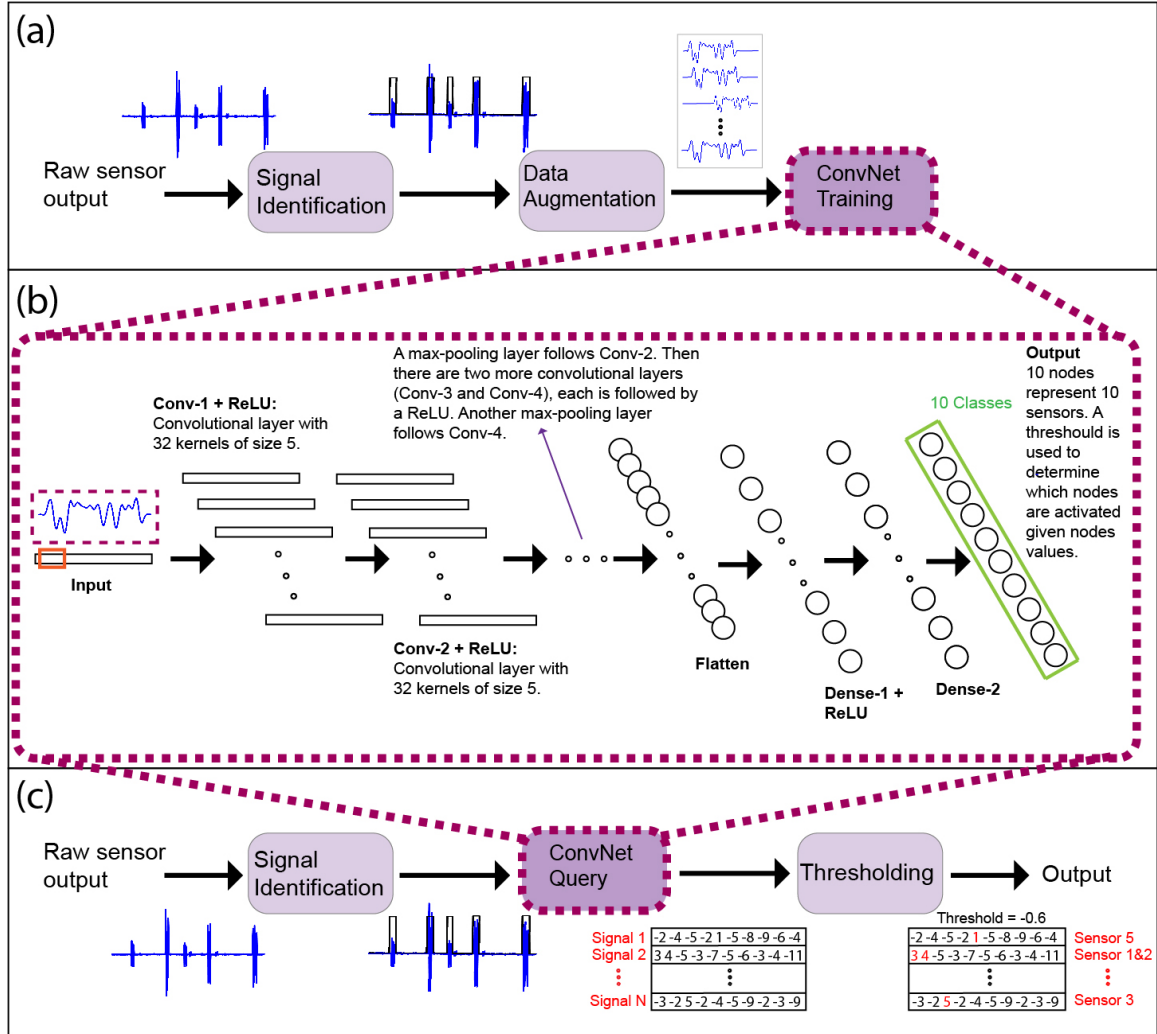
Figure 37 - Concept and ConvNet design of the second version deep learning-based processing for the Microfluidic CODES. (a) The signal processing workflow. (b) ConvNet design. (c) Given an input signal, the ConvNet predicts the probability with which the input signal belonged to each and every Coulter sensor in the microfluidic device.

3.3.4   *Software Design (V2) - based on Multiclass Classification*

3.3.4.1   ConvNet Design

In the second version deep learning model, we used the multiclass classification scheme [206] to design the deep learning model. Specifically, we built a ConvNet that

contained four convolutional layers (Figure 37b). The first convolutional layer (Conv-1) has 32 convolutional kernels of size 5, resulting in 192 trainable parameters. The output feature map is then processed by Conv-2, which also has 32 convolutional kernels of size 5, and a total of 5152 trainable parameters. A max-pooling layer is placed right after Conv-2 to down-sample the convolved signal, and the output is fed into Conv-3, which contains 64 kernels and 10304 trainable parameters, and then Conv-4, which contains 64 kernels and 20544 trainable parameters. Another max-pooling layer is placed after Conv-4. Following the second max-pooling layer are a flatten layer and two dense (fully connected) layers, in which the first dense layer has 180224 trainable parameters and the second has 640 trainable parameters. The model has a total of 217056 trainable parameters. The second dense layer feeds the final output layer, which has 10 nodes, representing 10 Coulter sensors (10 classes). Given an input signal, the ConvNet predicts the probability with which the input signal belonged to each and every Coulter sensor in the microfluidic device. A predetermined probability threshold is used to predict the identity of the activated sensor (Figure 37c).

3.3.4.2 ConvNet Training

The ConvNet is trained with a batch size of 500 (batch size: the number of training signals processed before the model is updated), and an epoch number of 30 (epoch number: the number of times the learning algorithm works through the entire training dataset). The binary cross entropy (BCE) is used as the loss function to calculate the classification error. The Adam optimizer is used to minimize the error in each iteration. The learning rate is set to 0.001 for the first 10 epochs, 0.0001 for epochs 11 through 20, and 0.00001 for epochs 21 through 30.
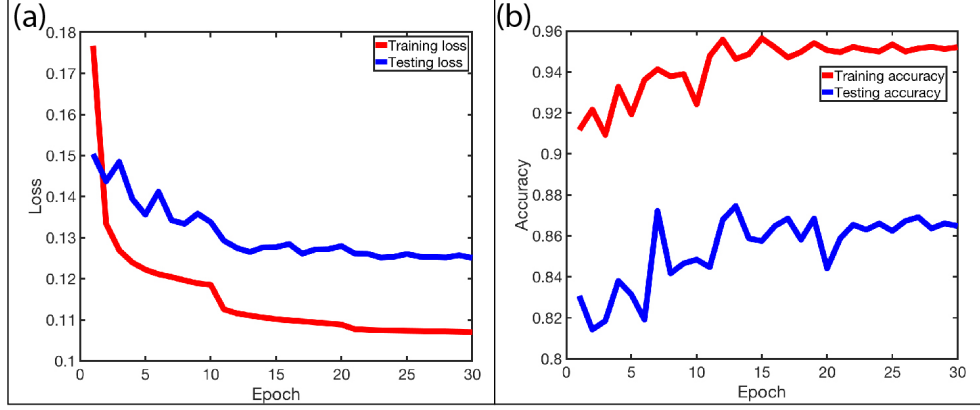
Figure 38 – Training (a) and testing (b) performance of the second version deep learning model for the Microfluidic CODES.

As the number of training epoch increases, the ConvNet improves itself to better represent the input data. After 25 epochs, the training and testing losses remain below 0.11 and 0.13, respectively, and the training and testing accuracies remain above 95% and 86%, respectively (Figure 38).

3.3.4.3   ConvNet Querying

For non-interfering sensor signals (Figure 39, the first and second rows), the ConvNet output for the corresponding sensor is close to 100%, while outputs for other sensors are nearly 0%. In this case, we could easily identify the activated sensor. For interfering sensor signals due to coincident particles (Figure 39, the third row), the corresponding output probabilities are reduced but the activated sensor identity could be correctly determined by using a predetermined threshold value (33% for this work).
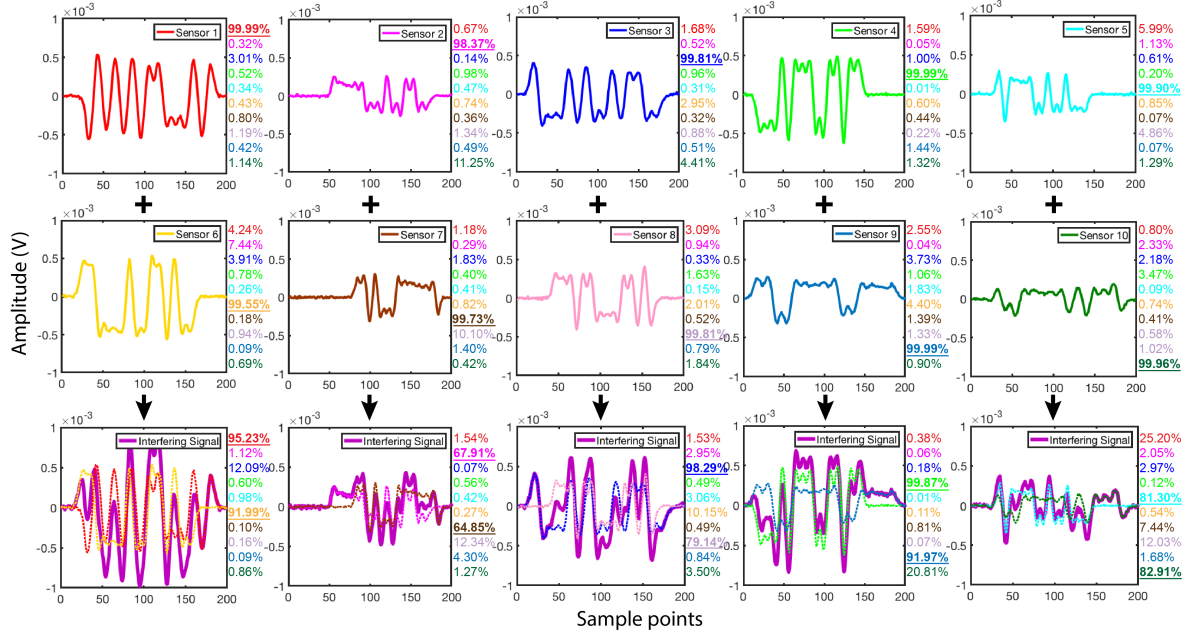
Figure 39 - ConvNet query of the second version deep learning model for the Microfluidic CODES. The first and second rows show the processing result for non-interfering signals. The third shows the processing result for interfering signals.

The query speed is over 800 particles/s, which represents an ~100× increase over the template-based algorithm (SIC) demonstrated in our earlier work. Query speeds of this order can potentially enable real-time particle analysis in LoC devices with code-multiplexed sensor networks.
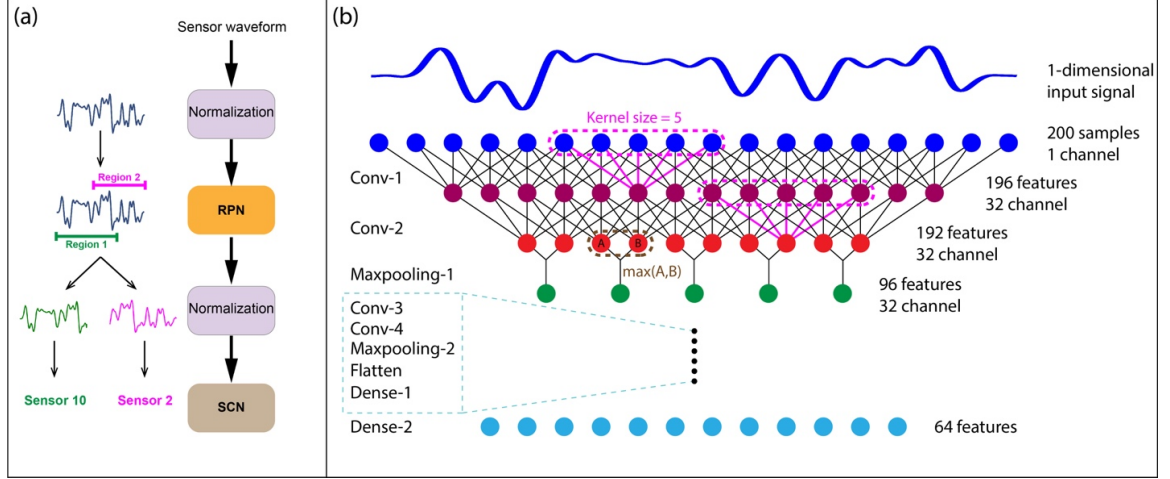
Figure 40 - Design of the two-stage ConvNet structure in the third version deep learning-based signal processing scheme for the Microfluidic CODES. (a) Signal processing workflow, where two ConvNet are trained to process the signal. (b) ConvNet structure.

3.3.5   Software Design (V3) - based on Region Proposal

3.3.5.1   ConvNet Design

In the third version deep learning model, to process the code-multiplexed Coulter sensor signal, we developed a two-stage ConvNet structure (Figure 40a). The first stage ConvNet is the region proposal network (RPN), which searches an input signal for regions (bounding boxes) that potentially contain signature waveforms. At the same time, the scale of each bounding box is used to estimate the amplitude and duration of the signature waveform providing information on the size and speed of the corresponding particle, respectively. The second stage ConvNet is the sensor classification network (SCN), which is trained to perform sensor-identity classification on signature waveforms extracted from the first stage. The SCN predicts the probability with which the input signature waveform belongs to each and every Coulter sensor in the network integrated on the microfluidic device.

82

Table 2 - ConvNet design parameters in the third version deep learning model for the Microfluidic CODES. The ConvNet contains four layers and a total of 217056 training parameters.

	C-size	C-Stride	C-pad	Act	P-size	P-stride	Params	O/P shape
Input	-	-	-	-	-	-	-	(200)
Conv-1	(5)	1	0	-	-	-	192	(32, 196)
Activation-1	-	-	-	ReLU	-	-	-	(32, 196)
Conv-2	(5)	1	0	-	-	-	5152	(32, 192)
Activation-2	-	-	-	ReLU	-	-	-	(32, 192)
Maxpooling-1	-	-	-	-	(2)	2	-	(32, 96)
Conv-3	(5)	1	0	-	-	-	10304	(64, 92)
Activation-3	-	-	-	ReLU	-	-	-	(64, 92)
Conv-4	(5)	1	0	-	-	-	20544	(64, 88)
Activation-4	-	-	-	ReLU	-	-	-	(64, 88)
Maxpooling-2	-	-	-	-	(2)	2	-	(64, 44)
Flatten	-	-	-	-	-	-	-	(2816)
Dense-1	-	-	-	-	-	-	180224	(64)
Activation-5	-	-	-	ReLU	-	-	-	(64)
Dense-2	-	-	-	-	-	-	640	(-)

The RPN and the SCN share the same structure for feature extraction (Figure 40b). We adapted our ConvNet structure from a work [207]. that aims pattern recognition in grayscale images. The structure is optimized using the Bayesian optimization algorithm [208]. We choose this structure due to several reasons: (1) We analogize the classification of sensor waveforms in an electrical signal to object recognition in an image frame; (2) Greyscale images have only one channel, like our electrical waveform and therefore the ConvNet can be compact for faster processing. Both of our ConvNets contain four convolutional layers, each of which is activated by a ReLU layer. A max-pooling layer is placed after the second and the fourth convolutional layers. Two dense layers are placed at last. The model has a total of 217056 trainable parameters. For reproducibility, detailed

information on our ConvNet design parameters is presented in Table 2.

3.3.5.2   Training Data Construction
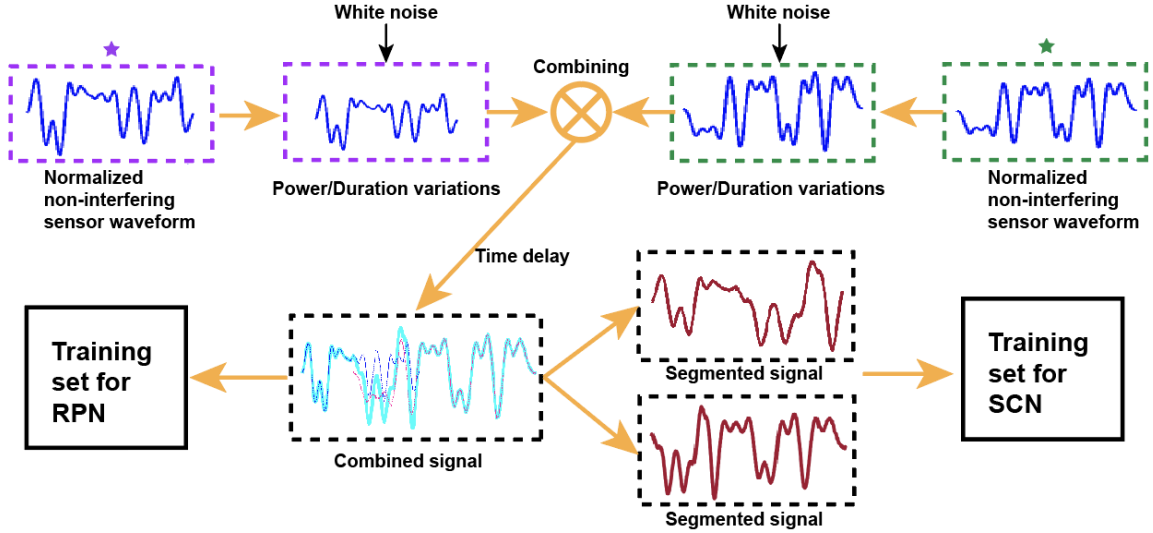
Figure 41 - Construction of training data of the third version deep learning-based signal processing scheme for the Microfluidic CODES.

Using the constructed non-interfering and interfering sensor waveform database, we created different training data for the RPN and the SCN because of the specific role each ConvNet played in the algorithm. For the RPN, the training data consists of non-interfering and interfering sensor waveforms directly from the database along with labels on waveforms' amplitudes and durations. For the SCN, the interfering sensor waveforms need to be pre-conditioned in the digital domain as if they are already processed by a "perfect" RPN because the RPN output is fed into the SCN in our algorithm. Specifically, this process involved extracting sections of an interfering sensor waveform such that the extracted section includes one of the signature waveforms in full along with parts of the contaminating waveform. The extracted section was then labeled with the sensor identity

corresponding to the full signature waveform, and it was used to train the SCN to identify the sensor in the presence of interference (Figure 41).

Table 3 - Hyper-parameters for ConvNets training in the third version deep learning model for the Microfluidic CODES.

	Loss function	Optimizer	Regularization	Learning rate	Momentum	Batch size	Epochs
RPN	MSE	SGD	N/A	0.001	0.9	500	50
SCN	Cross-Entropy	SGD	L2	0.001	0.9	500	50

3.3.5.3   ConvNet Training

We trained both ConvNets with a batch size of 500 and an epoch number of 50. In each iteration, we updated parameters by employing a stochastic gradient descent (SGD) optimizer. We used the grid search to determine the optimal combination of the learning rate and the momentum. In this process, the learning rate and the momentum was chosen from two different lists ([0.1, 0.01, 0.001, 0.0001, 0.00001] and [0.5, 0.9, 0.99], respectively), which were assembled based on typical values used in practice. For the PRN, we used the mean square error (MSE) to compute the error between actual bounding boxes and predicted bounding boxes. For the SCN, we used the cross-entropy to calculate the classification error. Furthermore, we employed an L2 regularization in training the SCN to prevent overfitting. Hyper-parameters for training the networks are shown in Table 3.
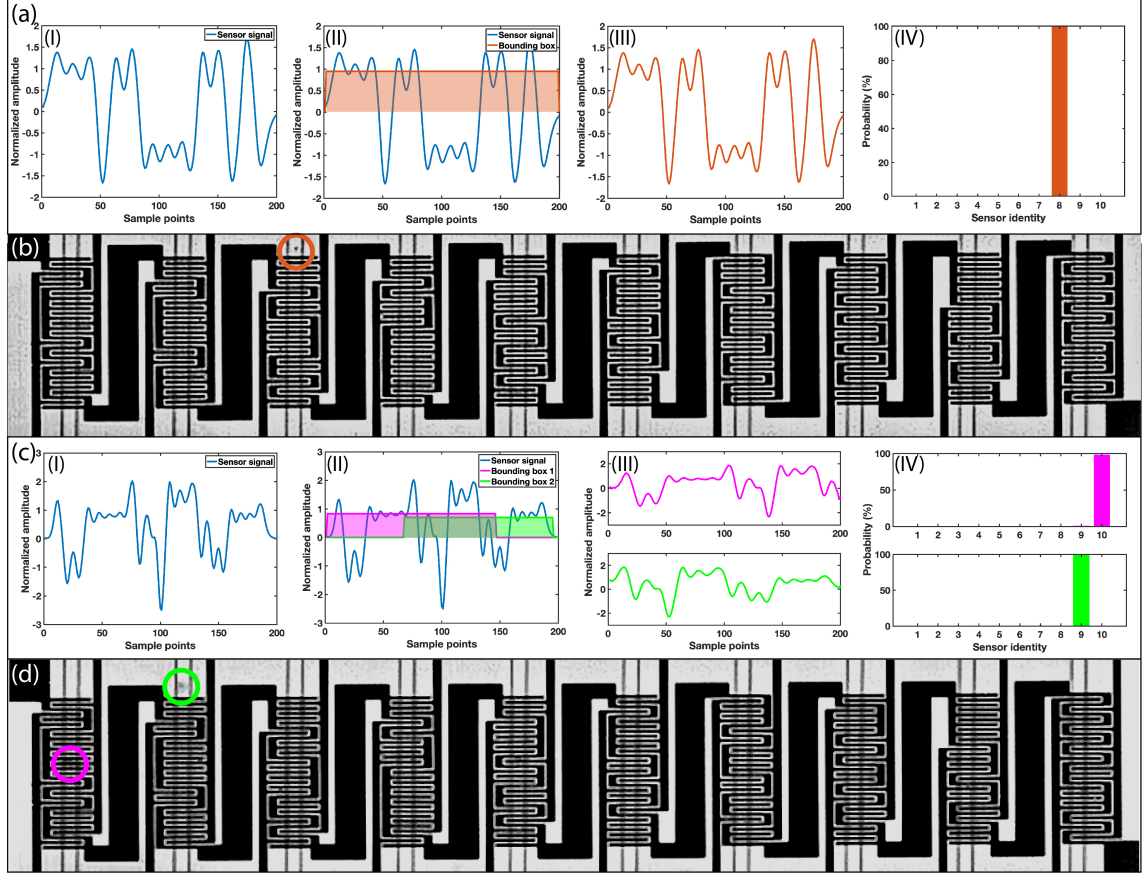
Figure 42 - ConvNet querying of the third version deep learning model for the Microfluidic CODES. (a) For a non-interfering sensor waveform, the RPN produces one bounding box that contains the signature waveform. The detected signature waveform is then extracted, normalized, and fed into the SCN. (c) For an interfering sensor waveform, the RPN produces two bounding boxes for two signature waveforms. The detected signature waveforms are then extracted, normalized, and fed into the SCN. (b)(d) Simultaneously recorded high-speed camera image confirms decoding result.

3.3.5.4 ConvNet Querying

Trained ConvNets are used to process experimental signals. For non-interfering sensor waveforms (Figure 42a, I), as the input contains only one signature waveform, the RPN only produces one valid bounding box (Figure 42a, II). Then the input signal is clipped according to the bounding box, and the extracted waveform is normalized in power (Figure 42a, III). The normalized waveform is fed into the SCN for sensor identity classification. The sensor identity is determined by the index of the output node with the highest

86

probability value (Figure 42a, IV). For interfering sensor waveforms (Figure 42c, I), multiple bounding boxes are identified (Figure 42c, II). The predicted bounding boxes have different lengths and heights, according to different durations and amplitudes of the detected signature waveforms, respectively. Similarly, the waveform in each bounding box is then extracted, normalized, and processed by the SCN (Figure 42c, III). The SCN then determines the identities of the two sensors that detect the cells and provides the confidence levels for its prediction (Figure 42c, IV). The algorithm predictions are validated using a simultaneously recorded high-speed video of the cell flowing in the device (Figure 42b & Figure 42d).
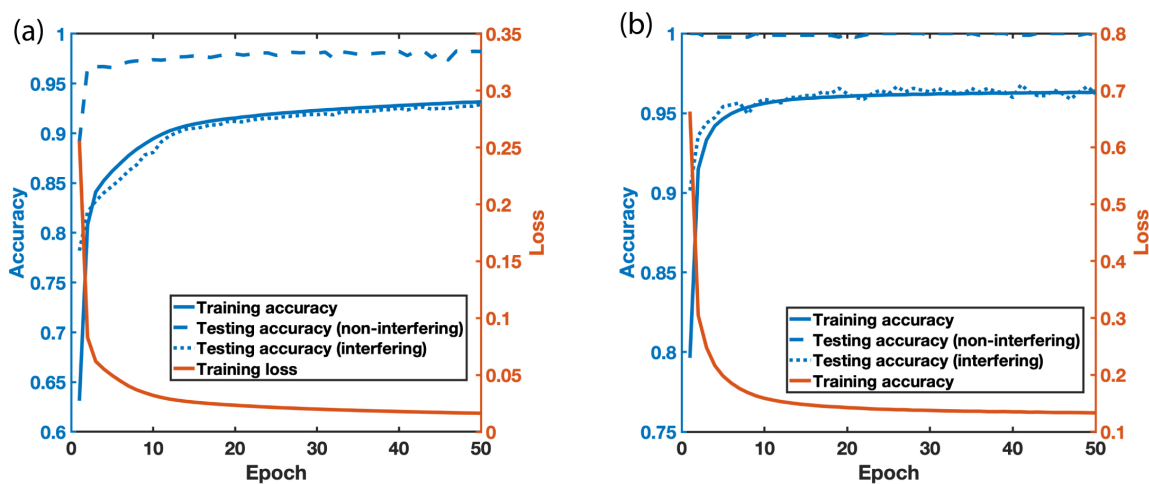
Figure 43 - ConvNet (a) training and (b) testing accuracy and loss of the third version deep learning model for the Microfluidic CODES. Each ConvNet is trained for 50 epochs.

3.3.5.5 ConvNet Testing

To test the ConvNets, we first constructed two testing datasets, one for single cells and another for coincident cells. Each of these sets contains signature waveforms from 900 cells. Each ConvNet is then tested separately with these two testing datasets for non-interfering and interfering sensor waveforms. For the RPN, the bounding box regression

accuracy on non-interfering sensor waveforms is higher than that on interfering ones (Figure 43a). This difference is expected as the bounding box for a non-interfering sensor waveform is the entirety of the input sensor waveform with only one signature waveform present. In contrast, for an interfering sensor waveform, the interference between signature waveforms results in less predictable boundaries, leading to lower accuracy. We observe that the accuracy of the RPN for both non-interfering and interfering sensor waveforms increases with the training epoch number and remained stable after 45 epochs (Figure 43a). We achieve a final testing accuracy of 97% on non-interfering sensor waveforms, and 92% on interfering sensor waveforms at epoch 50.
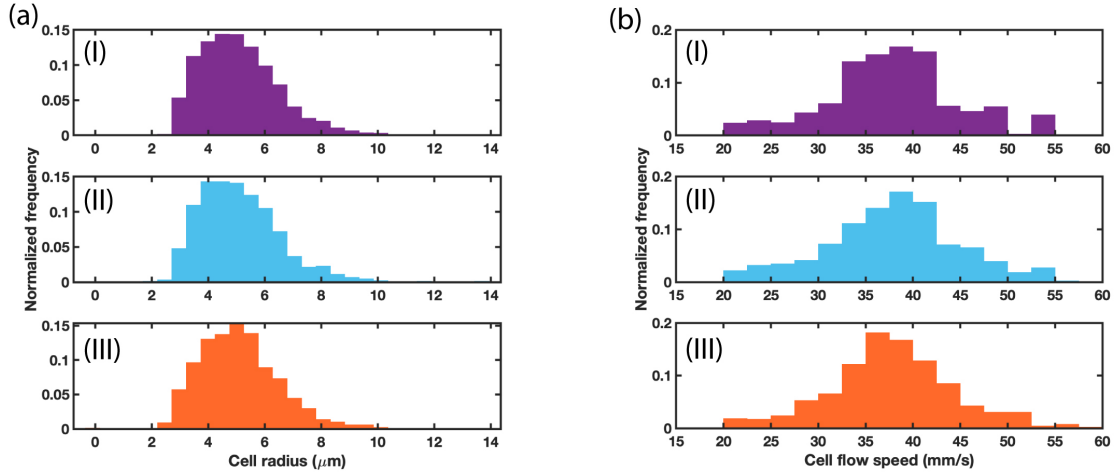
Figure 44 - ConvNet testing of size and speed prediction of the third version deep learning model for the Microfluidic CODES. Distributions of (a) Cell size and (b) cell flow speed are given.

Heights of the predicted bounding boxes were used to estimate sizes of detected cells. Because the height of each predicted bounding box corresponds to the amplitude of the identified signature waveform, it could be used to determine the cell volume, according to the Coulter principle. Following the calibration of signal amplitude for cell size using microscope images, we compared algorithm predictions with the actual size data directly

88

calculated from the testing data. To observe potential effects of interference-induced error in size estimation, we analyzed non-interfering (Figure 44a, I) and interfering (Figure 44a, II) sensor waveforms separately and observe that resulting size distributions closely match with each other. Furthermore, the size measurements from our algorithm also agree well with the size distribution directly calculated from the testing data (Figure 44a, III).

For the speed estimation, we used the length of each predicted bounding box, which corresponds to the duration of the identified signature waveform. Because the duration of the waveform provides the residence time of a flowing cell in the sensing region, by combining the waveform duration with the physical length of the coded sensor, we could calculate the speed of each cell. Using our algorithm, we calculated the flow speed for single (Figure 44b, I) and coincident (Figure 44b, II) cells separately. The calculated speed distributions for both tests match, demonstrating the negligible effect of sensor interference on cell speed estimations. The results are also in close agreement with the speed data (Figure 44b, III) directly calculated from the testing data.
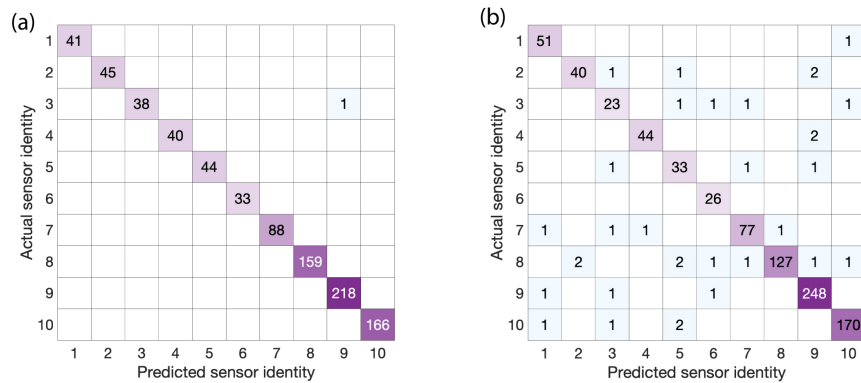
Figure 45 - Confusion matrix of the sensor identity prediction of the third version deep learning model for the Microfluidic CODES. (a) Prediction for non-interfering signals. (b) Prediction for interfering signals.
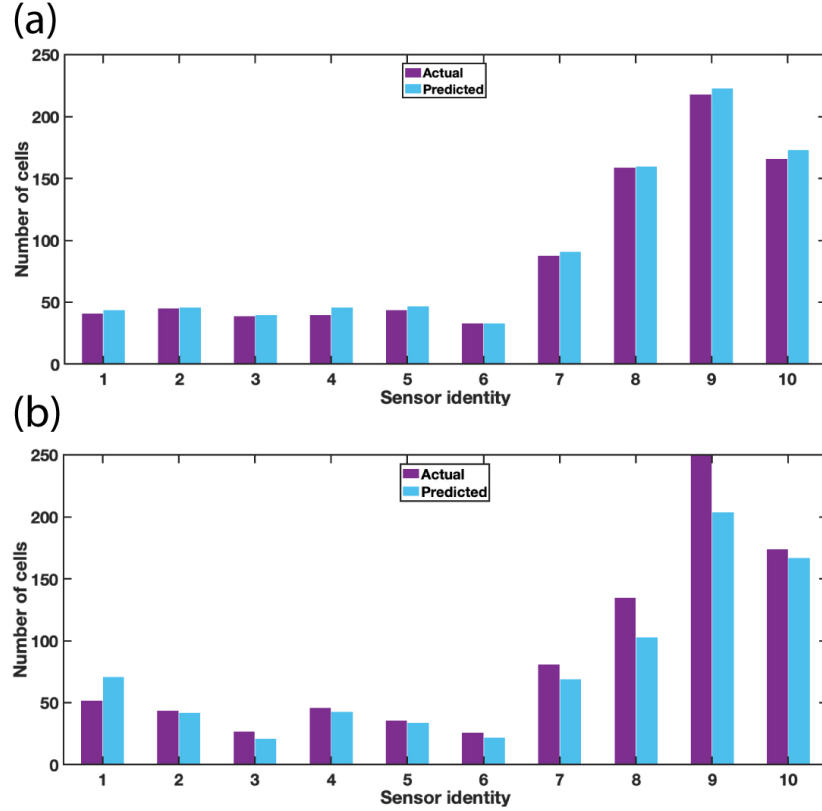
Figure 46 - Testing the ConvNets by cascading the RPN and SCN of the third version deep learning model for the Microfluidic CODES. (a) Prediction for non-interfering signals. (b) Prediction for interfering signals.

For the sensor identity estimation, we first tested SCN alone to test its accuracy in sensor identity classification for non-interfering and interfering sensor waveforms. The classification accuracy for non-interfering sensor waveforms is found to be higher than that of interfering ones (Figure 43b). This difference is expected because a non-interfering sensor waveform faithfully followed the pattern of the assigned code sequence. While deviations could result from differences in shape, size, and vertical position of a cell, those are often not at a level to negate the underlying signature waveform. However, for an interfering sensor waveform, part of a signature waveform is by definition distorted by contaminating signature waveforms. The partial deviation could be significant enough, especially if the interfering cell is larger, to dominate the signature waveform pattern and

90

lower the classification accuracy. Nevertheless, we achieved a testing accuracy of 99% for non-interfering sensor waveforms, and 95% for interfering sensor waveforms. Furthermore, confusion matrices for the tests of non-interfering (Figure 45a) and interfering sensor waveforms (Figure 45b) do not present a misclassification bias for any specific sensor combination.
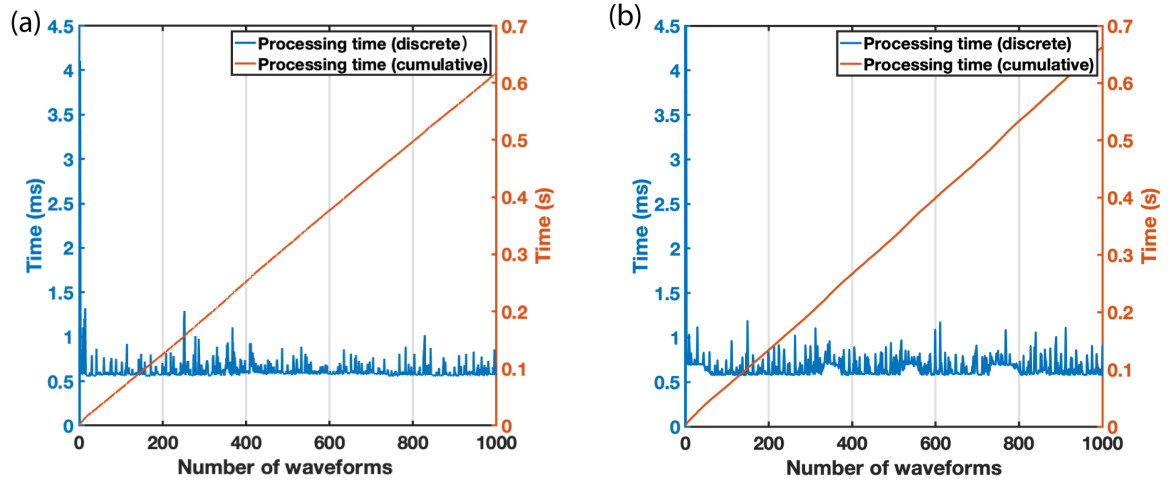
Figure 47 - Signal process speed of (a) RPN and (b) SCN of the third version deep learning model for the Microfluidic CODES. On average, the RPN required ~610 ms, and the SCN required ~670 ms, to process 1000 input waveforms.

We completed the testing of our algorithm by cascading the RPN and the SCN. In this setting, each testing signal is first processed by the RPN, and the extracted signature waveforms are then classified by the SCN. The accuracy was calculated by comparing the total number of cells detected by each code-multiplexed Coulter sensor (sensor identity distribution) with the known number of each signature waveform in the testing data (Figure 46a & Figure 46b). We achieved an accuracy of 97% for single cells and 85% for coincident cells. The overall testing accuracy for the cascaded ConvNets (i.e., the complete algorithm) is less than the calculated accuracy for a single ConvNet due to the propagation of the error. Specifically, the bounding-box estimation errors that occur in the first stage

(RPN), including occasional missing of low-power signature waveforms in interfering sensor waveforms, propagated to the second stage (SCN), resulting in reduced classification accuracy.

The processing speed is an essential factor when evaluating an algorithm. To estimate the processing speed, we used each ConvNet to process 1000 input waveforms and record the unit processing time for each input (Figure 47a & Figure 47b). We also calculated the cumulative time elapsed as each ConvNet processed those 1000 waveforms. As the RPN and the SCN share the same structure (same number of parameters), they have similar processing speeds. On average, the RPN required ~610 ms, and the SCN required ~670 ms, to process 1000 input waveforms. Based on these metrics, the two-stage ConvNet structure could process 780 cells per second (2.7 GHz Intel Core i7, Intel). Processing speeds of this order can potentially make real-time analysis possible for a variety of sample types.

To interpret the trained ConvNets, we also visualized the learned parameters of kernels in each convolutional layer. The kernels in the first two convolutional layers (Figure 48) learn first-order features in a coded sensor waveform such as orientations and amplitudes of individual pulses. In deeper convolutional layers, the patterns of kernels become more complex, indicating that the last two layers represented more abstract information, including slopes and transitions between two adjacent pulses (Figure 49). This observed hierarchical representation matches with the fact that a ConvNet interprets input as a hierarchy of features with increasing abstraction. In our ConvNet, a few kernels in deeper layers showed noisy patterns, indicating these kernels are not activated given the specific training data.
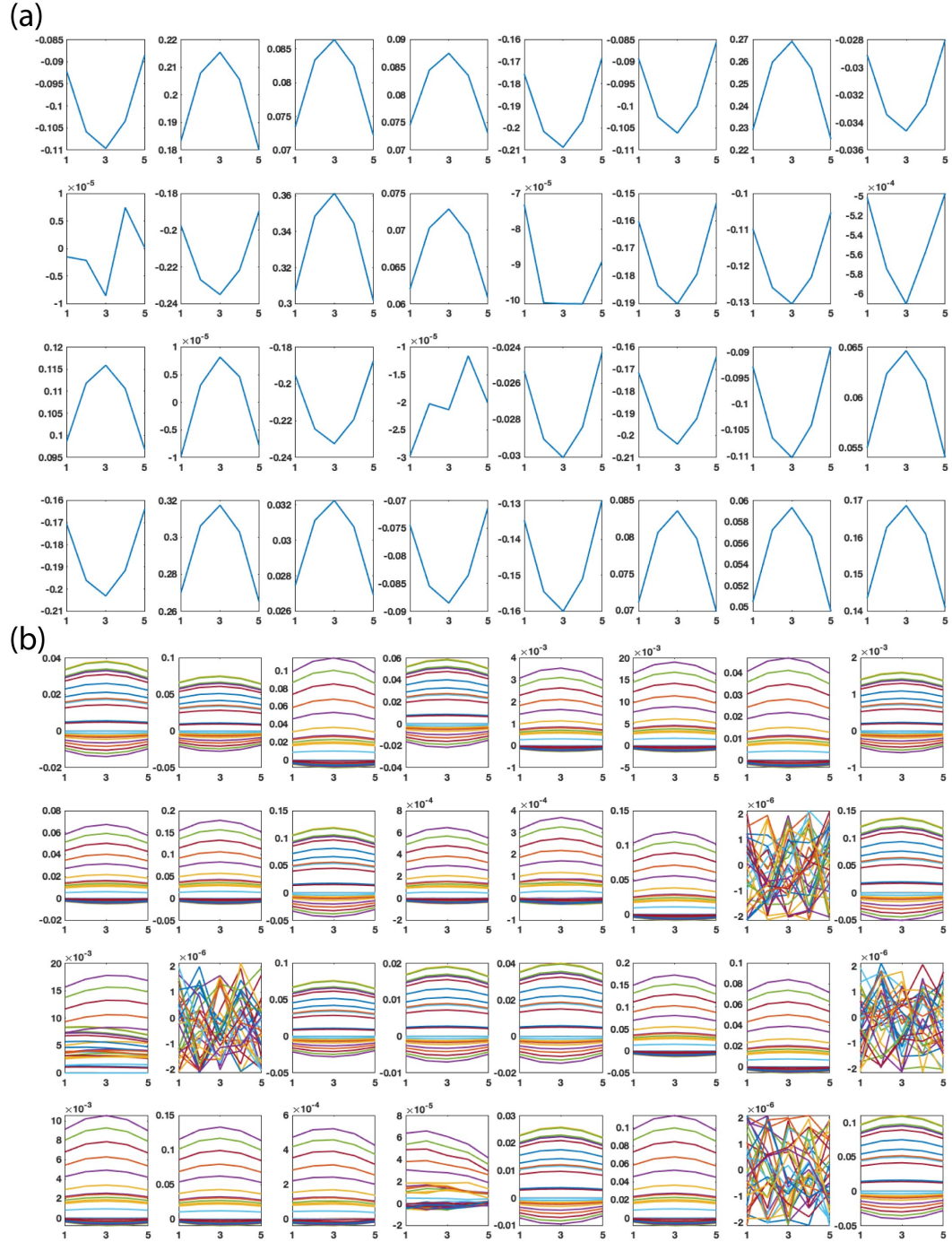
Figure 48 - ConvNet weight visualization (Conv-1 and Conv-2) of the third version deep learning model for the Microfluidic CODES

(c)

(d)
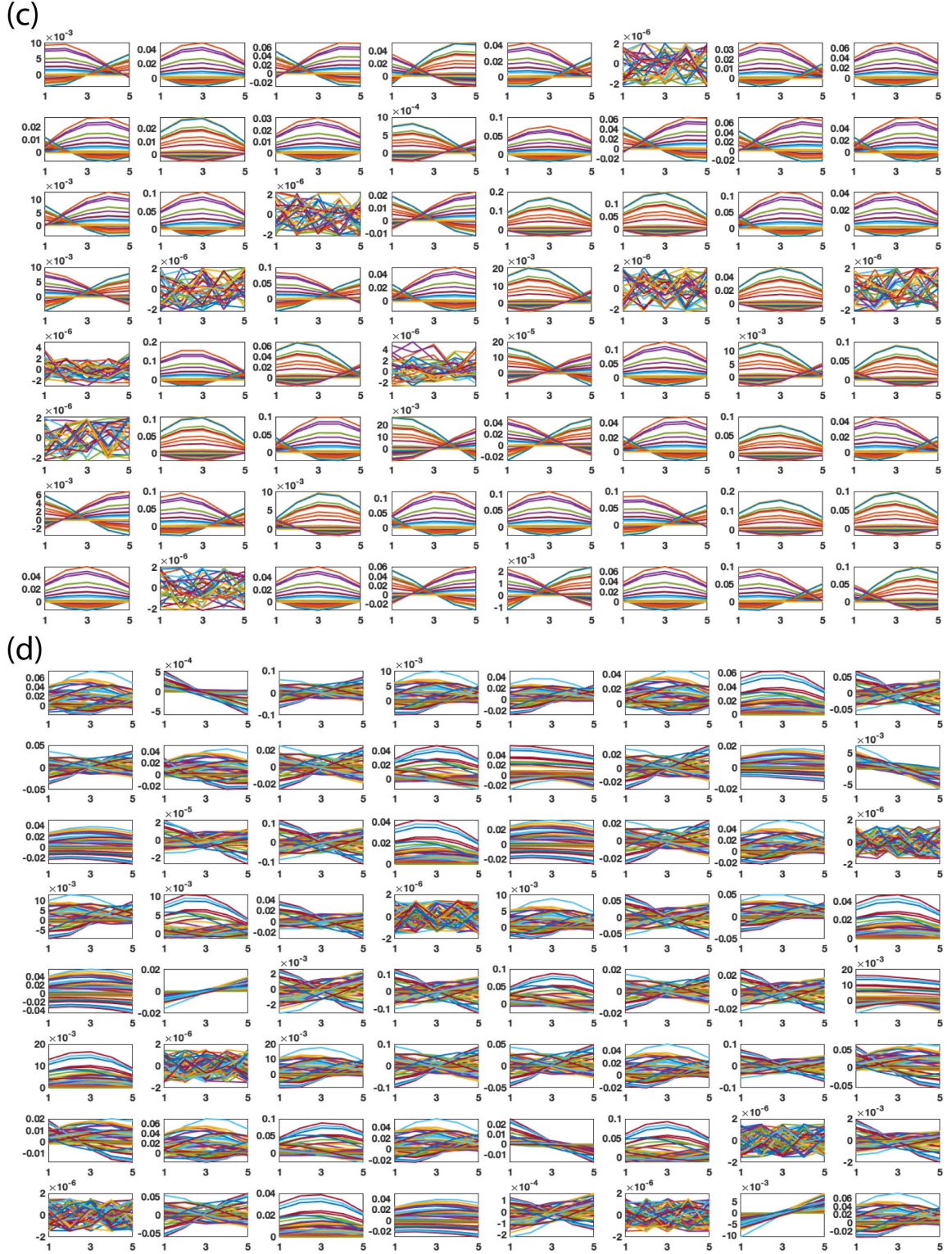
Figure 49 - ConvNet weight visualization (Conv-3 and Conv-4) of the third version deep learning model for the Microfluidic CODES.
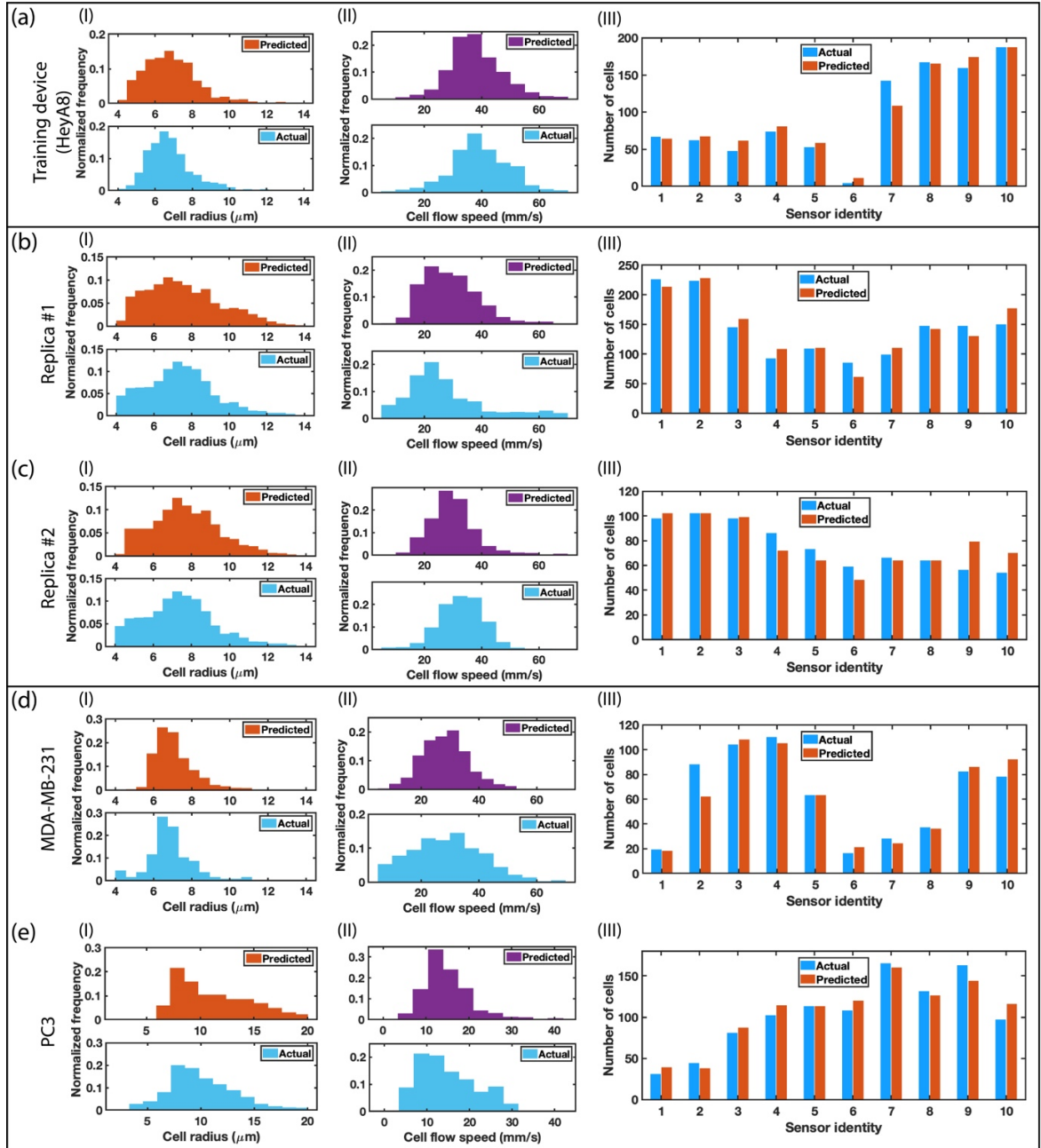
Figure 50 - ConvNet validation via optical imaging of the third version deep learning model for the Microfluidic CODES. (a) Validation of the original device. (b) Cross-platform validation by using replicate devices. (c) Cross-cell line validation by using two new cell lines (MDA-MB-231 and PC3).

3.3.5.6 ConvNet Validation via Optical Imaging

To independently validate the performance of our algorithm, we compared the algorithm results with a simultaneously recorded high-speed (1000 fps) microscopy video footage of human cancer cells flowing through the microfluidic device. The video is recorded by placing all the sensors within the same field of view so that the whole sensor network activity can be visually acquired. By processing the recorded video of ~1000 cells by a custom-built image-processing program, speed and the sensor identity for each cell are automatically determined. Cell size distribution is obtained in a separate experiment by imaging cells of the same type and processing the recorded images with the ImageJ software. Microscope-measured cell size (Figure 50a, I) and cell speed (Figure 50a, II) histograms closely match with the prediction. Besides algorithm-induced errors, the differences from optical measurements of cell properties are expected to be due to several factors: (1) the cells used for imaging might have had a different size distribution from the cells detected by the device even though they are sampled from the same tissue culture; (2) accuracy in cell size measurements might have suffered from calibration errors as well as the sensor-proximity effects in the microfluidic channel; (3) optical cell speed measurements with the high-speed camera are prone to errors from low spatial and temporal resolution. In terms of the sensor identity prediction, our algorithm is able to identify the correct sensor with an overall accuracy of 90.3% (Figure 50a, III). These results validated the ability of our algorithm to accurately capture the microfluidic activity of the cells and their characteristics.

96

3.3.5.7   Cross-platform ConvNet Validation

To be of practical utility, trained ConvNets should be directly applicable to signals from other LoC devices with identical sensor designs. Furthermore, using the same device to generate both the training and testing signals might artificially enhance the measured accuracy of our algorithm. Therefore, we tested the cross-platform operability by training our algorithm on data from one device and testing its performance on other devices. For this purpose, we fabricated two microfluidic devices, which were replicas of the original device (the training device) we used in this study. Even though all the three devices have the same electrode design, their signature waveforms for each Coulter sensor were expected to show observable differences due to variations from the fabrication processes and the electrical contacts.

We processed ~1000 human ovarian cancer cells sampled from the same PBS suspension with each replica microfluidic device. High-speed microscopy videos are recorded as a benchmark to determine the cross-platform accuracy of our algorithm. The videos were processed, and microscopy measurements were compared with the algorithm predictions for the cell size, cell flow speed, and sensor identity. For both replica devices, the microscope-measured cell size (Figure 50b, I & Figure 50c, I) and flow speed (Figure 50b, II & Figure 50c, II) distributions match closely with algorithm results, yielding similar mean and variance. As for sensor identities, we achieved 90.65% (Figure 50b, III), and 89.42% (Figure 50c, III) accuracy on Replica #1 and Replica #2, respectively. Taken together, these results demonstrate the robustness of our trained ConvNets against cross-platform waveform variations, leading us to the conclusion that a pre-trained network could

directly be used to interpret sensor signals from different microfluidic designs, as long as the same set of code sequences is used in the sensor network.

3.3.5.8   Cross-cell type ConvNet Validation

To be used in a variety of applications, trained ConvNets should be directly applicable to signals generated by any cell types. Therefore, we tested the cross-cell type compatibility of our technique by applying our ConvNet, trained with human ovarian cancer cells (HeyA8) to interpret signals from the processing of human breast (MDA-MB-231) and prostate (PC3) cancer cell lines. For these measurements, we fabricated two identical microfluidic devices (replicas of the training device) and separately processed the two cell lines on these devices. Simultaneously-recorded high-speed microscopy videos are treated as the ground truth to calculate the cross-cell type accuracy. For both cell lines, the microscope-measured cell size (Figure 50d, I & Figure 50e, I) and flow speed (Figure 50d, II & Figure 50e, II) distributions matched closely with algorithm results, yielding similar mean and variance. As for sensor identities, we achieved 89.76% (Figure 50d, III), and 91.11% (Figure 50e, III) accuracy on MDA-MB-231 and PC3, respectively. These results demonstrate the compatibility of trained ConvNets with different sample types and the potential of our technique for general-purpose cytometry application.

3.4   FDMA-based Processing of Microfluidic CODES Signal

We also investigated the implementation of FDMA in decoding our sensor signals. Besides CDMA, FDMA is another effective way for signal multiplexing in digital communication systems. In an FDMA system, each source signal is allocated in a distinct frequency range. Therefore, even though all the source signals are transmitted within a

single transmission channel at the same time, no overlapping happens among them in the frequency domain. Therefore, we can use filter to extract the information in each frequency band.

We have introduced an adaptation of Microfluidic CODES, which combines CDMA with FDMA, to multiplex detection of particles with an electrical sensor network. However, we were not simply driving each sensor using an excitation signal with a distinct frequency, we actually introduced frequency differences by designing the electrode pattern.

In our sensor network, all sensors were interconnected and monitored from a single electrical output. For multiplexing the sensor data, each sensor was designed to generate a distinct waveform when it detected a particle. We specifically designed the sensor structure so that signals from individual sensors had distinguishable frequency spectra. Therefore, frequency-domain analysis of the output signal can be used to determine which sensor in the network is activated in a given time window. In the case of coincident particles causing multiple sensors to be activated simultaneously, each sensor effectively operates in a non-overlapping frequency band, allowing us to resolve individual sensor signals (Figure 51).
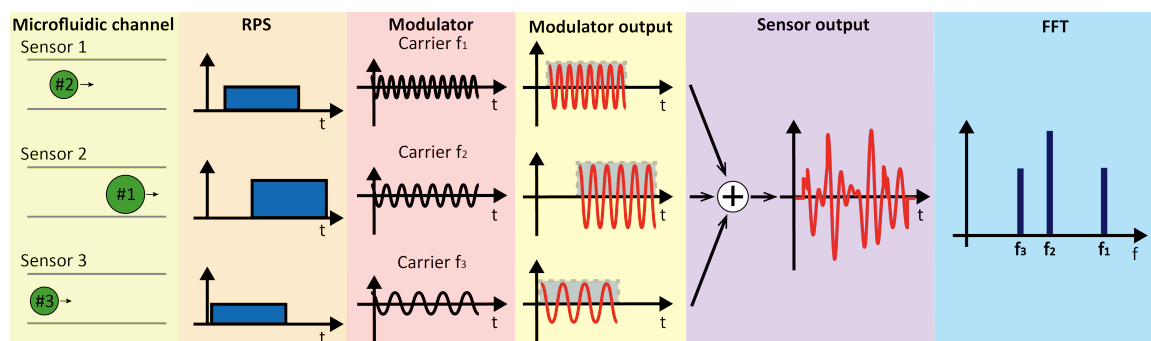
Figure 51 - Concept illustration of the FDMA-based processing of the Microfluidic CODES. The signal generated from each sensor is designed at a specific frequency band.
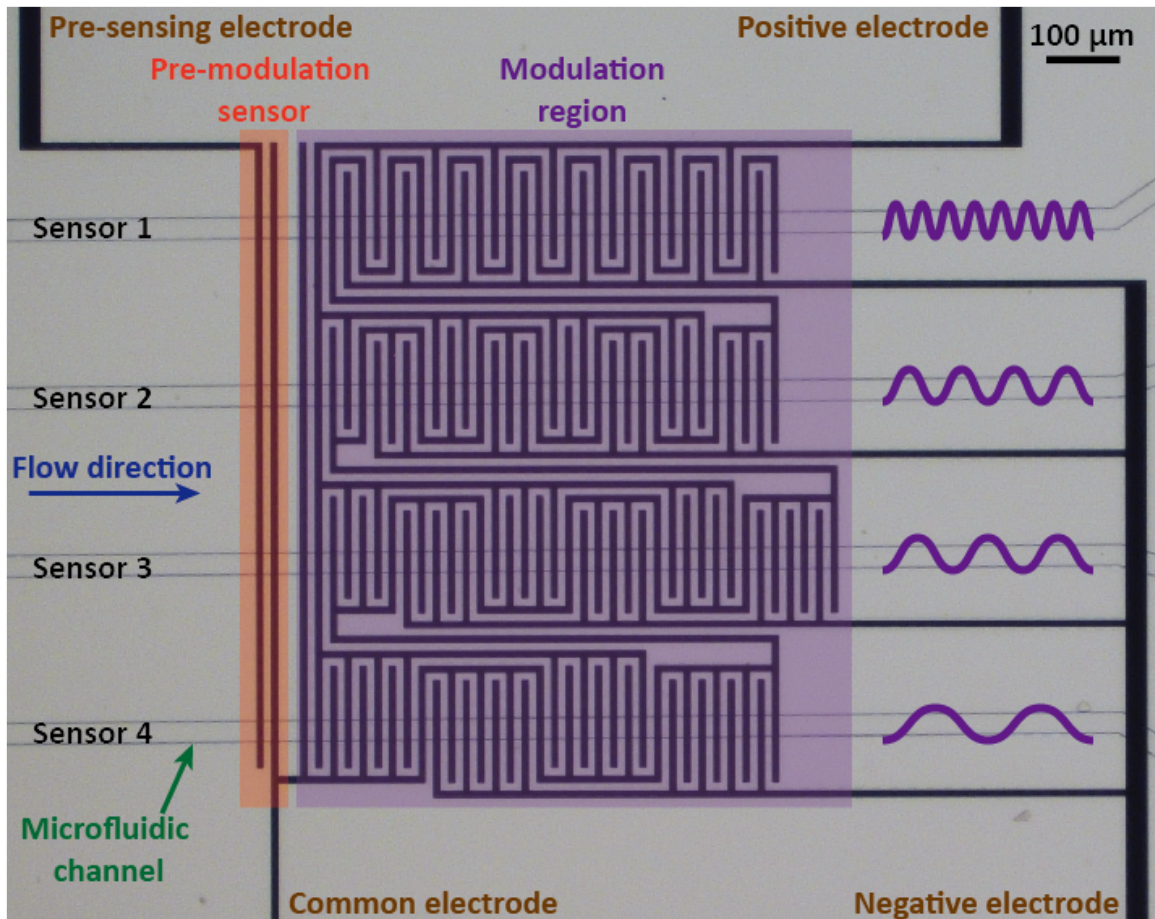
Figure 52 - Electrode design of the Microfluidic CODES using FDMA-based processing. By designing the electrode pattern for each sensor, the signal generated from each sensor is designed at a specific frequency band.

3.4.1 Hardware Design

As a proof of principle, we created a network of four sensors (Figure 52), by designing the electrode patterns with different spatial frequencies, we effectively allocated a distinct temporal frequency band to each sensor. Besides the electrode spatial pattern, the frequency spectrum of any individual sensor signal was determined by the flow speed of

the detected particle. To measure the flow speed, our device included a pre-modulation sensor that was shared by all sensors in the network. We use a machine learning model based on the KNN algorithm to estimate the speed of the particle. Once we knew particle speeds present in the system, we used this information in the decoding process to predict possible frequency spectrum for individual sensors and searched for them in the output signal spectrum.
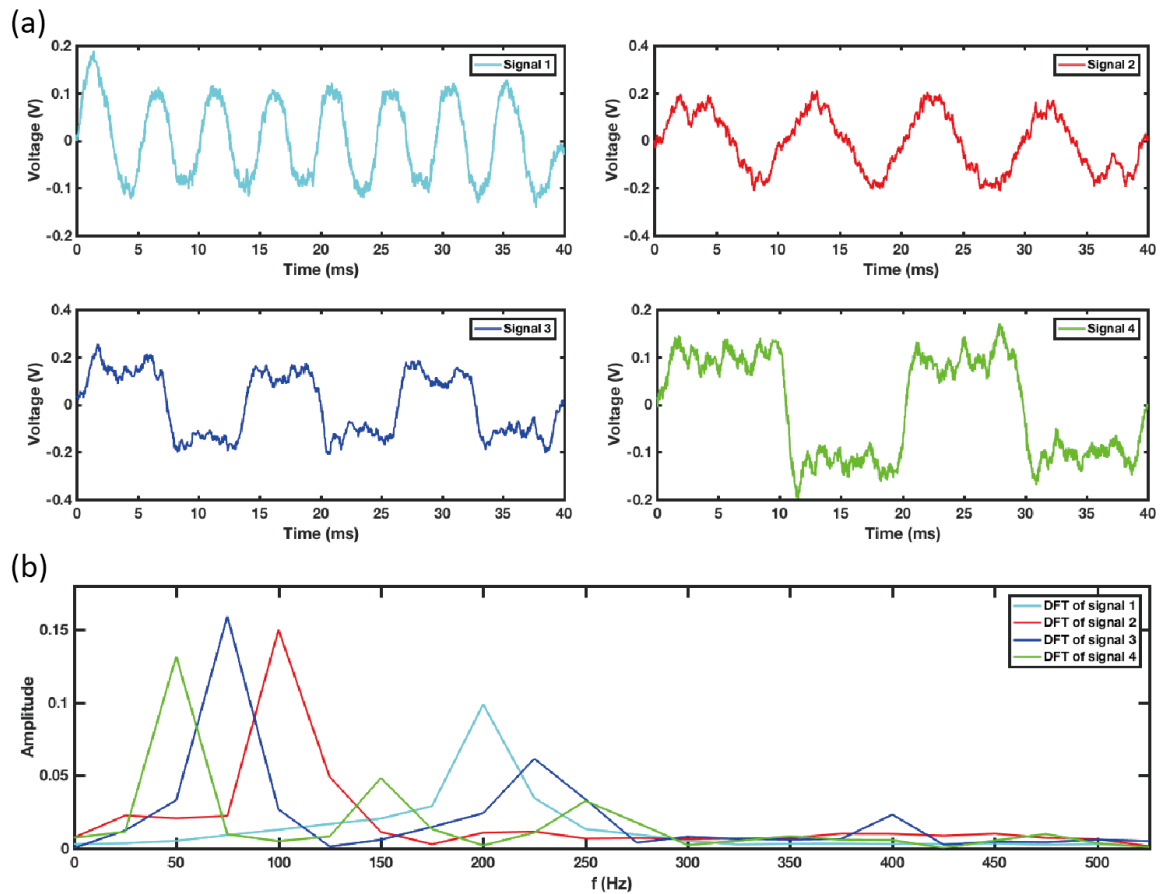
Figure 53 - Sensor signal of the Microfluidic CODES using FDMA-based processing. (a) Sensor signal from each sensor shows different frequency. (b) Discrete Fourier transform (DFT) for each sensor signal shows distinct peaks.

(a)

(b)
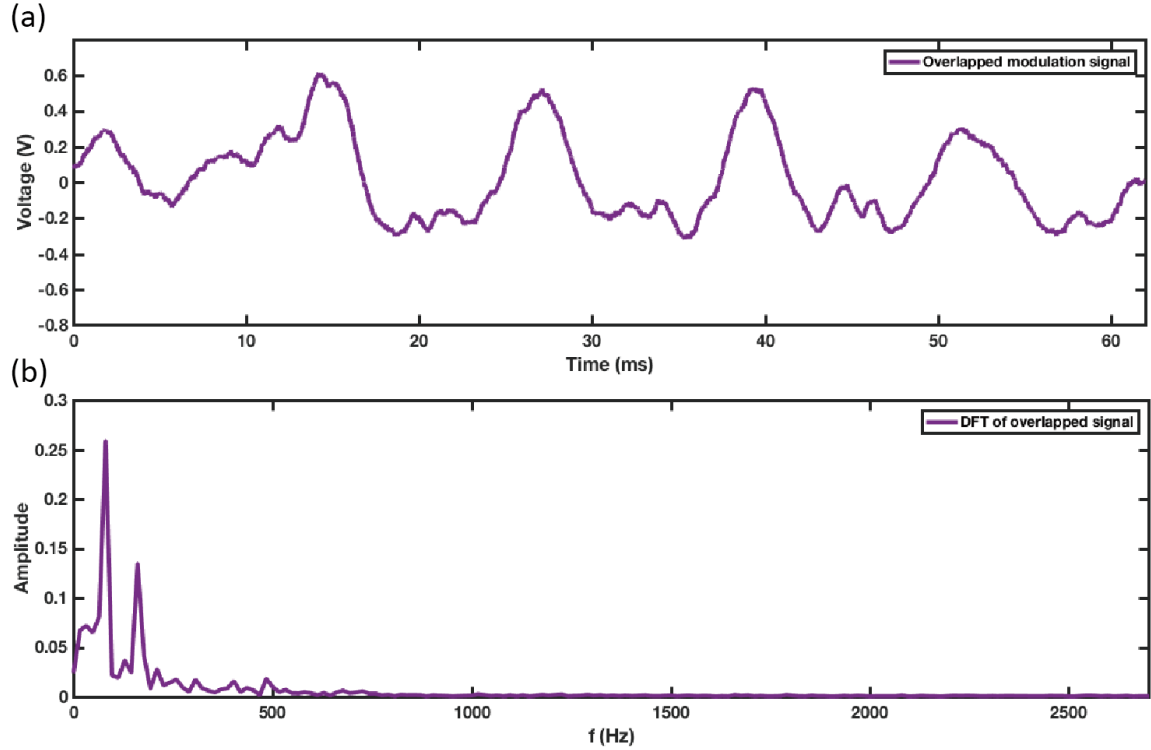
Figure 54 - Sensor signal processing of an interfering signal of the Microfluidic CODES using FDMA-based processing. (a) An interfering sensor waveform with 2 cells. (b) DFT shows two peaks.

3.4.2 Software Design

Figure 53 shows that individual sensor signals can be discriminated in the frequency domain. An important feature of our technology is that it can resolve cells in microfluidic channels when they coincide in the sensing volume. Here, we demonstrate a case in Figure 54, where we resolve two coincident cells. We determine from two peaks in the frequency spectrum that the cells are in the first and second sensors.

3.5 ICA-based Processing of Microfluidic CODES Signals

The figure shows Input 1 and Input 2 signal plots on the left feeding into an "Independent Component Analysis (ICA)" box, with the equations:

$$x_1(t) = a_{11}s_1 + a_{12}s_2$$
$$x_2(t) = a_{21}s_1 + a_{22}s_2$$

and outputs Independent Component 1 and Independent Component 2 on the right.
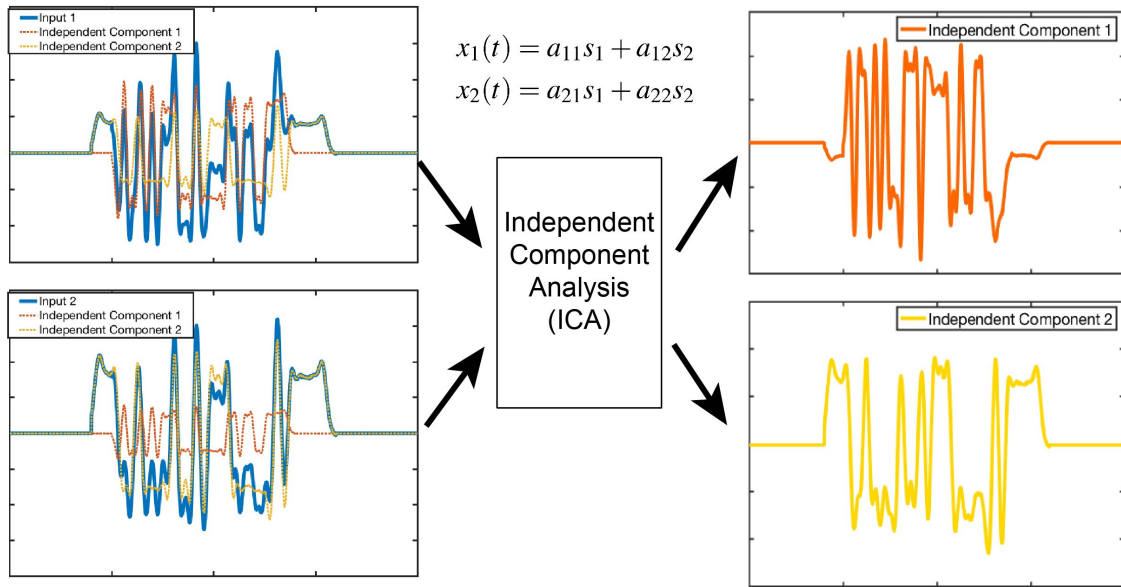
Figure 55 - Concept of the ICA-based processing for the Microfluidic CODES. Independent component analysis (ICA) is used for signal separation.

We also investigated the implementation of ICA in decoding our sensor signals. The ICA is a mathematical method for separating a multivariate signal into additive components. In ICA, we assume that the multivariate signal is a linear combination of components that are statistically independent. As shown in Figure 55, each of the two input signals is a linear combination of two source signals, s_1 and s_2, and ICA can extract the two independent sources by processing the inputs.

3.5.1 Hardware Design

To test the algorithm, we used the 10-channel (sensor) 31-bit Gold code Microfluidic CODES device (Figure 7) for characterization. It should be noted that, ICA

103

does not rely on the orthogonality among spreading codes, and here we just used this device as an example to demonstrate the work.
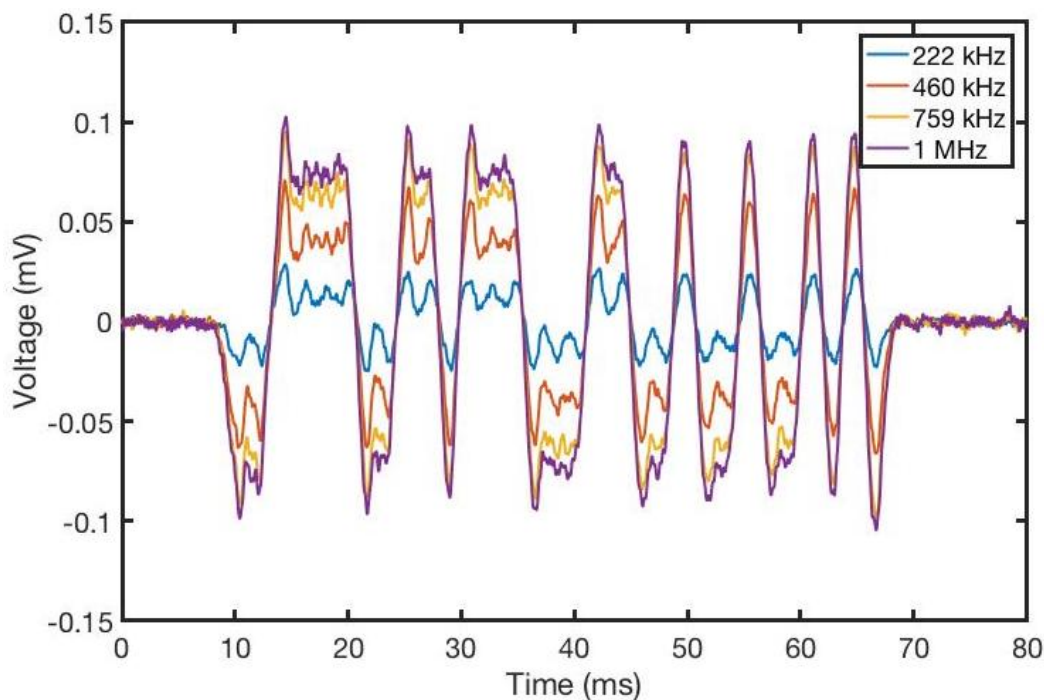
Figure 56 - Sensor signal of the ICA-based Microfluidic CODES. With four signals with different amplitudes at four excitation signals.

We prepared a suspension of MDA-MB-231 human breast cancer cells in phosphate buffer saline (PBS) to test the device. The cell suspension was loaded into a syringe and driven into the device using a syringe pump. At the same time, we used a lock-in amplifier (HF2LI with multi-frequency option) to excite the common electrode with a multi-frequency signal that contained signals in 4 frequencies (222 kHz, 460 kHz, 759 kHz, and 1 MHz), but with the same amplitude. Then we recorded the sensor output and demodulate the output with 4 independent oscillators to extract the signal in each frequency. Figure 56 shows sensor signals for one MDA cell corresponding to 4 frequencies.
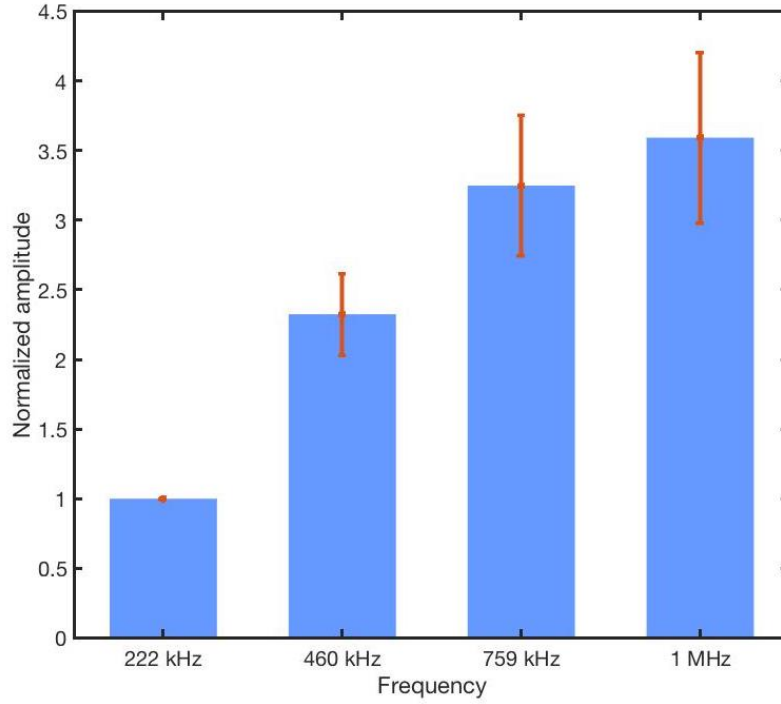
Figure 57 - Frequency response of MDA cells. At different frequency, signal amplitudes show different error bars.

3.5.2   Software Design

By processing sufficient number of cells, we generate the frequency response of MDA cells (Figure 57). We could see that the larger the excitation frequency, the cells induce signal with larger amplitudes.

When two sensors are activated at the same time (Figure 58a), we fed multi-frequency overlapping signals into the ICA and separated the two subcomponents (Figure 58b). Then by correlating these two subcomponents with signal of each sensor, we detected the auto-correlation peak and determined the activated sensors.
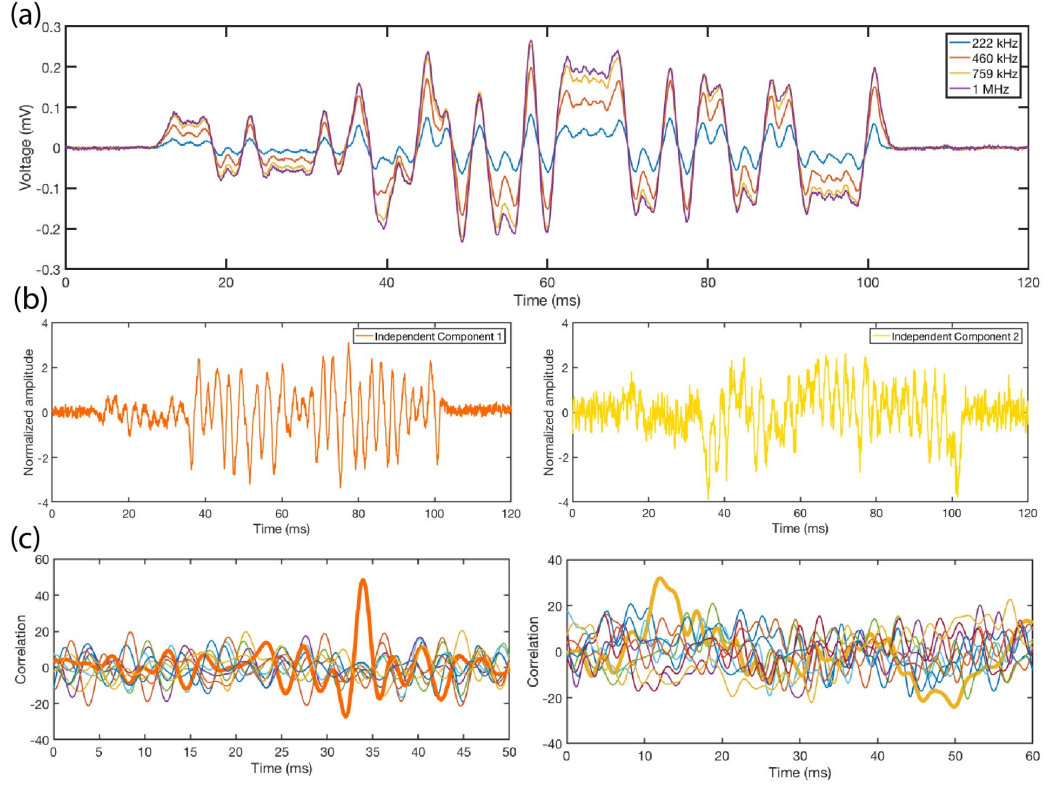
Figure 58 - Sensor signal processing using ICA for the Microfluidic CODES. (a) An interfering signal acquired with four frequencies. (b) Signal separated by ICA. (c) Using correlation to acquire the identity of the signal.

3.6 Discussion

Combining the techniques from telecommunications, signal processing, and microfluidics, we have introduced the microfluidic CODES technology, a scalable electronic sensing platform to detect particles in multiple locations on a microfluidic device from a single electrical output. The microfluidic CODES relies on multiplexing an array of micromachined Coulter counters, each designed to produce a distinct digital code when a particle is detected. Furthermore, a signal process algorithm is designed to process sensor output.

The design of the signal processing algorithm (for demultiplexing) also relies on the design of the signal multiplexing scheme. Based on the spreading codes used for encoding each sensor, the signal processing algorithm should not only be able to address the difference between different spreading codes, but also identify them when they interfere and deform. Based on the specific multiplexing/demultiplexing principle, we have mainly introduced three versions of signal processing schemes for the Microfluidic CODES technology, namely the correlation-based, the error-correction-based, and the deep learning-based scheme. We demonstrated that our technology could readily be applied to detect human cancer cells on a multi-channel microfluidic chip. Importantly, our technology can also resolve particles with a high accuracy if they overlap in time, a feature that is required to process samples with a high particle density. Microfluidic CODES offers a simple, all-electronic interface for tracking particles on microfluidic devices and is particularly well suited to create integrated, low-cost cytometry for cell- or particle-based assays that are needed for point-of-care tests in resource-limited settings.

Through theoretical analysis, we also investigated the effect of sensor signal interference due to coincident cells on the performance of the signal processing algorithm [193]. In an interfering sensor waveform, interference from one sensor appears as the noise of another sensor, leading to lower SNR. Eventually, interferences lead to errors in the decoding process. We mathematically modeled the relationship between the interference among different sensors and its effect on the bit error rate and then estimated the error rate as a function of expected coincident cells. Generally, as the number of coincident cells increases, the bit error rate also increases. Furthermore, as the expected number of coincident cells depends on the product of sensing volume and the particle concentration

(i.e., number of cells per unit volume), we also calculated the error rate as functions of sample and device properties.

The aforementioned modeling analysis not only estimated the device performance when processing different samples, but also provide proper guidance in designing the sensor platform. Generally, when designing the spreading codes, several aspects need to be considered. First, each code should be distinct, so that it can be used as a signature for each distributed sensor. Second, the length of the codes should not be too long, as longer codes will not only increase the complexity of the coplanar electrodes but also enlarge the volume of the sensing region. When the sensing volume increases, the expected number of coincident cells in the sensing region, which is the product of sensing volume and the particle concentration (i.e., number of cells per unit volume), also increases. The increasing number of coincident cells will further increase the error rate of the signal processing algorithm. Therefore, when designing the algorithm, we focus on the goal of using shorter spreading codes and designing signal processing algorithms with lower error rates and higher processing speed. On the other hand, the particle density can be tuned through dilution to achieve a target error rate for a given sensor network design.

Microfluidic CODES-based cytometers have several advantages over conventional cytometers. First, compared to traditional impedance-based flow cytometers that only count and size cells, the Microfluidic CODES also tracks the location of manipulated cells, providing another dimension of information for cell analysis. Second, the Microfluidic CODES can measure any cell property, not necessarily measurable by a conventional cytometer, as long as the cell property can be used for differential microfluidic manipulation. Third, the use of electrical sensors instead of optical detection allows system

108

integration and miniaturization to realize low-cost and portable systems that can perform as accurately as conventional systems. Finally, compared to imaging-based cytometry, which can also provide spatial information on cell manipulation, the Microfluidic CODES (1) offers a nonrigid "field of view" that can be tuned to any microfluidic platform for cell manipulation, (2) has a higher sub-millisecond temporal resolution, which can only be matched by specialized high-speed camera systems and (3) can efficiently compress spatial measurements on cells into an electrical waveform that could be processed more efficiently than video footage.

CHAPTER 4. MICROFLUIDIC CODES-BASED FEEDBACK CONTROL SYSTEM

While highly effective in manipulating cells, microfluidic devices are designed and experimentally optimized to operate under well-controlled conditions that cannot universally be maintained in practice [122][123]. Inevitable perturbations to device operation such as variation in the flow rate due to clogged channels [124] or fabrication-related deviations in device geometry [116] could go unnoticed and translate into process artifacts. Moreover, differences between sample viscosities could lead to different flow dynamics [124] even if the rest of the operation parameters could be made equal. Therefore, microfluidic devices for cell analysis need to be engineered to preempt those potential artifacts due to process/sample variance if they are to be deployed in the field for biomedical applications.

One strategy to ensure the microfluidic device operates under optimized conditions irrespective of unforeseen perturbations is to employ a feedback control. A feedback-controlled system automatically regulates a process variable by constantly monitoring instantaneous changes (i.e., error) and countering those by triggering a negating stimulus to maintain that process variable at a set value. Establishing a feedback control on a microfluidic therefore requires a quantitative assessment of the state of the device, a control algorithm (i.e., controller), and a control input to the system to change its state. In fact, feedback control has been successfully demonstrated in regulating microfluidic systems for a variety of applications, including digital microfluidics [209], productions of micro-droplets [210], modulations of fluidic properties [211], and automated regulations of fluid height [212], pressure [213], and temperature [214] in microfluidic chambers.

To implement feedback control with cell manipulation, we have demonstrated a system where the process variable is controlled within a feedback loop based on direct measurements on cells being manipulated within a microfluidic chip [121]. Our system utilizes (1) a network of electrical sensors (Microfluidic CODES) distributed across the microfluidic device to make measurements on flowing cells, (2) a trained deep learning algorithm to process the raw sensor data and produce actionable control signals, and (3) a controller that updates external stimuli to regulate the process variable. In a proof-of-principle demonstration, we use the deep learning-based signal processing scheme to measure cell flow speeds across the device and control a programmable pressure pump to maintain the same flow speed irrespective of perturbations. We characterize the system performance under static and dynamic perturbations and demonstrate its stability.
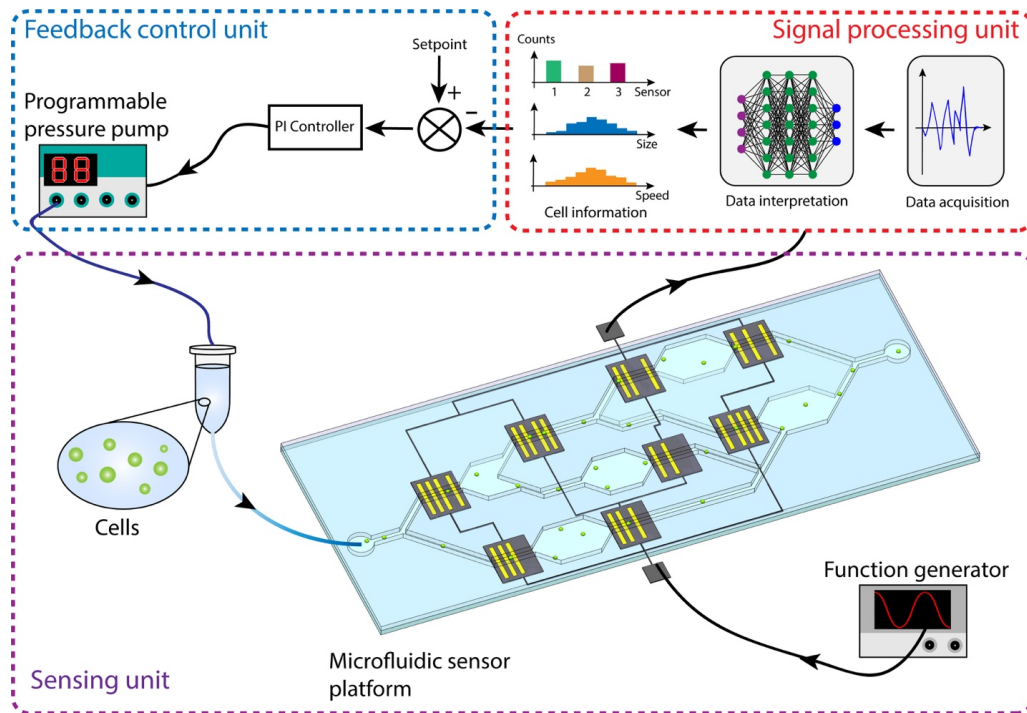
Figure 59 - Concept illustration of the Microfluidic CODES-based feedback control system. A feedback loop is constructed among a sensing unit, a signal processing unit, and a feedback control unit.

The introduced adaptive microfluidic system is composed of three main units: the sensing unit, the signal processing unit, and the feedback control unit (Figure 59).

The sensing unit is a microfluidic sensor platform consisted of surface micro-electrodes, which are designed to produce electrical signals when a cell is detected. To detect cells within the device, we utilize the fact that suspended cells modulated the electrical current as they flow over these microelectrodes. To monitor the cell flow throughout the whole device, we create a network of sensors distributed to multiple measurement nodes. Because all sensors are electrically connected, the data from the network could be acquired as a single time waveform. Nevertheless, by designing each sensor to produce a distinct waveform, we ensure a lossless recovery of information from individual sensors in the recorded electrical signal.

The signal processing unit acquires raw sensor data, analyzes its content, and calculates parameters such as size, instantaneous location, and speed for every cell. The signal processing unit could be considered as a combination of a data acquisition block and a data interpretation block. The data acquisition block consists of signal acquisition software and hardware, including amplifiers and a data acquisition board, which extracts, amplified, and transmitted sensor waveforms in real-time. Conditioned sensor waveforms are then processed by the data interpretation block. The sensor waveforms are analyzed using a deep learning model specifically to perform cell measurements in real-time. Real-time analysis of sensor data then allows timely intervention by the controller to modulate the device settings.

The feedback control unit regulates a process variable based on the measurements on cells. Measured cell parameters are compared to a predetermined target value (setpoint), and the process variable is continuously updated to minimize the difference between the two. In this work, we set our feedback loop on the cell flow speed without loss of any generality and update the driving pressure of the sample by controlling a pressure pump. A regulated flow ensures cells to flow at a determined speed inside the device irrespective of external perturbations or potential miscalibration of the pressure pump or device geometry.

4.1   Design of Sensing Unit

We designed our microfluidic sensor platform following the Microfluidic CODES using deep learning-based signal processing scheme (Figure 60). Our sensor network was composed of eight coded Coulter sensors distributed across eight 30 μm-wide microfluidic channels. Each sensor was designed to produce a unique binary sequence, specifically a randomly-generated 15-bit code sequence. The fabrication and experimental setup also followed the design of the Microfluidic CODES technology using the deep learning-based signal processing scheme.
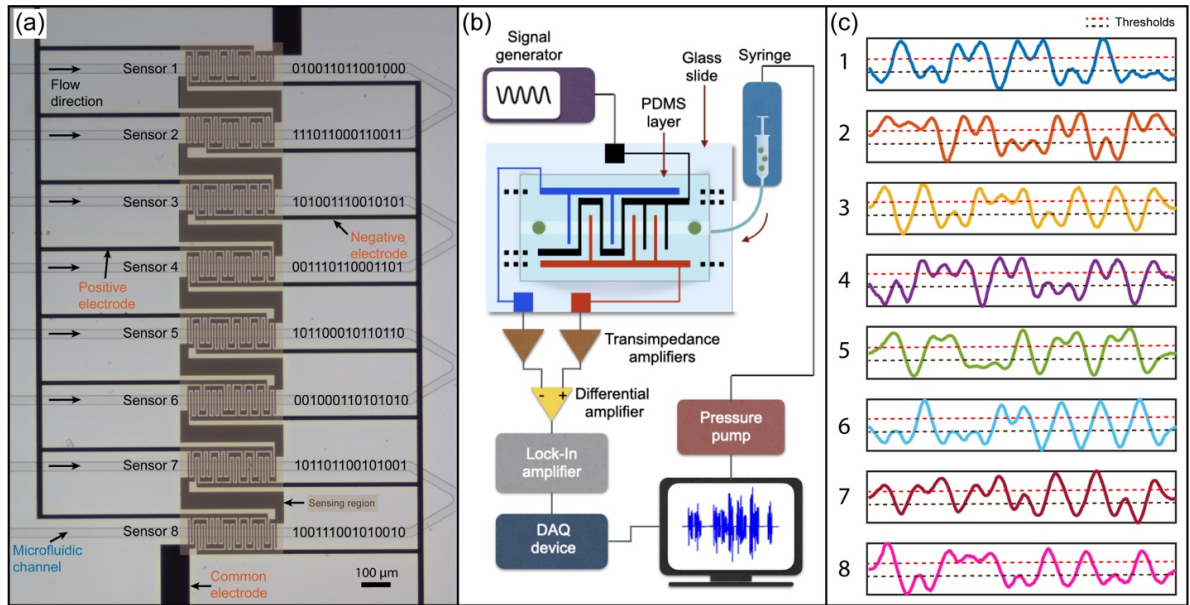
Figure 60 - Sensor design and experimental setup of the Microfluidic CODES-based feedback control system. (a) A microscopy image of the microfluidic sensor platform with eight code-multiplexed Coulter sensors. Each sensor is designed with a unique electrode pattern determined by a distinct binary code sequence. (b) A block diagram for the experimental set-up. (c) The signature waveform for each coded sensor.

4.2   Design of Signal Processing Unit

4.2.1   Real-time Signal Processing Environment

We developed a real-time signal processing environment that could continuously acquire, identify, and extract sensor waveforms corresponding to individual cell events (Figure 61a). Because cells randomly interact with sensors at different locations, the sensor waveforms asynchronously appear in the data stream (Figure 61c). To make the information available to the controller in a timely fashion, we continuously screened short blocks (50 samples) from the data stream to catch potential sensor activity. For each data block (iteration), we first calculated signal power (i.e., variance) and compared it with a predefined threshold value (variance of the baseline noise) to determine whether the signal in the current data block originated from a triggered sensor or is simply noise. If it was

114

scored as sensor data, these samples would be temporarily stored in a buffer. Next, by comparing the current data block's signal variance with that of the previous data block, we determined if the data block corresponded to either beginning or ending of a sensor waveform. If the data block was identified as an ending block, all the data blocks stored in the buffer were combined and marked as a complete sensor waveform to be identified, followed by clearing the buffer for the next sensor waveform (Figure 61b).

We implemented the continuous data acquisition in LabVIEW, and the PyDAQmx package [215] was used as a software interface between the data acquisition board and Python, a programming language commonly employed for machine learning-based data analysis. An off-line simulation of the signal extraction scheme demonstrats that sensor waveforms with varying amplitudes and durations are successfully identified from a recorded sensor data stream (Figure 61c). It should be noted that some of these extracted sensor waveforms are individual ones induced by a single cell, and some are interfering ones induced by coincident cells interacting with one or multiple sensors simultaneously. The pattern of individual sensor waveforms closely follows the binary code sequences used to encode each sensor so that they could readily be recognized, while interfering sensor waveforms require specific algorithms to demultiplex and interpret the cell information.
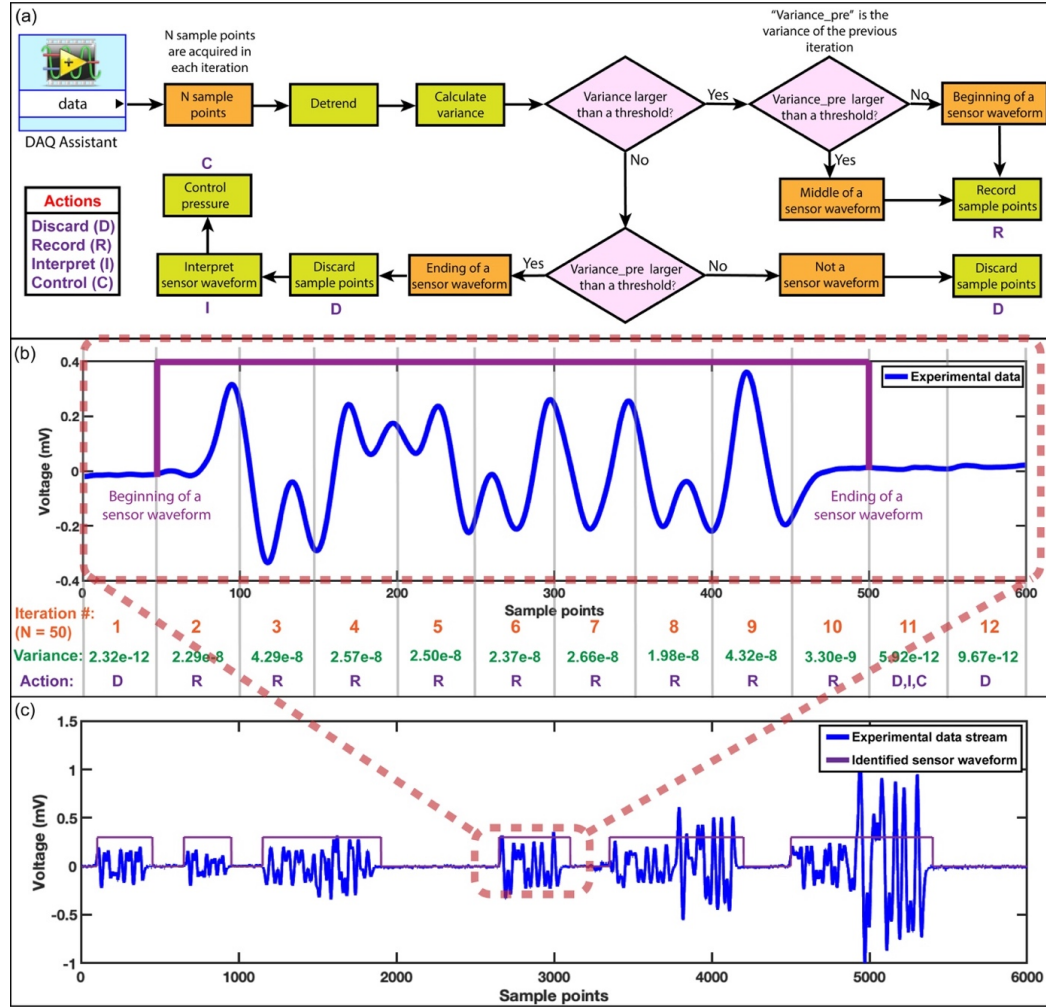
Figure 61 - Real-time sensor waveform identification of the Microfluidic CODES-based feedback control system. (a) A flow diagram illustrating the environment implemented for real-time sensor waveform identification and extraction. (b) An illustration of the process of identifying a sensor waveform. (c) Multiple sensor waveforms are successfully identified from an experimental data stream

4.2.2   *Deep Learning-based Data Interpretation*

We further improved the deep learning-based signal processing algorithm. Specifically, we still implemented a 2-stage ConvNet structure to interpret extracted sensor waveforms (Figure 62a). Given an input sensor waveform, the first stage, named region proposal network (RPN), predicts the number of signature waveforms contained in that waveform (e.g., 1 if isolated signature waveform or >1 if the sensor waveform resulted

from the interference of multiple signature waveforms) and proposes a bounding box on each individual signature waveform. Each identified signature waveform is then extracted and fed into the second stage, named sensor classification network (SCN), for a further sensor identity (location) classification. Combining the predictions from two stages, the property and behavior of detected cells are estimated. First, the number of identified signature waveforms indicates the number of detected cells. Second, the height of the bounding box represents the amplitude of the signature waveform, which, based on the Coulter principle is proportional to the size (volume) of the detected cell. Third, the width of the bounding box represents the duration of the signature waveform, which represents the time the cell spent passing through the entire sensing region of the corresponding sensor (cell residence time). This could be further used to calculate the speed of the cell. Fourth, the predicted sensor identity provides the location information of the cell as sensors are distributed at different locations on the microfluidic sensor platform. All of this information provides an on-demand snapshot of the state of cell manipulation within the microfluidic device.

In our ConvNet model, the RPN and the SCN share the same structure for feature extraction, while each has a distinct output layer (Figure 62b). Specifically, each ConvNet contains four convolutional layers, each of which is followed by a ReLU layer for a non-linear activation. After the second and fourth convolutional layers, a max-pooling layer is placed to down-sample the feature map. Two dense (fully-connected) layers are placed after the second max-pooling layer (right before the output layer). The output layer of the RPN has two groups of nodes, where the first group predicts the number of contained signature waveforms in the input sensor waveform, and the second group fits a bounding

box for each identified signature waveform. The output layer of the SCN has eight nodes, each representing one of the eight distributed Coulter sensors on the microfluidic device.
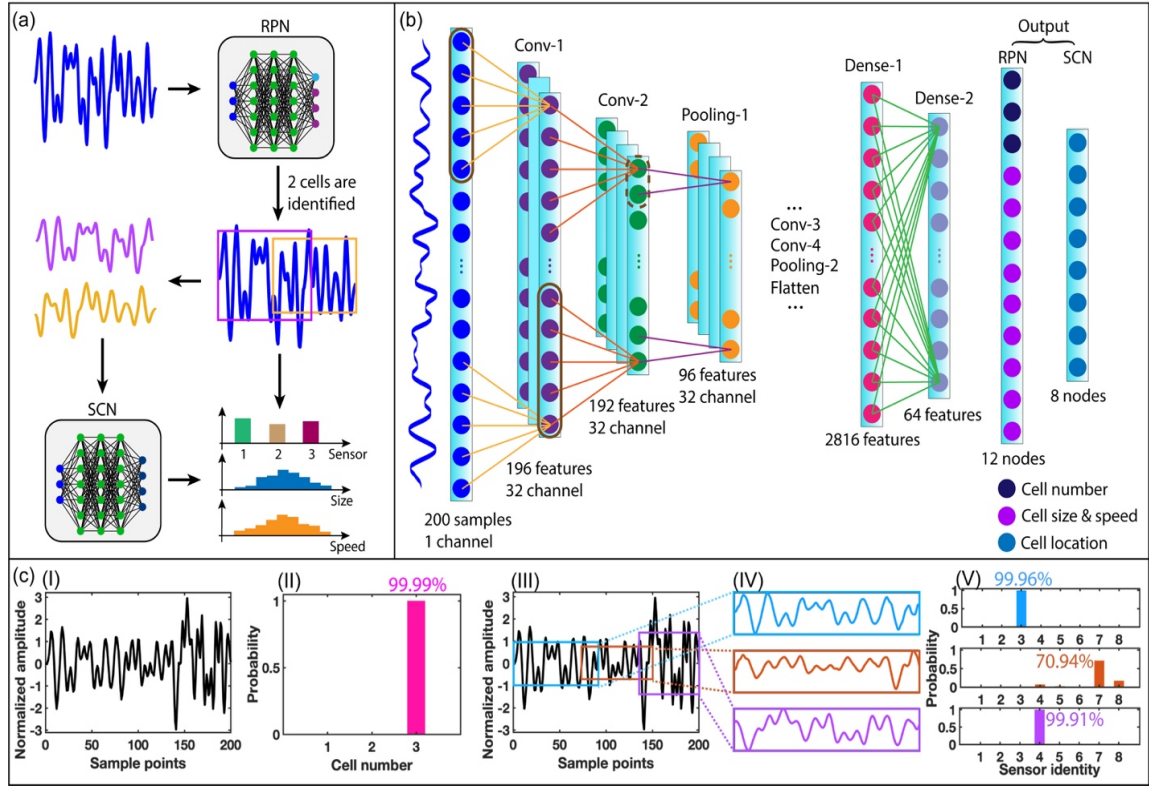
Figure 62 - Implementation of the deep learning-based sensor waveform interpretation of the Microfluidic CODES-based feedback control system. (a) A workflow showing the decoding process of the 2-stage ConvNet model. (b) The structure of the ConvNet model. (c) ConvNet decoding process for a representative 3-cell interfering sensor waveform.

We built a training dataset with 1,000,000 training waveforms. In the training dataset, each sensor has roughly the same amount of training data, and 1/3 of which are non-interfering sensor waveforms, 1/3 are 2-cell interfering sensor waveforms, and 1/3 are 3-cell interfering sensor waveforms. To increase the number of waveforms available for constructing the training dataset, we employed a data augmentation process. Briefly, each interfering training waveform is manually combined from randomly-scaled non-interfering sensor waveforms.
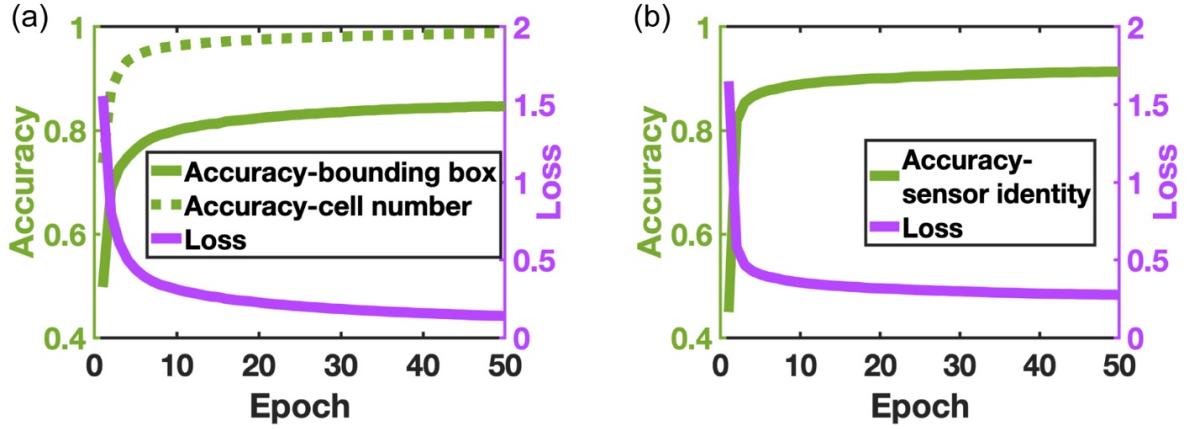
Figure 63 - Training accuracy and loss of (a) RPN and (b) SCN of the Microfluidic CODES-based feedback control system.

After training both ConvNets for 50 epochs (Figure 63), we generated a validation dataset and a test dataset to validate the ConvNets. The validation dataset is used to evaluate the performance of the ConvNets after each training epoch (Figure 64), and the test dataset is used to validate the final trained ConvNets via real-time experimental data. Similar to the training dataset, the validation dataset was manually constructed, in which all the interfering sensor waveforms were manually built from labeled but unseen non-interfering ones, of which we knew the ground truth of cell number, bounding box. and sensor identity. In this case, we also calculated the accuracy of all the predictions given sensor waveforms with different number of interfering cells (Figure 64). The test dataset was automatically recorded during an experiment, along with an optical recording. Then we used a video processing algorithm to extract cell information from the recording as the ground truth. Afterward, we compared the ConvNets-predicted distributions with optically-measured distributions in terms of cell size, speed, and sensor identity (Figure 65).

119
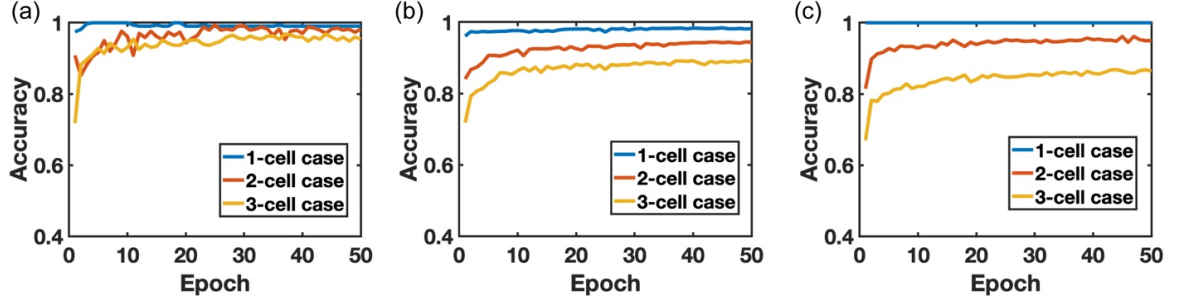
Figure 64 - Validation of the ConvNets (through the validation dataset) of the Microfluidic CODES-based feedback control system. Accuracy of (a) cell number, (b) bounding box and (c) Sensor identity are given.
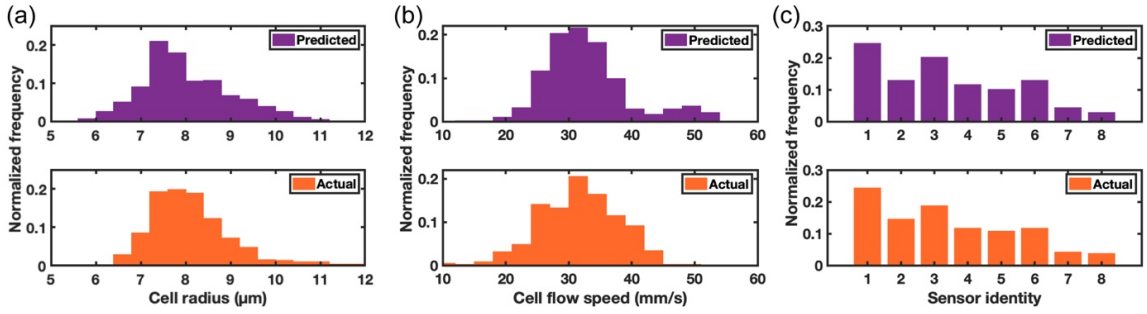
Figure 65 - Validation of the ConvNets (through the test dataset) of the Microfluidic CODES-based feedback control system. Distributions of (a) Cell size, (b) cell flow speed, and (c) Sensor identity are given.

The decoding process of a 3-cell interfering sensor waveform from the validation dataset is demonstrated (Figure 62c). Given the input sensor waveform (Figure 62c, I), the RPN predicts the number of signature waveforms (cells) producing the observed signal with a confidence level (Figure 62c, II) and marks individual signature waveforms making up the signal with bounding boxes (Figure 62c, III). Once the signature waveforms within the bounding boxes are extracted and normalized (Figure 62c, IV), the SCN makes a sensor identity prediction on each identified signature waveform and reports the confidence level for each prediction (Figure 62c, V).
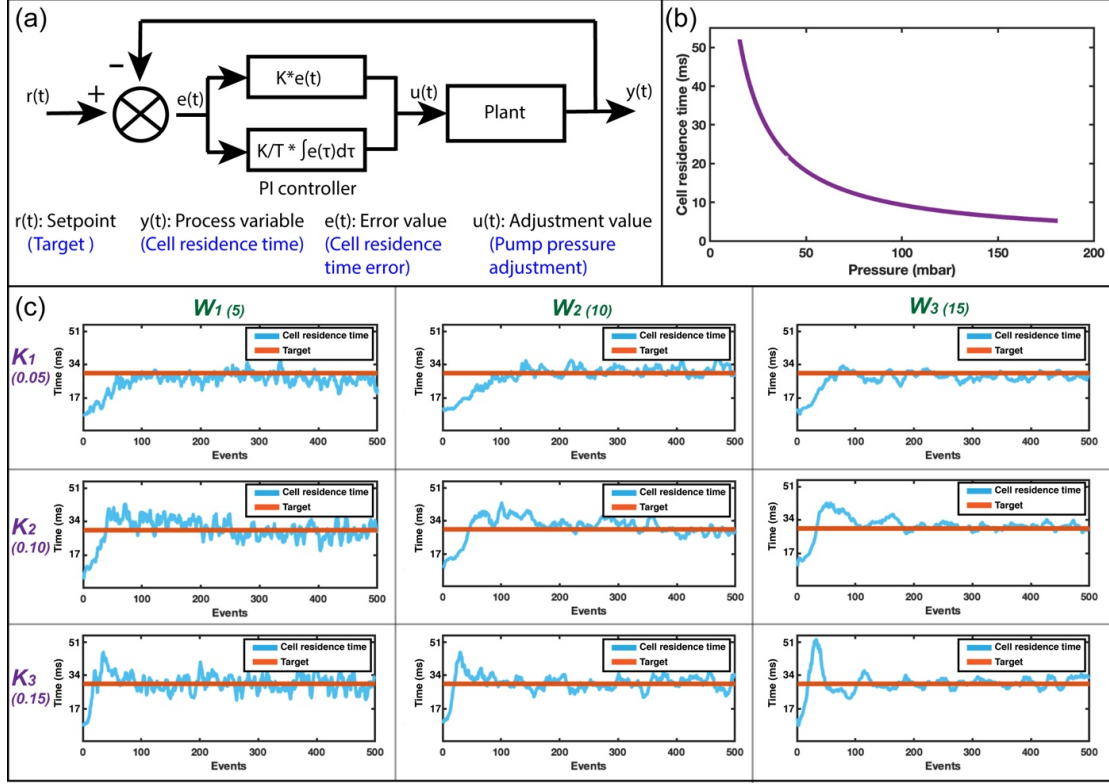
Figure 66 - Design and characterization of the Microfluidic CODES-based feedback control system. (a) A block diagram showing the proportional-integral (PI) controller in the microfluidic feedback control system. (b)The monotonic relation between the pump pressure and the cell residence time. (c) Step response of the feedback control system given different combinations of feedback gain (K) and averaging window size (W).

4.3   Design of Feedback Control Unit

4.3.1   Design of the Feedback Control System

To demonstrate closed-loop control of cell manipulation in the microfluidic device, we developed a feedback control system that regulated cell flow speed based on measurements on processed cells. Besides the fact that cell flow speed is of practical importance for a variety of cell manipulation/sorting applications in microfluidic devices, it has a simple dependence on the driving pressure, making it an ideal parameter for proof-of-concept demonstration of closed-loop control. The designed feedback control system

121

could be abstracted into a plant and a feedback controller (Figure 66a). The plant consists of the programmable pressure pump, the sensing unit, and the signal processing unit producing a measured process variable, $y(t)$, which is the variable to be controlled in the system. The goal of the feedback control system is to regulate the control input (the pump pressure), so that the process variable could approach the setpoint, $r(t)$, as the target value of the process variable. This is achieved by the system continuously calculating an error value, $e(t)$, as a difference between the instantaneous process variable and the setpoint and the feedback controller attempting to minimize the error by generating an appropriate adjustment value, $u(t)$, to update the control input in the plant.

The core part of our feedback control system is the feedback controller, which determines the parameters adjusting the control input given a specific error value. For our study, we implemented a proportional-integral (PI) controller, which adjusted the control input based on a weighted sum of present and past error values [216]. As such, the adjustment value to the pressure pump is computed by

$$u(t) = Ke(t) + \frac{K}{T_i} \int_0^{T_i} e(\tau)d\tau$$

where K is the feedback gain, and T_i is the integration period.

To regulate the cell flow speed in a feedback control loop, we chose the measured time that a cell interacted with a sensor (cell residence time) as the process variable. The cell residence time was calculated as the quotient of the sensor size and the cell flow speed, which has a linear relationship with the driving pressure (Figure 67). Therefore, the cell residence time has a non-linear but monotonic relation with the driving pressure and hence

122

could be adjusted by updating the pressure pump settings (Figure 66b). Each time a cell (i.e., event) is detected, our system measures the cell residence time, compares it with the setpoint, and calculates an error value, based on which, the PI controller produces an updated setting for the programmable pressure pump.
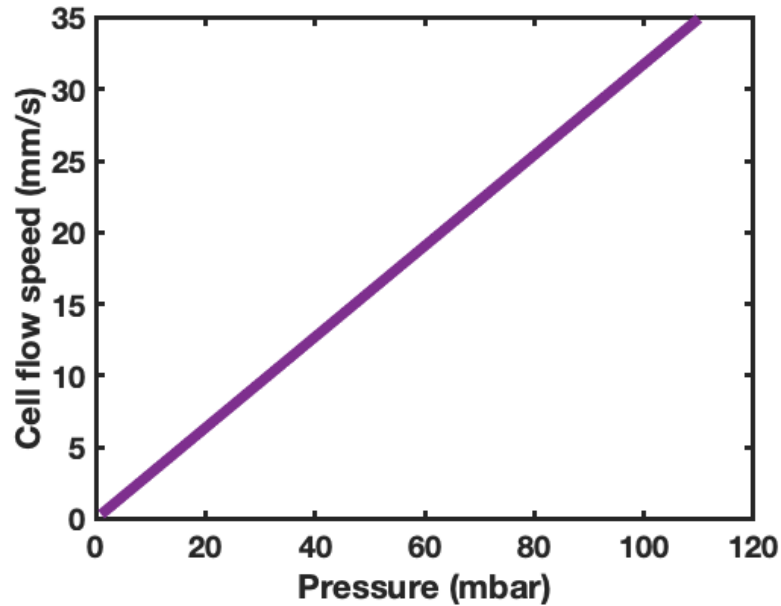
Figure 67 - The calibration between the driving pressure and the cell flow speed in the Microfluidic CODES-based feedback control system.

4.3.2   Step Response of the Feedback Control System

To characterize our feedback control system, we processed a model biological sample with a density of 5 x 10^5 cells ml^{-1}. We first measured the step response of the system. In these measurements, we set the setpoint for cell residence time at 10 ms, corresponding to a pressure of 95 mbar. Then we abruptly changed the setpoint from 10 ms to 30 ms and monitor changes in the process variable as it converged to the new setpoint (Figure 66c). We analyzed the effects of the feedback gain (K) and the averaging window size (W), which set the number of earlier cell measurements considered when calculating

the instantaneous cell residence time. Specifically, we selected K from a list of [0.05, 0.10, 0.15] and W from a list of [5, 10, 15]. For each parameter combination, we evaluated the step response against multiple metrics: First, we measured the rise time, defined as the number of events required for the cell residence time to rise from 10% to 90% of the setpoint, indicating how fast the system responds to a change in the setpoint. Second, we measured the settling time from the number of events required for the cell residence time to enter and stay within a certain error band (15%) around the setpoint, indicating how fast the system converges. Note that because our measurements are only updated when a cell is detected by the sensor network, we chose our unit of progress as the cell detection events rather than the actual time commonly used in these analyses. Finally, we analyzed the response in its overshoot from how much the cell residence time exceeds the new setpoint before convergence, representing the maximum swing of the control system.

Analysis of step responses from different feedback controllers clearly shows the effect of varying feedback parameters. Increasing the feedback gain results in a faster response due to a higher sensitivity to the error value but also leads to larger swings and a less stable system. With a higher K, the rise time decreases, the overshoot increases, and the settling time increases (Table 4), an expected response from a PI controller [216]. Varying the W, on the other hand, acts as a noise filter for cell residence time measurements. Because cell flow speed within a microfluidic device has an intrinsic variance due to Poiseuille flow profile [217] within channels or non-uniform hydraulic resistance across the device, averaging measurements over multiple cells reduces noise in calculated error values. This results in a smoother response but increased the time to convergence.

124

Table 4 - The effect of the feedback gain (K) on the rise time, overshoot, and settling time of the system for W = 15 in the Microfluidic CODES-based feedback control system.

K	Rise time (events)	Overshoot (ms)	Settling time (events)
0.05	55	3.4	73
0.10	31	13.3	171
0.15	18	23.1	188

4.3.3   Tracking of Dynamic Setpoints

Next, we tested our system's ability to follow a varying setpoint for the process variable. A dynamic setpoint for a process variable could be helpful in practice for applications where sweeping operational settings of a microfluidic device could enable a parametric analysis on a sample. In characterizing our system for dynamic setpoints, we chose a *K* of 0.1 and a *W* of 5 to build the feedback controller. We programed the setpoint to vary with a controlled pattern and monitor how well the instantaneous cell residence time in the microfluidic device followed the programmed function (Figure 68). We first ramped the cell residence time from 10 ms to 30 ms and found that the system was able to track the setpoint successfully (Figure 68a). Next, we modulated the setpoint sinusoidally, and the system was able to respond with a small but noticeable delay (Figure 68b). Finally, we modulated the setpoint in the form of a square wave. While we clearly observed the feedback delay and ringing on both rising and falling edges, the system recovered in between and was able to track the setpoint successfully (Figure 68c).
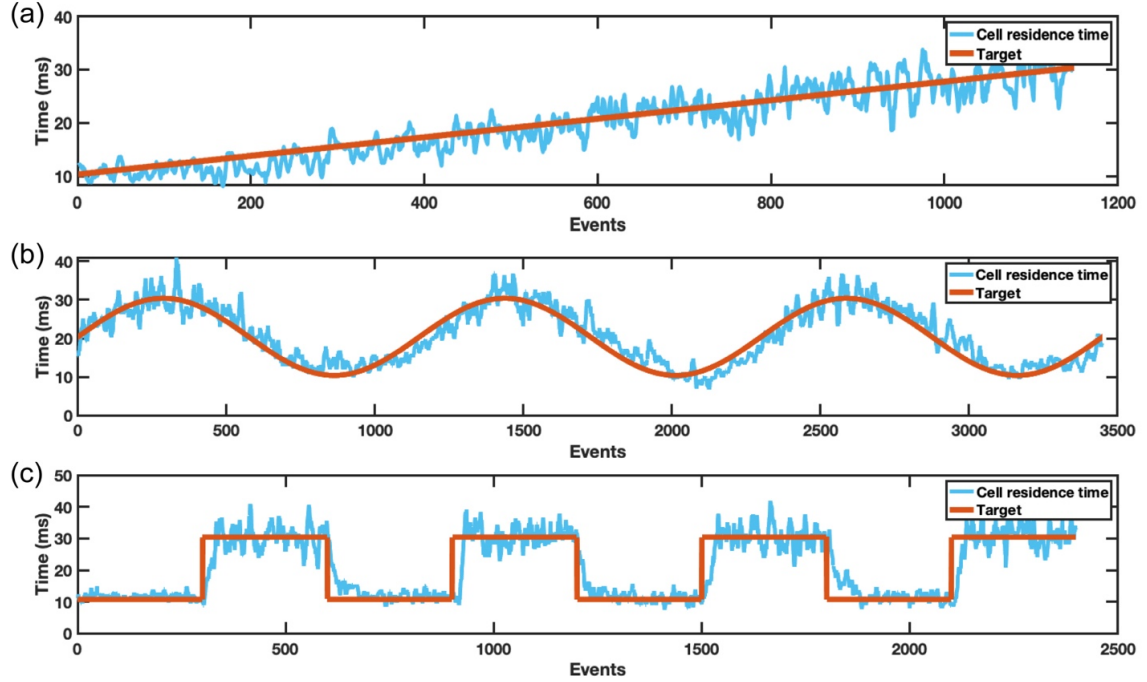
Figure 68 - Tracking dynamic setpoints to characterize the Microfluidic CODES-based feedback control system in terms of (a) ramp, (b) sine, and (c) square wave. In each case, the cell residence time closed tracks the dynamic setpoint, demonstrating the high accuracy and fast converging speed of the feedback control system.

4.3.4 Feedback Control under Perturbation

To investigate the feedback response under external perturbations, we added another pressure pump (perturbing pump) to the system and monitored the response of the perturbed system. The perturbing pump was connected to the outlet of the microfluidic device to perturb cell flow speed by countering the driving pressure pump connected to the inlet, and the feedback system was engaged to keep the cells flowing at the same speed irrespective of the external perturbation by adjusting the driving pressure. Initially, the net forward pressure was set at 100 mbar with a 200-mbar driving pressure and a 100-mbar perturbing pressure and this condition produces a ~9-ms cell residence time. We also set the parameters as $K = 0.1$ and $W = 10$ for the feedback controller. Later, we modified the perturbing pressure in 50 mbar steps between 0-200 mbar (Figure 69a, I, IV). Despite such

126

a perturbation, the measured instantaneous cell residence time remained at 9 ms, which is the setpoint for our feedback controller (Figure 69a, II, V). Transient ringing in the measured cell residence time coincides with the changes in the perturbation signal as anticipated and is quenched after a few events. The asymmetric ringing of the instantaneous cell residence time at the rising and falling edges of the perturbing pressure is expected due to the non-linear dependence between the cell residence time and the driving pressure (Figure 66b). Finally, comparing the feedback-controlled driving pressure with the perturbing pressure shows that the driving pressure is adjusted to balance the perturbing pressure changes (Figure 69a, III, VI), maintaining a constant forward pressure. It should be noted that all the automatic adjustments to the driving pressure pump are made based on the aggregate cell residence time data collected from the network of distributed electrical sensors (Figure 69b) without prior knowledge on the perturbation. Taken together, these results show the ability of the feedback system to successfully adapt to the changing perturbation.

Table 5 - Optically measured cell flow speeds (µm/s) at nine different time periods during the perturbation experiment closely match the expected cell flow speed (35.12 µm/s) in the Microfluidic CODES-based feedback control system.

Time period	1	2	3	4	5	6	7	8	9
Cell flow speed (µm/s)	34.50	34.05	33.15	33.60	32.26	35.84	35.84	36.29	35.39
Accuracy (%)	98.2	97.0	94.4	95.7	91.9	97.9	97.9	96.7	99.2

To independently validate the effectiveness of the feedback control in maintaining the cell flow speed within the microfluidic device, we directly measured the flow speed of

cells with high-speed microscopy while the device was under perturbation. Cells were randomly sampled for imaging throughout the experiments, and the measurements were compared against the setpoint flow speed (obtained by converting the target cell residence time) (Table 5). The microscopically-measured cell flow speed (n=10) at different time periods (Figure 69a, I) is found to have an average <3.5% deviation from the setpoint flow speed of 35.12 $\mu m/s$ with a 1.39 $\mu m/s$ standard deviation among the measured cell flow speeds. These results prove the ability of the developed feedback-controlled system to maintain a process variable based on direct measurements on cell state under a continuous perturbation.
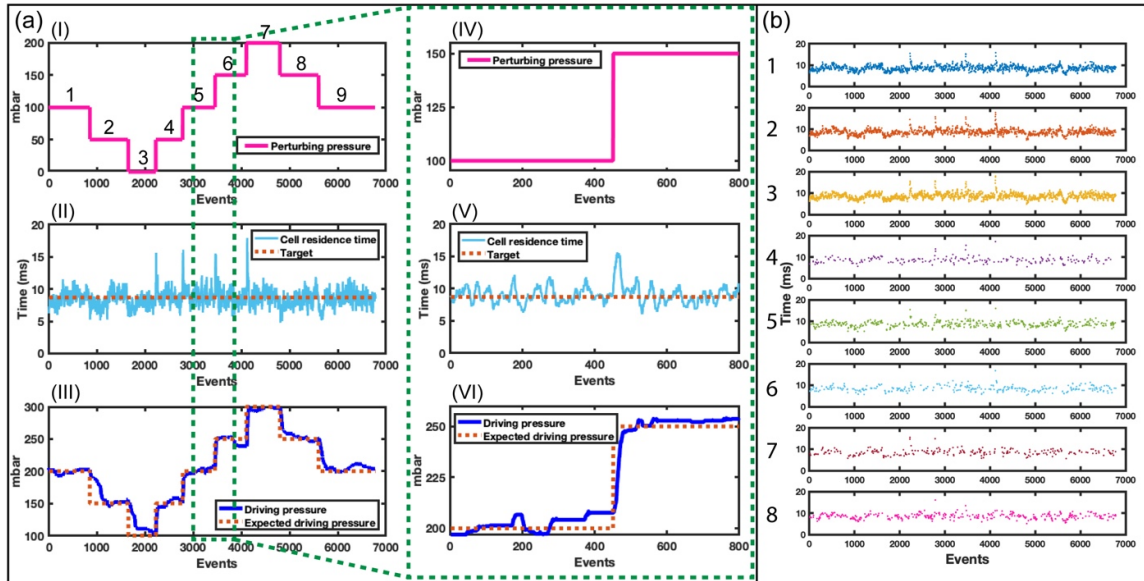
Figure 69 - Adding continuous external perturbations to characterize the Microfluidic CODES-based feedback control system. (a) System performance under continuous perturbations. (b) Cell residence time in terms of different locations (sensor identities). Cells at different locations are regulated to have the same cell residence time.

We further observed the performance of the system under different perturbing pressures (Figure 70). Initially, the driving pressure was set to 300 mbar, and the perturbing pressure was set to 0 mbar. Then we changed the perturbing pressure with five different

values (50, 100, 150, 200, 250 mbar) and observed the performance of the system. We characterized the system regarding two parameters: (1) the maximum deviation represents the maximum distance (ms) between the instantaneous cell residence time and the setpoint (Figure 70a); (2) the recovery time (events) represents the number of events required for the instantaneous cell residence time to recover to and be stable around the setpoint (Figure 70b). With perturbing pressures ranging from 50 to 250 mbar, the system could successfully recover to the setpoint with increasing maximum deviation and recovery time.
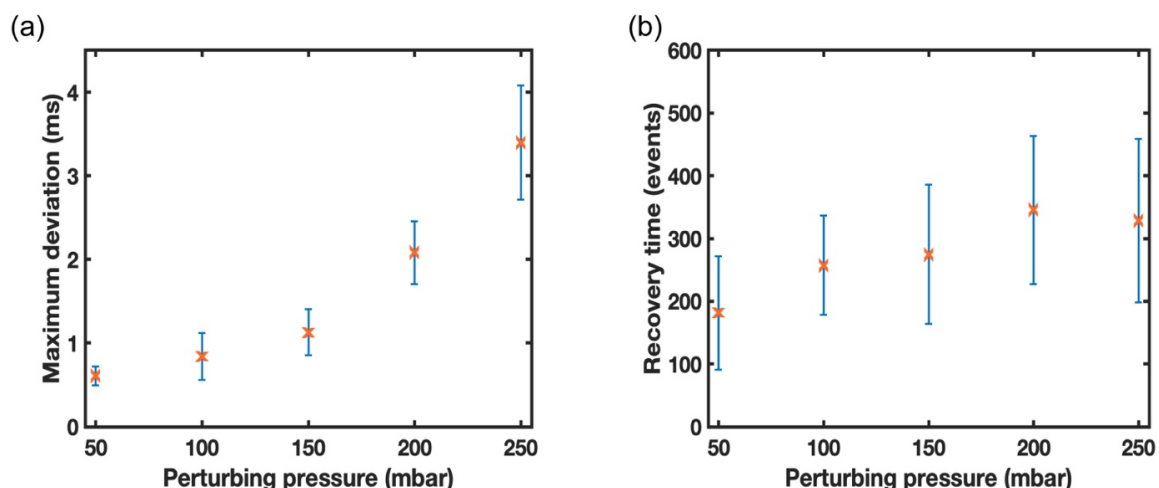
Figure 70 - Adding different external perturbations to characterize the Microfluidic CODES-based feedback control system. (a) The maximum deviation of the cell residence time (ms) away from the setpoint. (b) The number of events required for the cell residence time to recover to and be stable around the setpoint after the perturbation.

4.4   Discussion

We demonstrate a microfluidic system in which the spatiotemporal state of each manipulated cell is continuously monitored with a built-in electrical sensor network, not only as a means for quantitative analysis but also to control and adapt the device operation

based on these measurements on the sample under test. Importantly, monitoring of cells within the microfluidic device through electrical signals from the sensor network does not have the redundancy of imaging and hence requires less computational resources, which enables us to implement real-time closed-loop control on process variables. Finally, the fact that measurements for closed-loop control could be performed solely using sensors within the microfluidic device eliminates the need for external instruments such as a microscope or high-speed cameras and demonstrates the feasibility of creating adaptive lab-on-a-chip devices that could be operated outside of research laboratories.

Existing feedback-controlled microfluidic systems either utilize isolated sensors that directly measure a process variable such as pH, temperature, or impedance or utilize arrays of discrete sensors with dedicated readouts for spatial information. In contrast, we could set our feedback loop on multi-dimensional spatiotemporal data from cells within the device while still acting on a one-dimensional electrical waveform. This aspect makes our approach advantageous for implementing adaptive yet low-cost microfluidic cell-based assays. Additionally, we could extract, through computation, cell information including size, speed, and location, any combination of which could be further used as the process variable of the feedback system. When combined with differential manipulation of cells, such spatiotemporal data can be linked to cell biochemical/biophysical properties, further expanding the choice of process variables for the feedback loop.

In terms of electrically tracking cells over the microfluidic device, our deep learning-based demultiplexing scheme offers several advantages over traditional demultiplexing techniques used in code division multiple access (CDMA) telecommunication networks. Traditional approaches employed for demultiplexing coded

electrical signals rely on the correlation of the signal with a set of template waveforms to identify specific patterns. While computationally inexpensive, correlation-based demultiplexing requires a special code-set with individual codes being mutually orthogonal with each other, effectively constraining the design of sensors in the network. In contrast, deep learning-based analysis of the output signal allowed us to identify differentiating features between individual sensor waveforms irrespective of the degree of correlation between them and utilize these differences to rapidly decode the output signal. Besides increased flexibility in design, the ability to train the ConvNets with actual waveforms from sensors rather than relying on model-based templates of ideal square waveforms increases the sensitivity of deep learning-based demultiplexing. It should also be noted that, even though the deep learning model introduced in this work was designed to interpret waveforms from coincidental detection of up to 3 cells, waveforms due to more coincident cells could be resolved, albeit with less accuracy, by modifying the training dataset and the structure of the ConvNets.

The ability to continuously and quantitatively assess the manipulation of cells or other particles in a microfluidic device in real-time through built-in sensors and to change the state of the device in response presents exciting opportunities. While this work demonstrates the regulation of cell flow speed under perturbation as proof of principle, the cell spatiotemporal data generated by networked sensors contain a wealth of information about the sample under test and could be fully utilized to command a variety of actuators internally or externally. From the operational point of view, the applications could range from controlling valves to redirect flows based on the instantaneous distribution of cells on the device to the detection of clogged channels or malfunctioning devices. Furthermore,

microfluidic systems coupled with different types of stimuli ranging from chemicals to physical transducers could either be automatically tuned to achieve a desired sample response or alternatively be employed to perform automated experiments by sweeping different parameters in a closed-loop setting to extract multi-parametric information from the sample under test.

CHAPTER 5.   MICROFLUIDIC CODES-BASED CELL CHARACTERIZATIONS

Microfluidic CODES not only provides a quantitative electronic output to plastic lab-on-a-chip devices while retaining their simplicity and frugality, but also transforms the Coulter sensing from a technique that is limited to sizing and counting of cells to a technology that analyzes cells with respect to any parameter that can be used to differentially manipulate cells on a microfluidic device such as mechanical properties [125], immunophenotype [126][127], and cell surface expression [129][130].

5.1   Cell Mechanophenotyping

Interrogating the mechanical properties of cells and microorganisms reveals a multitude of insights into their state. Hence, such measurements have been used to obtain stem cell differentiation stage [218], disease progression in blood-related pathologies such as sickle cell disease [219] and provide insight into the metastatic propensity of tumor cells [220]. Furthermore, being a label-free biomarker, the cell mechanical phenotype affords ease of use and flexibility in instrumentation.

Recent advances in microfluidic technologies have enabled researchers to characterize cell stiffness by measuring the time that it takes to traverse a photolithographically defined constrictive microfluidic channel [221]. A fundamental limitation to this approach is the low throughput due to the time spent by the cells as each of them undergoes compression to enter the constrictive channel. Furthermore, during the time a cell is passing through a constriction, that channel is idle and cannot accept another cell. To overcome the throughput limit, we developed a microfluidic device with parallel

constriction channels, each of which is monitored by multiplexed electrical sensors positioned at the entrance and exit of each constriction (Figure 71).
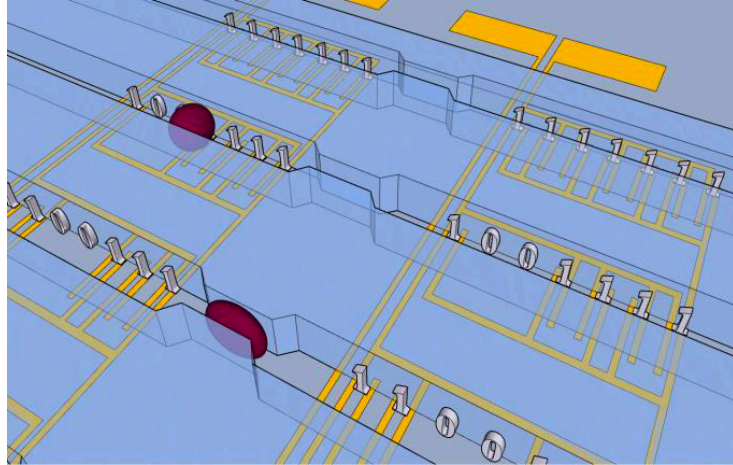
Figure 71 - Concept illustration for Microfluidic CODES-based cell mechanophenotyping. Sensor network are patterned at the entry and exit of a constriction channel to record the information of cells entering and exiting the constriction channel.

5.1.1   System Design

Our goal is to create a device that can measure cell stiffness via the constrictive channel without having to suffer a throughput penalty. To this end, we have made two fundamental design choices. The first is the use of parallel channels, which allows simultaneous measurements of multiple cells. All the channels feature a constrictive zone (5 μm wide by 50 μm long) and two electrical sensors, each one placed before and after the constriction. These sensors log the constriction entry and exit time of every cell processed. The second design choice is that of the electrical sensors themselves, which are code-multiplexed based on the introduced Microfluidic CODES scheme.

As we have introduced, the electrical sensors are a series of coplanar electrode pairs that use the Coulter principle to detect the cells. The excitation signal is applied to the common electrode, and the sink is the sensing electrode that is patterned adjacent to the common electrode. By arranging these electrode pairs in particular sequences, we are able to create sensors that produce signature bipolar signals unique to each channel.
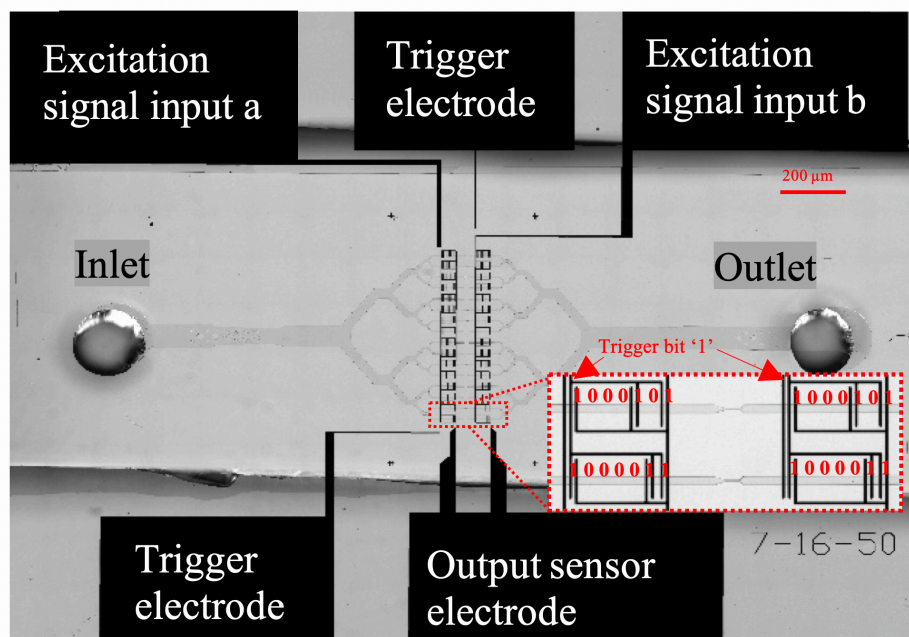
Figure 72 - Microscope image of the device for Microfluidic CODES-based cell mechanophenotyping.

Here we demonstrate a proof-of-principle device consisting of 16 parallel channels, each featuring a constriction zone, integrated with a sensor network (Figure 72). Each constriction employs two electrical sensors (entry and exit) that log the entry and exit time for the cell. The electrical detection technique is based on the error-correction based-Microfluidic CODES scheme, which enables the assignment of a unique identifier to each channel. Each sensor is a unique sequence of 7 binary bits, where a '1' bit and '0' bit is represented by the presence and absence of an electrode pair, respectively. These electrodes

135

maintain an AC electric field between them (500 kHz, 200 mV$_{pp}$). When a cell flows over the electrode pairs in the sensor, a sequence of pulses, which can be uniquely linked to a particular constriction, is generated. In some versions of this technology, an additional 'trigger' bit is also patterned at the beginning of every sensor to aid in signal processing. It should be noted that device based on correlation-based processing was also introduced.
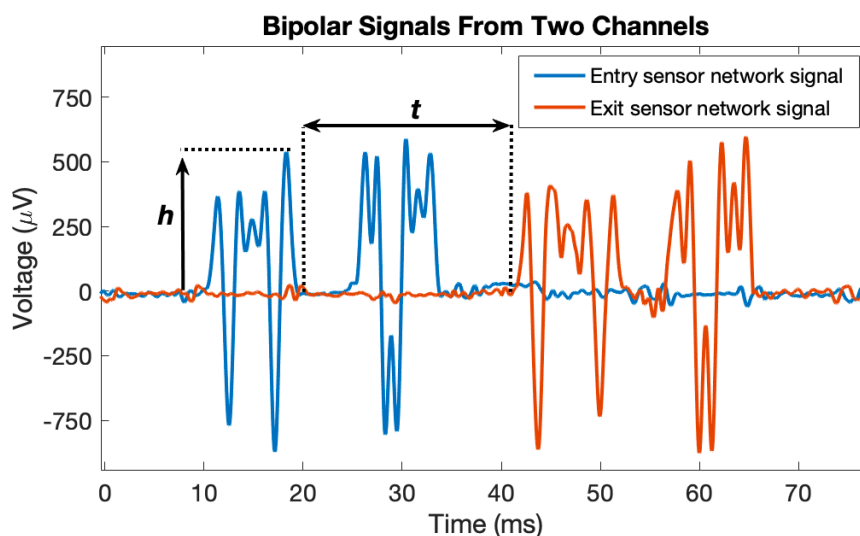
Figure 73 - Sensor signals for Microfluidic CODES-based cell mechanophenotyping. For each cell, the entry sensor network signal is paired with the exit sensor network signal, so that we can get the cell information before and after the constriction channel.

5.1.2   Sensor Signal Processing

We also demonstrate the signals from the device using correlation-based Microfluidic CODES. Each of the two outputs produced by the device, namely the entry sensor network detections and the exit sensor network detections, are cumulative output currents of the individual sensors within the network (Figure 73). While this architecture simplifies the hardware and affords scalability, it necessitates advanced signal processing.

Specifically, if two or more sensors within a network register cell detections at the same time, the signals interfere and get distorted. We refer to these distorted signals as interfering cases, and recovered the signals using the successive interference cancellation. With the program, the timestamps of the identified codes, for both interfering and non-interfering cases, are aggregated and transit times are calculated by measuring the duration between each code in the entry data stream and its complement in the exit data stream.
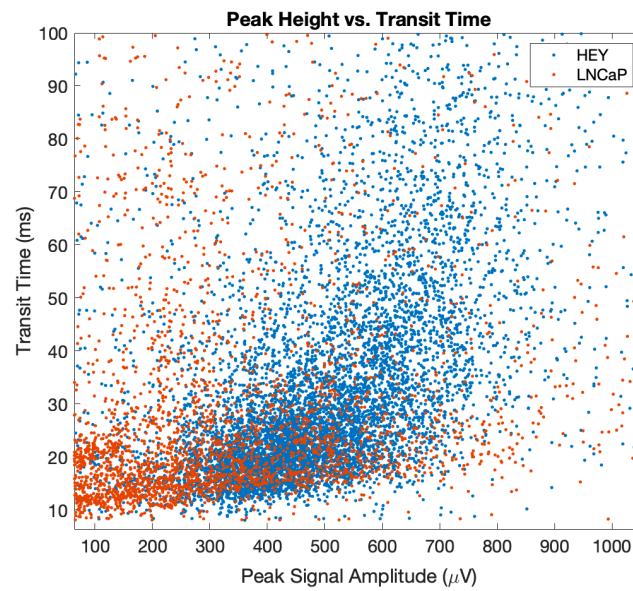
Figure 74 - Scatter plot showing peak signal amplitude vs. transit time for two cell lines measured using the Microfluidic CODES-based cell mechanophenotyping.

5.1.3   Preliminary Results

Two human cancer cell lines, namely HeyA8 (human ovarian carcinoma) and LNCaP (human prostate carcinoma), that are known to possess similar size but differing stiffnesses [222], were separately processed to demonstrate our device's mechanophenotyping capabilities.

We measured the size of each cell from the peak amplitude of the corresponding sensor signal based on the Coulter principle. By plotting the transit time against the peak signal amplitude for each processed cell (Figure 74), we could observe the effect of cell size on the constriction transit time. The data show a clear trend that for both cell lines, the cells which take longer to traverse the constriction produced larger peak signal amplitudes.
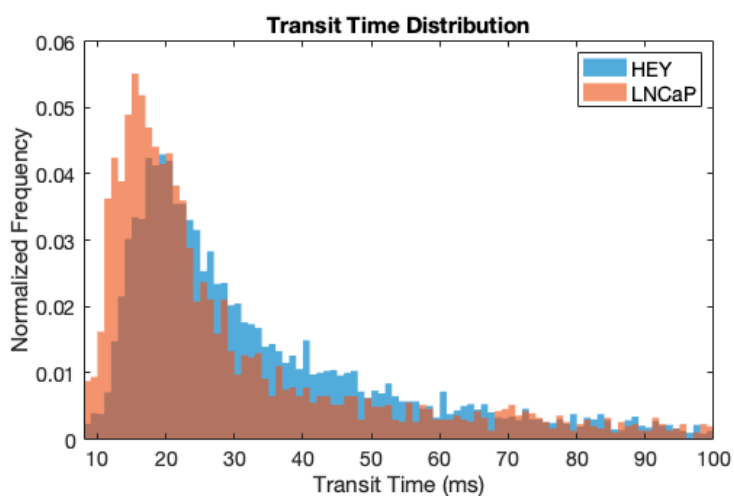
Figure 75 - Distribution of the transit times taken by two cell lines to clear the constrictions measured using the Microfluidic CODES-based cell mechanophenotyping.

In addition to the cell size, the transit time is also affected by cell stiffness in our measurements. When comparing the transit time distributions of both cell lines (Figure 75), we observed that HeyA8 cells, on average, took longer to clear the constrictions compared to LNCaP cells. To decouple the effect of cell size on the transit time measurements, we grouped the transit time data based on cell size. Direct comparison of transit time for similarly sized HEY and LNCaP cells shows that HeyA8 cells consistently take longer to pass through the constriction and hence the HeyA8 cells are found to be stiffer than the LNCaP cells.

5.2 Cell Immunophenotyping

Immunophenotyping (i.e., identifying the membrane protein expression, usually CD antigens, of cells) is widely used to characterize cells in lineages of differentiation from hematopoietic stem cell, and also to diagnose and classify diseases derived from those cells. This process typically requires flow cytometers or fluorescence microscopy, which are typically housed in centralized laboratories. While microfluidic devices have been used as immunophenotyping assays through immunoaffinity-based capture of the target cells, these devices either require external tools for readout [223] or are limited to a single antigen type [110]. Here, we present a method for combinatorial immunophenotyping of cells against multiple antibodies in a microfluidic system, that readily provides quantitative results as an electrical signal. Our approach is based on the integration of multiple cell capture chambers, each selectively functionalized with a specific antibody, with Microfluidic CODES.

5.2.1 System Design

We designed and fabricated a proof-of-concept device with a 2×2 capture chamber array, each functionalized by a specific antibody (Figure 76). The microfluidic chambers were arranged as two parallel tracks, with each track consisting of two serially connected chambers. In each chamber, micropillars were used to increase the cell capture efficiency. Code-multiplexed electrical sensors encoded with distinct digital codes were placed at strategic locations across the device to quantify the capture rate in each chamber through differential counts. All of the sensor data was collected from a single waveform, which is computationally analyzed to obtain immunophenotyping results. Our device was fully

139

integrated yet frugal, consisting of a polydimethylsiloxane (PDMS) microfluidic channel layer fabricated using a soft lithography process, and an electrode-patterned glass substrate fabricated with a lift-off process.
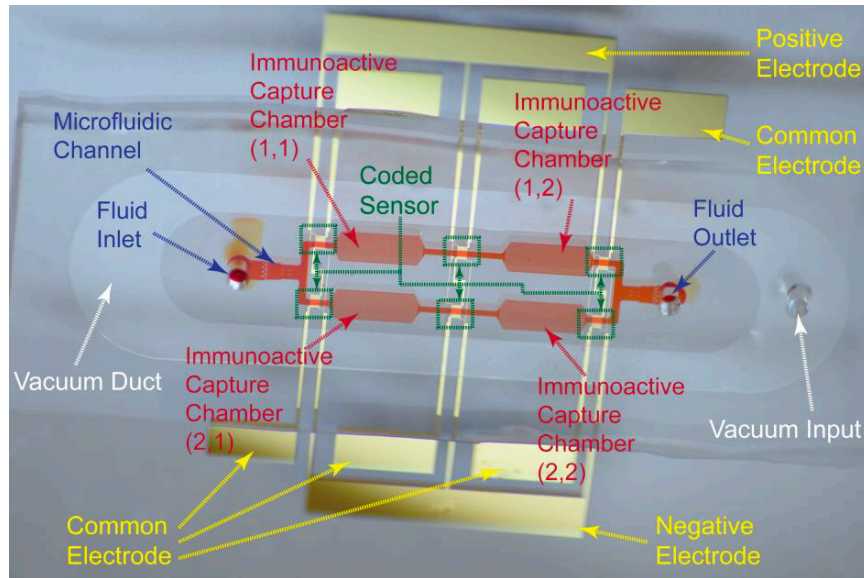
Figure 76 - Microscope image of the device for Microfluidic CODES-based cell immunophenotyping.

To functionalize our device, we developed a new technique to selectively modify individual capture chambers (Figure 77). Briefly, prior to bonding, the PDMS layer was first treated with (3-Mercaptopropyl)-trimethoxysilane solution droplets for 1 hour, followed by incubation with N-y-maleimidobutyryloxy-succinimide-ester (GMBS) for 30 minutes and NeutrAvidin solution for 1 hour. After washing and gentle drying, the PDMS layer was aligned and reversibly attached to an auxiliary PDMS layer consisting of microscale features that isolated individual chambers by sealing the fluidic channels in between. The auxiliary component also had pre-punched holes above the chambers and allowed different biotinylated antibody solutions to be introduced and selectively incubated in different chambers for 1 hour. Finally, the PDMS layer was sealed with the glass

substrate using vacuum and primed with bovine serum albumin to block non-specific cell adhesion.
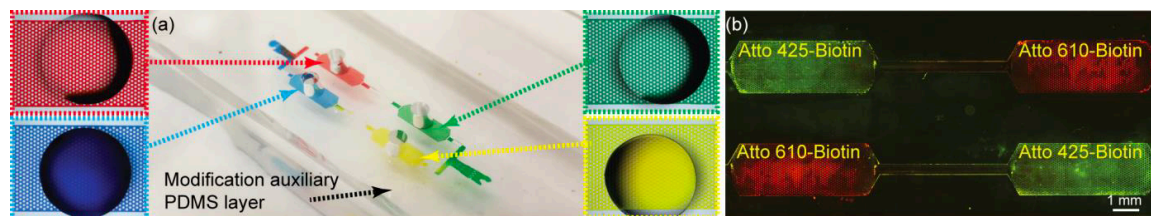
Figure 77 - Functionalization of the microfluidic capture chambers the device for Microfluidic CODES-based cell immunophenotyping. (a) Chamber structure. (b) Functioning result.

5.2.2   Sensor Signal Processing

We used the SIC for processing the sensor signal and acquired cell information.

5.2.3   Preliminary Results

We tested the device with human blood sample following the lysis of red blood cells. The chambers of the device were pre-treated with four different antibodies (anti-CD66b, anti-CD15, anti-CD38, and anti-CD45 antibodies), and the sample was driven through the device using a syringe pump. A 500 kHz sine wave was applied to drive the sensor network, and signals from the sensors were measured using a lock-in amplifier.

By acquiring all the sensor network data from a single electrical waveform, the number of cells passing through each sensor was obtained from the digital processing of the recorded signal on a computer (Code 1,1: 2541, Code 1,2: 1015, Code 1,3: 574, Code 2,1: 576, Code 2,2: 356, Code 2,3: 305). Based on the processed sensor data, the fraction of each immunophenotype (Chamber 1,1 (CD66b+): 60.0%, Chamber 1,2 (CD66b-CD15+): 17.4%, Chamber 2,1 (CD38+): 38.2%, Chamber 2,2 (CD38-CD45+): 8.85%) is

calculated. The number of captured cells in each chamber was also confirmed using microscopy (Figure 78), and the fraction of each subpopulation closely agrees with results from a commercial flow cytometer (Abbott, CELL-DYN Ruby).
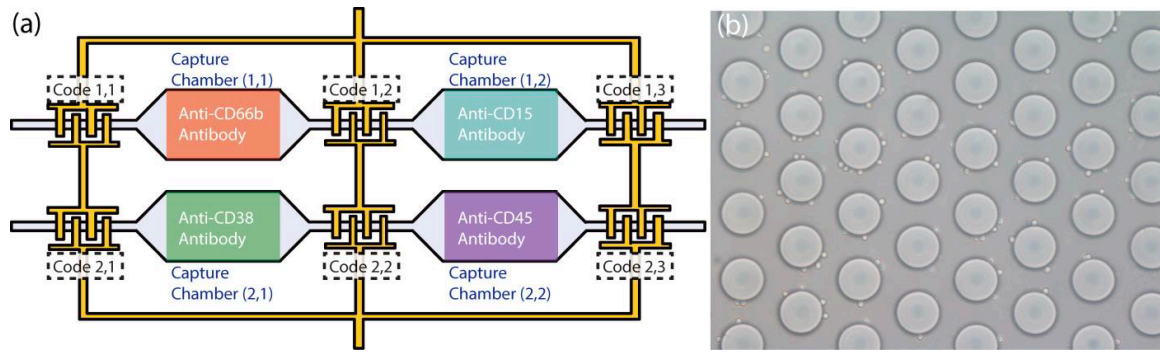
Figure 78 - Experimental setup of the microfluidic capture chambers the device for Microfluidic CODES-based cell immunophenotyping. (a) Concept illustration of the working principle. (b) Image showing the capture result.

5.3   Cell Membrane Antigen Expression Profiling

Membrane antigens dictate biochemical interactions of a cell with its environment and are often used as diagnostic and therapeutic biomarkers for clinical applications. As such, identification of cell membrane antigens and quantification of their expression at the single-cell level is of great interest for applications ranging from drug discovery to medical diagnostics. Fluorescence-based flow cytometry is the current gold standard for quantitative surface expression analysis, but it involves highly complex, expensive and bulky instrumentation limiting its use to laboratories with skilled technicians. Therefore, devices that can achieve similar functionality in a low-cost portable platform could potentially impact biomedical testing in resource-limited settings.

Due to its simplicity and specificity, magnetophoresis is commonly used in bulk and microfluidic cell separation to enrich a cell subpopulation of interest in a heterogeneous mixture [224]. As part of this process, target cells are labeled with magnetic beads that are functionalized with antibodies specific to their membrane antigens. Immunomagnetically labeled cells are then differentially displaced under an external magnetic field based on their specific magnetic load. While magnetophoresis is typically employed for binary separations (i.e., magnetically labeled cells from unlabeled cells), separation of cells into multiple subpopulations based on their magnetic loads has also been demonstrated [225].

In this work, we introduce a microfluidic system that uniquely couples magnetophoretic cell sorting with an array of code-multiplexed resistive pulse sensors to electrically quantify the spatial mapping of cells in the sorting process. Because magnetic load (i.e., the number of the beads on the cell) is correlated with the cell's surface expression, we can use our sensor data to profile surface antigen expression in a cell population directly from an electrical signal.

5.3.1 System Design

Our device (Figure 79) consisted of three stages. In the first stage, cells, magnetically-labelled against a specific antigen, are hydrodynamically focused into a single flow stream using a sheath flow. In the second stage, cells deflected into one of the eight outlets based on their magnetic loads under a transverse magnetic field generated by the permanent magnet embedded in the device. In the final stage, cells flowing through each outlet channel were detected and counted by the code-multiplexed electrical sensor. All sections combined, the device offers both separation of cell subpopulations and an

integrated quantification capability, and therefore can be considered as a low-cost, all-electronic alternative to a fluorescent activated cell sorter.
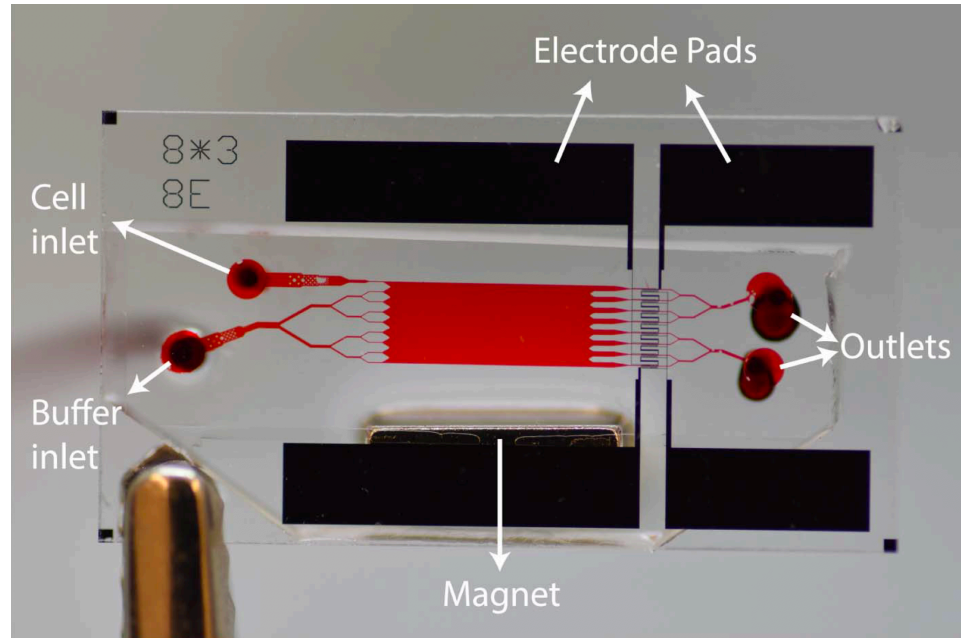
Figure 79 - Microscope image of the device for Microfluidic CODES-based cell membrane antigen expression profiling.

The microfluidic device features a 30 μm-wide inlet channel for the cell population and a buffer solution inlet that bifurcates into eight 30 μm-wide channels. The magnetophoretic deflection chamber is 8 mm long and 3 mm wide. A permanent magnet, placed 1.5 mm away from the edge of the deflection chamber, generates the external magnetic field required to deflect magnetically labeled cells. At the outlet, the flow is divided into eight 30 μm-wide outlet channels. On the floor of each outlet channel, coded sensors consisting of 5 μm-wide electrodes are placed to quantify magnetically sorted cell subpopulations.

The electrode sensor network at the device outlet is designed based on the Microfluidic CODES technology that we introduced. Briefly, the sensor in each outlet

channel was formed by distinctly patterned surface electrodes that produce distinguishable signal patterns when a cell flows over them (Figure 80). In this work, each sensor was specifically designed to generate a 31-bit digital code (Gold code) signal that is orthogonal to the signals produced by sensors monitoring other outlets. This multiplexed sensor network architecture provides two advantages: First, it allows us to effectively label magnetically deflected cells in the electrical output waveform with signature codes that can be associated with the specific outlet channel that the cell is sorted into. Second, it enables simultaneous monitoring of all outlet channels from a single electrical output, significantly simplifying the hardware. Importantly, recovery of interfering sensor signals is ensured due to the orthogonality of sensor signals from different outlets. Taken together, our sensor system enables electronic quantification of fractionated cell subpopulations.
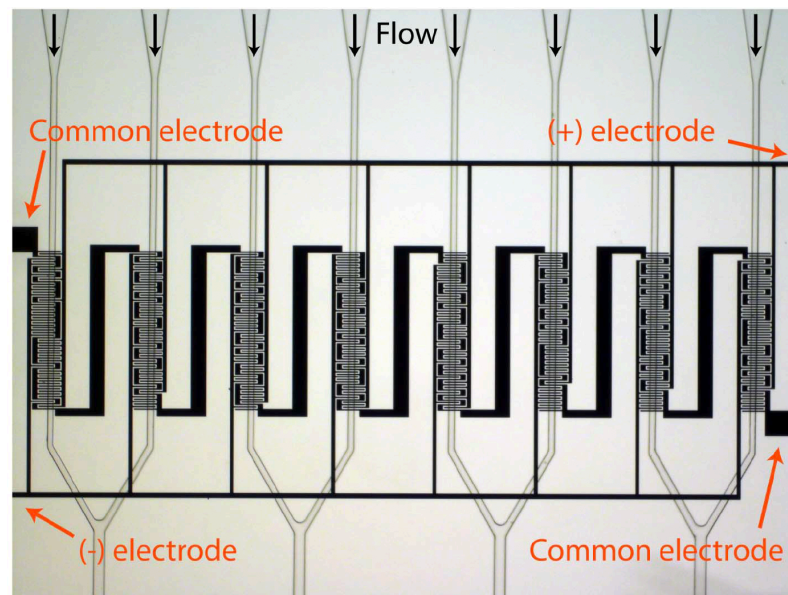
Figure 80 - Microscope image of the sensor network for Microfluidic CODES-based cell membrane antigen expression profiling.

5.3.2   Sensor Signal Processing

We use the SIC for processing the sensor signal and acquired cell information.
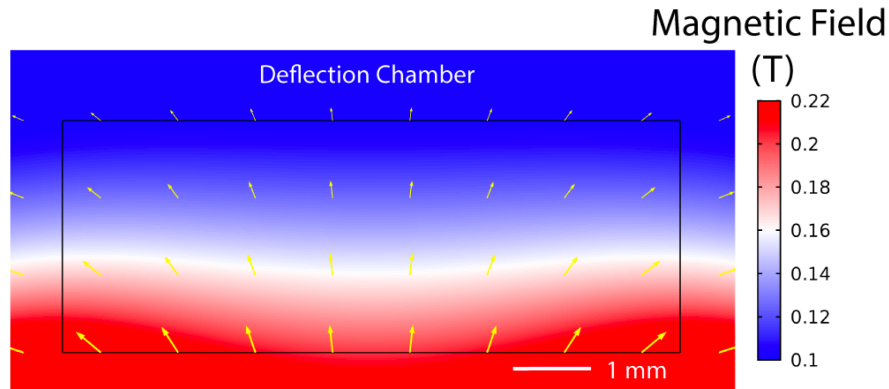
Figure 81 - Simulation of the magnetic field magnitude and proportional gradient with the deflection chamber of the device for Microfluidic CODES-based cell membrane antigen expression profiling.

5.3.3   Preliminary Results

We first simulated the magnetic field distribution within the magnetophoretic deflection chamber using finite element analysis (Figure 81). For a 1.5 mm distance between the magnet and the edge of the magnetophoretic deflection chamber, our simulations indicate that the magnetic field magnitude changes from 0.2 T to 0.1 T over a distance of 3 mm in the transverse direction. The simulation results enable us to calculate magnetic forces and the transit time (i.e., flow rate) required for a cell labeled with a given number of magnetic beads to deflect into a specific outlet channel.

To experimentally demonstrate the effect of sample flow rate on the magnetic deflection in our device, we analyzed the trajectory of magnetic beads as a function of the inlet pressure. 1 µm magnetic beads are injected from the cell inlet into a device that has 4 mm long and 1.7 mm wide deflection chamber. The trajectory of magnetic beads under different drive pressures was obtained from the stationary beads at the base of the channel

due to sedimentation (Figure 82). Driven with 120 mbar inlet pressure, the magnetic beads left the chamber from the 3rd (from the top) outlet. When the driving pressure was reduced to 50 mbar, the beads deflected more, and arrived at the 4th and 5th outlets. Further decreasing the pressure to 30 mbar resulted in beads leaving the system from the 6th outlet.
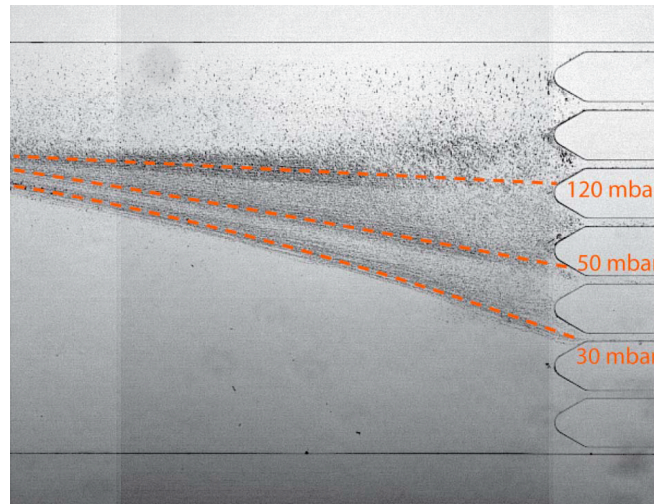
Figure 82 - Sedimentation pattern showing the deflection trajectory of the 1 μm magnetic beads in the deflection chamber of the device for Microfluidic CODES-based cell membrane antigen expression profiling.

We tested our system by processing breast cancer cell line (MDA-MB-231) population suspended in 1X PBS solution. Magnetically-labelled cells were pneumatically driven through our microfluidic device at 50 mbar using a computer-controlled pressure regulator. 1X PBS solution was driven from the buffer inlet under the same pressure to create the sheath flow. To electrically detect the cells, the common electrode of the sensor array was excited by a 500 kHz sine wave, and the electrical current signals were acquired from two (positive and negative) sensing electrodes and extracted by amplifiers.

A total of 821 cells were analyzed in our experiment. The distribution of cells in different outlets was presented as a histogram showing fraction of cells deflected into each

outlet channel (Figure 83). For qualitative comparison, we also analyzed a cell population

from the same batch using flow cytometry to validate the result.
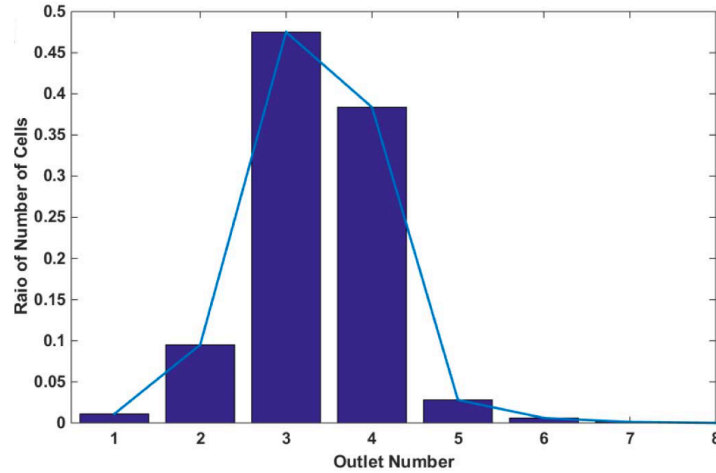
Figure 83 - Histogram showing the fraction of MDA-MB-231 cells defected into different outlet channels of the device for Microfluidic CODES-based cell membrane antigen expression profiling.

5.4   Discussion

Combining with the Microfluidic CODES technology, we have introduced a

fundamentally different flow cytometry approach that is more amenable to hardware

integration and cost reduction than its conventional counterpart. Our approach allowed the

whole flow cytometer to be realized as a disposable microfluidic platform that can directly

be interfaced electronically. Specifically, our integrated flow cytometer is composed of

two stages, a cell-discriminating stage, and a sensing stage. In the cell-discriminating stage,

target cells were spatially manipulated based on certain properties, so that the sensing stage,

equipped with the microfluidic CODES sensing technology, electrically detected target

cells. Combining the functionalities from both stages, target cells can be characterized.

Currently, we have introduced integrated flow cytometry for the characterization of cell mechanical properties, immunophenotype, and cell surface expression. We believe our cytometry technique addresses several issues that currently limit the point-of-care adoption of conventional fluorescence-based flow cytometry by offering a chip-based, electronic alternative that is especially well suited for mobile and resource-limited scenarios.

The cell-discriminating stage utilizes the exciting opportunity offered by lab-on-a-chip devices to deterministically screen a large number of cells. In the cell-discriminating stage, a type of force, such as mechanical, electrical, magnetic, or chemical force, can be engineered to fractionate cell suspensions with high-throughput based on the contrast in their properties such as size, shape, elasticity, and electrical properties. In this sense, the cell-discriminating stage can be seen as an upstream sample preparation stage. which maps cells to different locations on the chip according to properties under investigation, prior to analytical measurements.

Even though we mainly focused on measuring a certain property of a cell (discriminating cells based on a specific property), the cell-discriminating stage can be designed to incorporate multiple substages so that multiple cell properties can be used as a discriminator at the same time. In this case, under the multi-dimensional measurement, more complex cell differentiation can be achieved. For example, by concatenating a DLD stage, an inertial focusing stage, and a magnetophoresis stage, CTCs can be extracted from whole blood [54]. Concatenating multiple substages of cell differentiation increases the capability of the cell-discriminating stage so that the whole microfluidic platform can be used in more versatile situations for healthcare purposes.

The sensing stage utilizes the Microfluidic CODES technology for a distributed Coulter detection of differentiated cells in the previous stage so that cell spatial information can be transduced into cell property information. Three factors need to be addressed when designing the sensing stage. First, the number of code-multiplexed sensors can be increased to enhance the resolution and capacity of the measurement. However, when the number of sensors increases, the sensing area is also inevitably enlarged (also due to the potential increase of code length when more sensors are integrated), resulting in more interference among code-multiplexed Coulter sensors. More inference further decreases the signal SNR and increases the error rate. Therefore, the tradeoff between the sensor capacity and the signal processing accuracy needs to be addressed. The second factor, which is also correlated with the first one, is that the sample concentration needs to be adjusted accordingly. As the expected number of coincident cells is related to the sensing area and sample concentration, when the sensor dimension (number of sensors, length of code, width of electrodes) is fixed, the sample concentration should be adjusted to achieve a target error rate. That is to say, when the sample is whole blood, a dilution process might be needed before the measuring process. Third, when integrating more sensors, the design and physical implementation of the scaled sensor network should also prioritize minimization of the electrode trace resistance to ensure a uniform response from the sensors in the network.

Currently, the sensing stage mainly acts as a downstream result collector and analyzer, and there's no communication from the sensing stage back to the cell-discriminating stage. This setup is straightforward but requires human intervention in the cell-discriminating stage to ensure a proper cell differentiating performance. For example,

in a cell sorting chamber, the cell flow rate needs to be manually determined so that target cells can be properly isolated. On the other hand, a further step forward of this technology is to build a feedback connection from the sensing stage back to the cell-discriminating stage, in which case, the cell discriminating stage could use the current result (measured by the sensing stage) to adjust itself so that an optimal condition can be reached. Constructing a feedback loop between these two stages will enable a fully-automated and integrated flow cytometry. More details will be illustrated in the next chapter.

Our technology can be easily fully-integrated. To activate code-multiplexed sensors in the sensing stage, a function generator is required to provide the excitation signal and to further extract sensor waveforms, a lock-in amplifier is required to do the demodulation. Currently, we are still using an external function generator and lock-in amplifier, which is not ideal for point-of-care purposes. On the other hand, we can integrate microfluidic chambers and required external hardware within a PCB so that the entire microfluidic platform can be a standalone device. Compared with traditional flow cytometry, which has the drawback of high cost, operational complexity, and bulky instrumentation, our technology has a great potential to be adopted in resource-poor settings, being useful to detect and monitor prevalent infectious diseases.

CHAPTER 6. CONCLUSIONS AND OUTLOOK

6.1 Innovations

A multitude of integrated Counter sensors can be distributed across a microfluidic platform to provide spatiotemporal information from processed/manipulated cells. Such information provides Coulter counters with the ability to analyze cell populations by monitoring cells' responses to various stimuli on the device besides their conventional use for sizing and counting cells. These responses can be further used to characterize cell properties. On the other hand, accessing information from all Coulter sensors in a scalable manner requires reliable demultiplexing strategies so that individual sensor data can be recovered with minimal loss.

To solve this problem, we develop the Microfluidic CODES, which is a multiplexed sensing technology that can be incorporated within a microfluid device for a spatial-temporal analysis of particles. In a Microfluidic CODES sensor platform, we spread a single Coulter counter across a whole microfluidic device by micropatterning its electrodes to create multiple measurement nodes, and location-specific Coulter signatures could be realized with distinct electrode patterns at each node. Based on different demultiplexing schemes, we have introduced three versions of this technology, namely the Correlation-based, the error-correction-based, and the deep learning-based one. Each version has its own characteristic and is validated with a high-speed camera.

Combining the Microfluidic CODES with a cell manipulation chamber, we have developed fully-electronic cutometers for characterizations of cell properties, such as mechanical property, immunophenotype, and cell surface expression.

Moreover, in the aforementioned Microfluidic CODES-based cytometers, it will be more interesting if monitored cell information can be further used to automatically enhance cell manipulation performance through feedback control. We therefore introduce a Microfluidic CODES-based feedback control system. As proof of principle, we use this feedback system to regulate the cell residence time in a microfluidic device. Specifically, we first build a real-time signal processing environment, in which a ConvNet based model is trained to interpret sensor waveforms with high speed and accuracy. Then, a PI controller is used to process the interpreted result and constantly generate an adjustment signal to update a programmable pressure pump. The control system performs well on constant target and dynamic target, and converges fast given an external perturbation, demonstrating that the presented approach can readily be employed for various kinds of microfluidic cell manipulation applications.

6.2   Future Work

6.2.1   Future work on the Deep Learning Model

We have already obtained promising results using ConvNets to process interfering Coulter sensor signals. Currently, the model has two stages, the RPN and the SCN. The two-stage structure is easy to build, but these two stages need to be trained separately, and also decrease the signal processing speed. Combining these two stages into an end-to-end model will be a big forward to the model.

Currently, the model is designed to interpret waveforms with a maximum of four coincident cells. This is enough in most situations. However, when the sample density is very high, two problems might occur. First, interfering waveforms with more cells will be detected. Currently, to increase the maximum number of coincident cells that can be solved, we need to modify the output layer of the ConvNet and retrain the model. We could come up with a better strategy to increase the efficiency. The second problem is there is a trade-off between the accuracy and the complexity of the ConvNet model. If we want to reliably solve sensor waveforms with more coincident cells, we probably need to increase the number of parameters in the model, which will decrease the signal processing speed. We could find an equilibrium in this trade-off.

Another problem is how to ensure real-time processing given an extremely high-density sample. When the signal processing speed cannot follow the data acquisition speed, the hardware will overflow and report errors. We could add some internal function to keep the hardware working (like dropping new samples) before overflow happens.

6.2.2 *Future work on the Feedback-Enhanced Integrated Cytometers*

We have demonstrated the combination of the Microfluidic CODES sensor platform with a microfluidic cell manipulation chamber for cell characterizations. On the other hand, these cell manipulation chambers are typically designed to function under optimized conditions. For example, we need to manually set the pressure pump that drives the cell samples to ensure a good cell manipulation result.

To develop a fully-automated integrated cytometer, we could add the Microfluidic CODES-based feedback mechanism with a cell manipulation chamber, so that the system

could automatically adjust and work in an optimal condition. For example, in a fully-automated electronic microfluidic cytometer for the profiling of cell membrane antigen expression, magnetically sorted cells are directed into discrete outlets with a programmable pressure pump, and the outlets are concurrently monitored by a Microfluidic CODES sensor network to quantify cell fractions. Based on the current fraction, the system automatically updates the pressure pump through a feedback loop, so that the sample flow rate can be adjusted accordingly in real-time, which, in turn, enhances and optimize the dynamic range of the system (Figure 84).
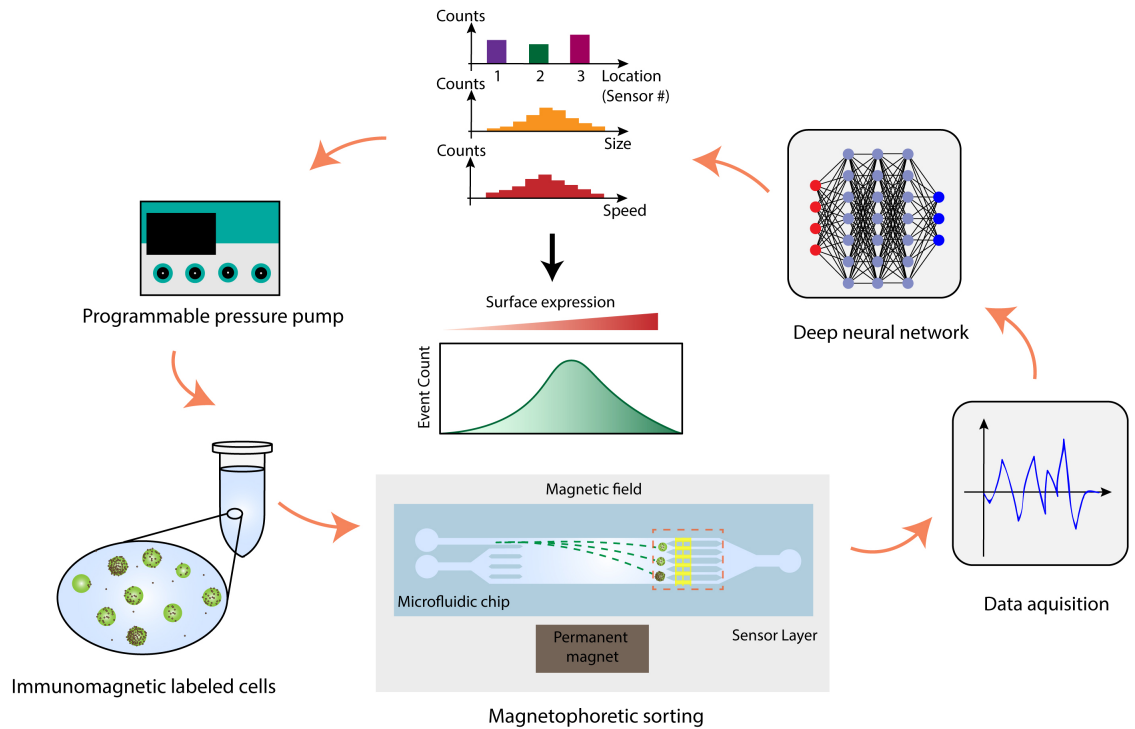
Figure 84 - Concept illustration of a fully-automated integrated cytometer for a profiling of cell membrane antigen expression.

REFERENCES

[1]   Yetisen, A. K., Akram, M. S., & Lowe, C. R. (2013). based microfluidic point-of-care diagnostic devices. *Lab on a Chip*, *13*(12), 2210-2251.

[2]   Geng, T., Bao, N., Sriranganathanw, N., Li, L., & Lu, C. (2012). Genomic DNA extraction from cells by electroporation on an integrated microfluidic platform. *Analytical chemistry*, *84*(21), 9632-9639.

[3]   Morsink, M. A. J., Willemen, N. G., Leijten, J., Bansal, R., & Shin, S. R. (2020). Immune Organs and Immune Cells on a Chip: An Overview of Biomedical Applications. *Micromachines*, *11*(9), 849.

[4]   Ohno, K., Tachikawa, K., & Manz, A. (2008). Microfluidics: applications for analytical purposes in chemistry and biochemistry. *Electrophoresis*, *29*(22), 4443-4453.

[5]   Glawdel, T., Almutairi, Z., Wang, S., & Ren, C. (2009). Photobleaching absorbed Rhodamine B to improve temperature measurements in PDMS microchannels. *Lab on a Chip*, *9*(1), 171-174.

[6]   Sarioglu, A. F., Aceto, N., Kojic, N., Donaldson, M. C., Zeinali, M., Hamza, B., ... & Toner, M. (2015). A microfluidic device for label-free, physical capture of circulating tumor cell clusters. *Nature methods*, *12*(7), 685-691.

[7]   Shields IV, C. W., Reyes, C. D., & López, G. P. (2015). Microfluidic cell sorting: a review of the advances in the separation of cells from debulking to rare cell isolation. *Lab on a Chip*, *15*(5), 1230-1249.

[8]   Bagnall, J. S., Byun, S., Begum, S., Miyamoto, D. T., Hecht, V. C., Maheswaran, S., ... & Manalis, S. R. (2015). Deformability of tumor cells versus blood cells. *Scientific reports*, *5*(1), 1-11.

[9]   Di Carlo, D., D., Irimia, D., Tompkins, R. G., & Toner, M. (2007). Continuous inertial focusing, ordering, and separation of particles in microchannels. *Proceedings of the National Academy of Sciences*, *104*(48), 18892-18897.

[10]   Xiang, N., Wang, J., Li, Q., Han, Y., Huang, D., & Ni, Z. (2019). Precise size-based cell separation via the coupling of inertial microfluidics and deterministic lateral displacement. *Analytical chemistry*, *91*(15), 10328-10334.

[11]   Yamada, M., Nakashima, M., & Seki, M. (2004). Pinched flow fractionation: continuous size separation of particles utilizing a laminar flow profile in a pinched microchannel. *Analytical chemistry*, *76*(18), 5465-5471.

[12]   Cupelli, C., Borchardt, T., Steiner, T., Paust, N., Zengerle, R., & Santer, M. (2013). Leukocyte enrichment based on a modified pinched flow fractionation approach. *Microfluidics and nanofluidics*, *14*(3-4), 551-563.

[13]   Sollier, E., Rostaing, H., Pouteau, P., Fouillet, Y., & Achard, J. L. (2009). Passive microfluidic devices for plasma extraction from whole human blood. *Sensors and Actuators B: Chemical*, *141*(2), 617-624.

[14]   Warkiani, M. E., Guan, G., Luan, K. B., Lee, W. C., Bhagat, A. A. S., Chaudhuri, P. K., ... & Han, J. (2014). Slanted spiral microfluidics for the ultra-fast, label-free isolation of circulating tumor cells. *Lab on a Chip*, *14*(1), 128-137.

[15]   Jimenez, M., Miller, B., & Bridle, H. L. (2017). Efficient separation of small microparticles at high flowrates using spiral channels: Application to waterborne pathogens. *Chemical Engineering Science*, *157*, 247-254.

[16]   Baba, A. I., & Câtoi, C. (2007). *Comparative oncology*. Bucharest: Publishing House of the Romanian Academy.

[17]   Beech, J. P., Holm, S. H., Adolfsson, K., & Tegenfeldt, J. O. (2012). Sorting cells by size, shape and deformability. *Lab on a Chip*, *12*(6), 1048-1051.

[18]   Ranjan, S., Zeming, K. K., Jureen, R., Fisher, D., & Zhang, Y. (2014). DLD pillar shape design for efficient separation of spherical and non-spherical bioparticles. *Lab on a Chip*, *14*(21), 4250-4262.

[19]   Holm, S. H., Beech, J. P., Barrett, M. P., & Tegenfeldt, J. O. (2011). Separation of parasites from human blood using deterministic lateral displacement. *Lab on a Chip*, *11*(7), 1326-1332.

[20]   Choi, G., Nouri, R., Zarzar, L., & Guan, W. (2020). Microfluidic deformability-activated sorting of single particles. *Microsystems & Nanoengineering*, *6*(1), 1-9.

[21]   Hur, S. C., Henderson-MacLennan, N. K., McCabe, E. R., & Di Carlo, D. (2011). Deformability-based cell classification and enrichment using inertial microfluidics. *Lab on a Chip*, *11*(5), 912-920.

[22]   Zhao, Y., Zhao, X. T., Chen, D. Y., Luo, Y. N., Jiang, M., Wei, C., ... & Chen, J. (2014). Tumor cell characterization and classification based on cellular specific membrane capacitance and cytoplasm conductivity. *Biosensors and Bioelectronics*, *57*, 245-253.

[23]   Huang, Y., Joo, S., Duhon, M., Heller, M., Wallace, B., & Xu, X. (2002). Dielectrophoretic cell separation and gene expression profiling on microelectronic chip arrays. *Analytical chemistry*, *74*(14), 3362-3371.

[24] Hu, X., Bessette, P. H., Qian, J., Meinhart, C. D., Daugherty, P. S., & Soh, H. T. (2005). Marker-specific sorting of rare cells using dielectrophoresis. *Proceedings of the national academy of sciences*, *102*(44), 15757-15761.

[25] Alshareef, M., Metrakos, N., Juarez Perez, E., Azer, F., Yang, F., Yang, X., & Wang, G. (2013). Separation of tumor cells with dielectrophoresis-based microfluidic chip. *Biomicrofluidics*, *7*(1), 011803.

[26] Cheng, I. F. Chang, H. C., Hou, D., & Chang, H. C. (2007). An integrated dielectrophoretic chip for continuous bioparticle filtering, focusing, sorting, trapping, and detecting. *Biomicrofluidics*, *1*(2), 021503.

[27] Moon, H. S., Nam, Y. W., Park, J. C., & Jung, H. I. (2009). Dielectrophoretic separation of airborne microbes and dust particles using a microfluidic channel for real-time bioaerosol monitoring. *Environmental science & technology*, *43*(15), 5857-5863.

[28] Chen, C. A., Chen, C. H., Ghaemmaghami, A. M., & Fan, S. K. (2012, March). Separation of dendritic and T cells using electrowetting and dielectrophoresis. In *2012 7th IEEE International Conference on Nano/Micro Engineered and Molecular Systems (NEMS)* (pp. 183-186). IEEE.

[29] Cushing, K. W., Piyasena, M. E., Carroll, N. J., Maestas, G. C., López, B. A., Edwards, B. S., ... & López, G. P. (2013). Elastomeric negative acoustic contrast particles for affinity capture assays. *Analytical chemistry*, *85*(4), 2208-2215.

[30] Johnson, L. M., Gao, L., Shields IV, C. W., Smith, M., Efimenko, K., Cushing, K., ... & López, G. P. (2013). Elastomeric microparticles for acoustic mediated bioseparations. *Journal of nanobiotechnology*, *11*(1), 1-8.

[31] Li, P., Mao, Z., Peng, Z., Zhou, L., Chen, Y., Huang, P. H., ... & Huang, T. J. (2015). Acoustic separation of circulating tumor cells. *Proceedings of the National Academy of Sciences*, *112*(16), 4970-4975.

[32] Han, K. H., & Frazier, A. B. (2005). A microfluidic system for continuous magnetophoretic separation of suspended cells using their native magnetic properties. *Proc. Nanotech*, *1*, 187-190.

[33] Zola, H. (2006). Medical applications of leukocyte surface molecules—the CD molecules. *Molecular medicine*, *12*(11), 312-316.

[34] Dabelsteen, E., Mandel, U., & Clausen, H. (1991). Cell surface carbohydrates are markers of differentiation in human oral epithelium. *Critical Reviews in Oral Biology & Medicine*, *2*(4), 493-507.

[35] Bennett, S. R., Carbone, F. R., Karamalis, F., Flavell, R. A., Miller, J. F., & Heath, W. R. (1998). Help for cytotoxic-T-cell responses is mediated by CD40 signalling. *Nature*, *393*(6684), 478-480.

[36]   Han, J. S., & Nair, P. P. (1995). Flow cytometric identification of cell surface markers on cultured human colonic cell lines using monoclonal antibodies. *Cancer*, *76*(2), 195-200.

[37]   Krüger, J., Singh, K., O'Neill, A., Jackson, C., Morrison, A., & O'Brien, P. (2002). Development of a microfluidic device for fluorescence activated cell sorting. *Journal of micromechanics and microengineering*, *12*(4), 486.

[38]   Adams, J. D., Kim, U., & Soh, H. T. (2008). Multitarget magnetic activated cell sorter. *Proceedings of the National Academy of Sciences*, *105*(47), 18165-18170.

[39]   Hyun, K. A., & Jung, H. I. (2013). Microfluidic devices for the isolation of circulating rare cells: A focus on affinity-based, dielectrophoresis, and hydrophoresis. *Electrophoresis*, *34*(7), 1028-1041.

[40]   Kato, K., & Radbruch, A. (1993). Isolation and characterization of CD34+ hematopoietic stem cells from human peripheral blood by high-gradient magnetic cell sorting. *Cytometry: The Journal of the International Society for Analytical Cytology*, *14*(4), 384-392.

[41]   Smith, M. J., Culhane, A. C., Donovan, M., Coffey, J. C., Barry, B. D., Kelly, M. A., ... & Redmond, H. P. (2009). Analysis of differential gene expression in colorectal cancer and stroma using fluorescence-activated cell sorting purification. *British journal of cancer*, *100*(9), 1452-1464.

[42]   Fukuda, H., Takahashi, J., Watanabe, K., Hayashi, H., Morizane, A., Koyanagi, M., ... & Hashimoto, N. (2006). Fluorescence-Activated Cell Sorting–Based Purification of Embryonic Stem Cell–Derived Neural Precursors Averts Tumor Formation after Transplantation. *Stem cells*, *24*(3), 763-771.

[43]   Kjeldsen, M. K., Perez-Andres, M., Schmitz, A., Johansen, P., Boegsted, M., Nyegaard, M., ... & Dybkaer, K. (2011). Multiparametric flow cytometry for identification and fluorescence activated cell sorting of five distinct B-cell subpopulations in normal tonsil tissue. *American journal of clinical pathology*, *136*(6), 960-969.

[44]   Wang, G. Y., Li, Y., Yu, Y. M., Yu, B., Zhang, Z. Y., Liu, Y., & Wang, S. J. (2009). Detection of disseminated tumor cells in bone marrow of gastric cancer using magnetic activated cell sorting and fluorescent activated cell sorting. *Journal of gastroenterology and hepatology*, *24*(2), 299-306.

[45]   Mohr, F., Przibilla, S., Leonhardt, F., Stemberger, C., Dreher, S., Müller, T. R., ... & Busch, D. H. (2018). Efficient immunoaffinity chromatography of lymphocytes directly from whole blood. *Scientific reports*, *8*(1), 1-6.

[46]   Soares, R. R., Pettke, A., Robles-Remacho, A., Zeebaree, S., Ciftci, S., Tampere, M., ... & Madaboosi, N. (2021). Circle-to-circle amplification coupled with microfluidic affinity chromatography enrichment for in vitro molecular

diagnostics of Zika fever and analysis of anti-flaviviral drug efficacy. *Sensors and Actuators B: Chemical*, *336*, 129723.

[47]   Kurkuri, M. D., Al-Ejeh, F., Shi, J. Y., Palms, D., Prestidge, C., Griesser, H. J., ... & Thierry, B. (2011). Plasma functionalized PDMS microfluidic chips: towards point-of-care capture of circulating tumor cells. *Journal of Materials Chemistry*, *21*(24), 8841-8848.

[48]   Mitchell, M. J., Castellanos, C. A., & King, M. R. (2015). Immobilized surfactant-nanotube complexes support selectin-mediated capture of viable circulating tumor cells in the absence of capture antibodies. *Journal of Biomedical Materials Research Part A*, *103*(10), 3407-3418.

[49]   Stephens, A., Nidetz, R., Mesyngier, N., Chung, M. T., Song, Y., Fu, J., & Kurabayashi, K. (2019). Mass-producible microporous silicon membranes for specific leukocyte subset isolation, immunophenotyping, and personalized immunomodulatory drug screening in vitro. *Lab on a Chip*, *19*(18), 3065-3076.

[50]   Hosokawa, M., Arakaki, A., Takahashi, M., Mori, T., Takeyama, H., & Matsunaga, T. (2009). High-density microcavity array for cell detection: single-cell analysis of hematopoietic stem cells in peripheral blood mononuclear cells. *Analytical chemistry*, *81*(13), 5308-5313.

[51]   Yousuff, C. M., Ho, E. T. W., Hussain K, I., & Hamid, N. H. B. (2017). Microfluidic platform for cell isolation and manipulation based on cell properties. *Micromachines*, *8*(1), 15.

[52]   Zhang, C., Lv, X., Han, X., Man, Y., Saeed, Y., Qing, H., & Deng, Y. (2015). Whole-cell based aptamer selection for selective capture of microorganisms using microfluidic devices. *Analytical Methods*, *7*(15), 6339-6345.

[53]   Bussonnière, A., Miron, Y., Baudoin, M., Matar, O. B., Grandbois, M., Charette, P., & Renaudin, A. (2014). Cell detachment and label-free cell sorting using modulated surface acoustic waves (SAWs) in droplet-based microfluidics. *Lab on a Chip*, *14*(18), 3556-3563.

[54]   Karabacak, N. M., Spuhler, P. S., Fachin, F., Lim, E. J., Pai, V., Ozkumur, E., ... & Toner, M. (2014). Microfluidic, marker-free isolation of circulating tumor cells from blood samples. *Nature protocols*, *9*(3), 694-710.

[55]   Chu, C. H., Liu, R., Ozkaya-Ahmadov, T., Boya, M., Swain, B. E., Owens, J. M., ... & Sarioglu, A. F. (2019). Hybrid negative enrichment of circulating tumor cells from whole blood in a 3D-printed monolithic device. *Lab on a Chip*, *19*(20), 3427-3437.

[56]   Huang, R., Barber, T. A., Schmidt, M. A., Tompkins, R. G., Toner, M., Bianchi, D. W., ... & Flejter, W. L. (2008). A microfluidics approach for the isolation of nucleated red blood cells (NRBCs) from the peripheral blood of pregnant

women. *Prenatal Diagnosis: Published in Affiliation With the International Society for Prenatal Diagnosis*, *28*(10), 892-899.

[57]   Kim, U., & Soh, H. T. (2009). Simultaneous sorting of multiple bacterial targets using integrated Dielectrophoretic–Magnetic Activated Cell Sorter. *Lab on a Chip*, *9*(16), 2313-2318.

[58]   Chung, K., Crane, M. M., & Lu, H. (2008). Automated on-chip rapid microscopy, phenotyping and sorting of C. elegans. *Nature methods*, *5*(7), 637.

[59]   Robert, D., Pamme, N., Conjeaud, H., Gazeau, F., Iles, A., & Wilhelm, C. (2011). Cell sorting by endocytotic capacity in a microfluidic magnetophoresis device. *Lab on a chip*, *11*(11), 1902-1910.

[60]   Kuswandi, B., Huskens, J., & Verboom, W. (2007). Optical sensing systems for microfluidic devices: a review. *Analytica chimica acta*, *601*(2), 141-155.

[61]   Wu, J., & Gu, M. (2011). Microfluidic sensing: state of the art fabrication and detection techniques. *Journal of biomedical optics*, *16*(8), 080901.

[62]   Chung, B. G., Flanagan, L. A., Rhee, S. W., Schwartz, P. H., Lee, A. P., Monuki, E. S., & Jeon, N. L. (2005). Human neural stem cell growth and differentiation in a gradient-generating microfluidic device. *Lab on a Chip*, *5*(4), 401-406.

[63]   Gossett, D. R., Henry, T. K., Lee, S. A., Ying, Y., Lindgren, A. G., Yang, O. O., ... & Di Carlo, D. (2012). Hydrodynamic stretching of single cells for large population mechanical phenotyping. *Proceedings of the National Academy of Sciences*, *109*(20), 7630-7635.

[64]   Chaudhary, S., Lee, S. A., Li, Y., Patel, D. S., & Lu, H. (2021). Graphical-model framework for automated annotation of cell identities in dense cellular images. *Elife*, *10*, e60321.

[65]   Dénervaud, N., Becker, J., Delgado-Gonzalo, R., Damay, P., Rajkumar, A. S., Unser, M., ... & Maerkl, S. J. (2013). A chemostat array enables the spatio-temporal analysis of the yeast proteome. *Proceedings of the National Academy of Sciences*, *110*(39), 15842-15847.

[66]   Nobs, J. B., & Maerkl, S. J. (2014). Long-term single cell analysis of S. pombe on a microfluidic microchemostat array. *PloS one*, *9*(4), e93466.

[67]   Balagaddé, F. K., You, L., Hansen, C. L., Arnold, F. H., & Quake, S. R. (2005). Long-term monitoring of bacteria undergoing programmed population control in a microchemostat. *Science*, *309*(5731), 137-140.

[68]   Heo, Y. J., Lee, D., Kang, J., Lee, K., & Chung, W. K. (2017). Real-time image processing for microscopy-based label-free imaging flow cytometry in a microfluidic chip. *Scientific reports*, *7*(1), 1-9.

161

[69] Praljak, N., Iram, S., Goreke, U., Singh, G., Hill, A., Gurkan, U. A., & Hinczewski, M. (2020). Integrating deep learning with microfluidics for biophysical classification of sickle red blood cells. *bioRxiv.*

[70] Lin, S. W., Chang, C. H., & Lin, C. H. (2011). High-throughput fluorescence detections in microfluidic systems. Genomic Medicine, Biomarkers, and Health Sciences, 3(1), 27-38.

[71] Combs, C. A. (2010). Fluorescence microscopy: a concise guide to current imaging methods. *Current protocols in neuroscience*, *50*(1), 2-1.

[72] Götz, S., & Karst, U. (2007). Recent developments in optical detection methods for microchip separations. *Analytical and bioanalytical chemistry*, *387*(1), 183-192.

[73] Guo, L., Shi, Y., Liu, X., Han, Z., Zhao, Z., Chen, Y., ... & Li, X. (2018). Enhanced fluorescence detection of proteins using ZnO nanowires integrated inside microfluidic chips. *Biosensors and Bioelectronics*, *99*, 368-374.

[74] Challa, P. K., Peter, Q., Wright, M. A., Zhang, Y., Saar, K. L., Carozza, J. A., ... & Knowles, T. P. (2018). Real-time intrinsic fluorescence visualization and sizing of proteins and protein complexes in microfluidic devices. *Analytical chemistry*, *90*(6), 3849-3855.

[75] Dittrich, P. S., & Schwille, P. (2003). An integrated microfluidic system for reaction, high-sensitivity detection, and sorting of fluorescent cells and particles. *Analytical chemistry*, *75*(21), 5767-5774.

[76] Zhang, H., Xu, T., Li, C. W., & Yang, M. (2010). A microfluidic device with microbead array for sensitive virus detection and genotyping using quantum dots as fluorescence labels. *Biosensors and Bioelectronics*, *25*(11), 2402-2407.

[77] Shrinivasan, S., Norris, P. M., Landers, J. P., & Ferrance, J. P. (2007). A low-cost, low-power consumption, miniature laser-induced fluorescence system for DNA detection on a microfluidic device. *Clinics in laboratory medicine*, *27*(1), 173-181.

[78] Komatsu, Y., Nagaoka, R., Funamoto, K. I., Hayase, T., Masauzi, N., Kanai, H., & Saijo, Y. (2014, August). "Sonocytometry"—Novel diagnostic method of ultrasonic differentiation of cells in blood flow. In *2014 36th Annual International Conference of the IEEE Engineering in Medicine and Biology Society* (pp. 2761-2764). IEEE.

[79] Godber, B., Thompson, K. S., Rehak, M., Uludag, Y., Kelling, S., Sleptsov, A., ... & Cooper, M. A. (2005). Direct quantification of analyte concentration by resonant acoustic profiling. *Clinical Chemistry*, *51*(10), 1962-1972.

[80]   Galanzha, E. I., & Zharov, V. P. (2013). Circulating tumor cell detection and capture by photoacoustic flow cytometry in vivo and ex vivo. *Cancers*, *5*(4), 1691-1738.

[81]   McKinnon, K. M. (2018). Flow cytometry: an overview. *Current protocols in immunology*, *120*(1), 5-1.

[82]   Piyasena, M. E., & Graves, S. W. (2014). The intersection of flow cytometry with microfluidics and microfabrication. *Lab on a Chip*, *14*(6), 1044-1059.

[83]   Oakey, J., Applegate Jr, R. W., Arellano, E., Carlo, D. D., Graves, S. W., & Toner, M. (2010). Particle focusing in staged inertial microfluidic devices for flow cytometry. *Analytical chemistry*, *82*(9), 3862-3867.

[84]   Yu, C., Vykoukal, J., Vykoukal, D. M., Schwartz, J. A., Shi, L., & Gascoyne, P. R. (2005). A three-dimensional dielectrophoretic particle focusing channel for microcytometry applications. *Journal of Microelectromechanical Systems*, *14*(3), 480-487.

[85]   Mao, X., Lin, S. C. S., Dong, C., & Huang, T. J. (2009). Single-layer planar on-chip flow cytometer using microfluidic drifting based three-dimensional (3D) hydrodynamic focusing. *Lab on a Chip*, *9*(11), 1583-1589.

[86]   Tanaka, T., Saeki, T., Sunaga, Y., & Matsunaga, T. (2010). High-content analysis of single cells directly assembled on CMOS sensor based on color imaging. *Biosensors and Bioelectronics*, *26*(4), 1460-1465.

[87]   Jin, G., Yoo, I. H., Pack, S. P., Yang, J. W., Ha, U. H., Paek, S. H., & Seo, S. (2012). Lens-free shadow image based high-throughput continuous cell monitoring technique. *Biosensors and Bioelectronics*, *38*(1), 126-131.

[88]   Huang, X., Jiang, Y., Liu, X., Xu, H., Han, Z., Rong, H., ... & Yu, H. (2016). Machine learning based single-frame super-resolution processing for lensless blood cell counting. *Sensors*, *16*(11), 1836.

[89]   Fernandes, A. C., Duarte, C. M., Cardoso, F. A., Bexiga, R., Cardoso, S., & Freitas, P. P. (2014). Lab-on-chip cytometry based on magnetoresistive sensors for bacteria detection in milk. *Sensors*, *14*(8), 15496-15524.

[90]   Albuquerque, D. C., Martins, V. C., & Cardoso, S. (2019). Magnetoresistive Detection of Clinical Biomarker for Monitoring of Colorectal Cancer. *IEEE Magnetics Letters*, *10*, 1-5.

[91]   Loureiro, J., Ferreira, R., Cardoso, S., Freitas, P. P., Germano, J., Fermon, C., ... & Rivas, J. (2009). Toward a magnetoresistive chip cytometer: Integrated detection of magnetic beads flowing at cm/s velocities in microfluidic channels. *Applied Physics Letters*, *95*(3), 034104.

[92]   Figeys, D., Gygi, S. P., McKinnon, G., & Aebersold, R. (1998). An integrated microfluidics-tandem mass spectrometry system for automated protein analysis. *Analytical Chemistry*, *70*(18), 3728-3734.

[93]   Hardouin, J., Duchateau, M., Joubert-Caron, R., & Caron, M. (2006). Usefulness of an integrated microfluidic device (HPLC-Chip-MS) to enhance confidence in protein identification by proteomics. *Rapid Communications in Mass Spectrometry: An International Journal Devoted to the Rapid Dissemination of Up‑to‑the‑Minute Research in Mass Spectrometry*, *20*(21), 3236-3244.

[94]   Armenta, J. M., Dawoud, A. A., & Lazar, I. M. (2009). Microfluidic chips for protein differential expression profiling. *Electrophoresis*, *30*(7), 1145-1156.

[95]   Horvatovich, P., Govorukhina, N. I., Reijmers, T. H., van der Zee, A. G., Suits, F., & Bischoff, R. (2007). Chip-LC-MS for label-free profiling of human serum. *Electrophoresis*, *28*(23), 4493-4505.

[96]   DeBlois, R. W. & Bean, C. P. (1970). Counting and sizing of submicron particles by the resistive pulse technique. *Review of Scientific Instruments*, *41*(7), 909-916.

[97]   Sukhacheva, E. (2020). Comments re article on comparison of performance and abnormal cell flagging of two automated hematology analyzers: Sysmex XN 3000 and Beckman Coulter DxH 800. *International journal of laboratory hematology*, *42*(3), e96.

[98]   Ginsburg, E. & Vonderhaar, B. K. (1995). Prolactin synthesis and secretion by human breast cancer cells. *Cancer Research*, *55*(12), 2591-2595.

[99]   Kubitschek, H. E. & Friske, J. A. (1986). Determination of bacterial cell volume with the Coulter Counter. *Journal of bacteriology*, *168*(3), 1466-1467.

[100]   Wang, J., Sun, Y., Meng, X. Y., Li, L. F., Li, Y., Luo, Y., ... & Qiu, H. J. (2018). Comprehensive evaluation of the host responses to infection with differentially virulent classical swine fever virus strains in pigs. *Virus research*, *255*, 68-76.

[101]   Simiele, M., D'Avolio, A., Baietto, L., Siccardi, M., Sciandra, M., Agati, S., ... & Di Perri, G. (2011). Evaluation of the mean corpuscular volume of peripheral blood mononuclear cells of HIV patients by a coulter counter to determine intracellular drug concentrations. *Antimicrobial agents and chemotherapy*, *55*(6), 2976-2978.

[102]   Bezrukov, S. M., Vodyanoy, I., & Parsegian, V. A. (1994). Counting polymers moving through a single ion channel. *Nature*, *370*(6487), 279-281.

[103]   Arimi, M. M., (2018). Particle size distribution as an emerging tool for the analysis of wastewater. *Environmental Technology Reviews*, *7*(1), 274-290.

[104] Tsutsui, M., Hongo, S., He, Y., Taniguchi, M., Gemma, N., & Kawai, T. (2012). Single-nanoparticle detection using a low-aspect-ratio pore. *ACS nano*, *6*(4), 3499-3505.

[105] Adamo, A., Sharei, A., Adamo, L., Lee, B., Mao, S., & Jensen, K. F. (2012). Microfluidics-based assessment of cell deformability. *Analytical chemistry*, *84*(15), 6438-6443.

[106] De Ninno, A., Errico, V., Bertani, F. R., Businaro, L., Bisegna, P., & Caselli, F. (2017). Coplanar electrode microfluidic chip enabling accurate sheathless impedance cytometry. *Lab on a Chip*, *17*(6), 1158-1166.

[107] Branton, D., Deamer, D. W., Marziali, A., Bayley, H., Benner, S. A., Butler, T., ... & Schloss, J. A. (2010). The potential and challenges of nanopore sequencing. *Nanoscience and technology: A collection of reviews from Nature Journals*, 261-268.

[108] Sui, J., Gandotra, N., Xie, P., Lin, Z., Scharfe, C., & Javanmard, M. (2021). Multi-frequency impedance sensing for detection and sizing of DNA fragments. *Scientific reports*, *11*(1), 1-9.

[109] Li, W., Bell, N. A., Hernández-Ainsa, S., Thacker, V. V., Thackray, A. M., Bujdoso, R., & Keyser, U. F. (2013). Single protein molecule detection by glass nanopores. *ACS nano*, *7*(5), 4129-4134.

[110] Watkins, N. N., Hassan, U., Damhorst, G., Ni, H., Vaid, A., Rodriguez, W., & Bashir, R. (2013). Microfluidic CD4þ and CD8þ T lymphocyte counters for point-of-care HIV diagnostics using whole blood. Sci. Transl. Med. 5.

[111] Liu, R., Wang, N., Kamili, F., & Sarioglu, A. F. (2016). Microfluidic CODES: a scalable multiplexed electronic sensor for orthogonal detection of particles in microfluidic channels. *Lab on a Chip*, *16*(8), 1350-1357.

[112] Liu, R., Waheed, W., Wang, N., Civelekoglu, O., Boya, M., Chu, C. H., & Sarioglu, A. F. (2017). Design and modeling of electrode networks for code-division multiplexed resistive pulse sensing in microfluidic devices. *Lab on a Chip*, *17*(15), 2650-2666.

[113] Wang, N., Liu, R., & Sarioglu, A. F. (2017). Microfluidic platform with multiplexed electronic detection for spatial tracking of particles. *Journal of visualized experiments: JoVE*, (121), 55311.

[114] Duel-Hallen, A., Holtzman, J., & Zvonar, Z. (1995). Multiuser detection for CDMA systems. *IEEE personal communications*, *2*(2), 46-58.

[115] Wang, N., Liu, R., Khodambashi, R., Asmare, N., & Sarioglu, A. F. (2017, January). Code-division multiplexed resistive pulse sensor networks for spatio-temporal detection of particles in microfluidic devices. In *2017 IEEE 30th*

International Conference on Micro Electro Mechanical Systems (MEMS) (pp. 362-365). IEEE.

[116] Wang, N., Liu, R., Asmare, N., Chu, C. H., & Sarioglu, A. F. (2021). Integrated sensor networks with error correction for multiplexed particle tracking in microfluidic chips. *Biosensors and Bioelectronics*, *174*, 112818.

[117] Wang. N., Liu, R., Asmare, N., Chu, C. H., & Sarioglu, A. F. (2019). Processing code-multiplexed Coulter signals via deep convolutional neural networks. *Lab on a Chip*, *19*(19), 3292-3304.

[118] Wang, N., Liu, R., Asmare, N., Anandakumar, D. B., & Sarioglu, A. F. (2019, June). Decoding of Code-Multiplexed Coulter Sensor Signals via Deep Learning. In *2019 20th International Conference on Solid-State Sensors, Actuators and Microsystems & Eurosensors XXXIII (TRANSDUCERS & EUROSENSORS XXXIII)* (pp. 202-205). IEEE.

[119] Wang, N., Liu, R., & Sarioglu, A. F. (2018, November). CONVOLUTIONAL NEURAL NETWORK BASED PROCESSING OF CODE-MULTIPLEXED COULTER SIGNALS. In *Proc. 22nd International Conference on Miniaturized Systems for Chemistry and Life Sciences*.

[120] Wang, N., Liu, R., & Sarioglu, A. F. (2018, November). CODE-MULTIPLEXED SENSOR NETWORKS FOR MICROFLUIDIC IMPEDANCE SPECTROSCOPY. In *Proc. 22nd International Conference on Miniaturized Systems for Chemistry and Life Sciences*.

[121] Wang, N., Liu, R., Asmare, N., Chu, C. H., Civelekoglu, O., & Sarioglu, A. F. (2021). Closed-loop Feedback Control of Microfluidic Cell Manipulation via Deep-learning Integrated Sensor Networks. *Lab on a Chip*.

[122] Whitesides, G. M. (2006). The origins and the future of microfluidics. *nature*, *442*(7101), 368-373.

[123] Sato, K., Tanaka, Y., Renberg, B., & Kitamori, T. (2009). Combining microchip and cell technology for creation of novel biodevices. *Analytical and bioanalytical chemistry*, *393*(1), 23-29.

[124] Dressaire, E., & Sauret, A. (2017). Clogging of microfluidic systems. *Soft Matter*, *13*(1), 37-48.Kim, S., Kim, K. C., and Yeom, E., *Opt. Lasers Eng.*, 104, 237-243 (2018).

[125] Asmare, N., Arifuzzman, A. K. M., Wang, N., Boya, M., Liu, R., & Sarioglu, A. F. (2019, June). High Throughput Cell Mechanophenotyping via Microfluidic Constrictions with Multiplexed Electrical Sensors. In *2019 20th International Conference on Solid-State Sensors, Actuators and Microsystems & Eurosensors XXXIII (TRANSDUCERS & EUROSENSORS XXXIII)* (pp. 948-951). IEEE.

[126] Liu, R., Chu, C. H., Wang, N., Ozkaya-Ahmadov, T., Civelekoglu, O., Lee, D., ... & Sarioglu, A. F. (2019). Immunophenotyping: Combinatorial Immunophenotyping of Cell Populations with an Electronic Antibody Microarray (Small 51/2019). *Small*, *15*(51), 1970275.

[127] Liu, R., Arifuzzman, A. K. M., Wang, N., Civelekoglu, O., & Sarioglu, A. F. (2020). Electronic Immunoaffinity Assay for Differential Leukocyte Counts. *Journal of Microelectromechanical Systems*, *29*(5), 942-947.

[128] Liu, R., Chu, C. H., Wang, N., & Sarioglu, A. F. (2018, November). MICROFLUIDIC ANTIBODY MICROARRAY WITH AN ELECTRONIC READOUT FOR COMBINATORIAL IMMUNOPHENOTYPING OF CELL POPULATIONS. In *Proc. 22nd International Conference on Miniaturized Systems for Chemistry and Life Sciences*.

[129] Civelekoglu, O., Wang, N., Boya, M., Ozkaya-Ahmadov, T., Liu, R., & Sarioglu, A. F. (2019). Electronic profiling of membrane antigen expression via immunomagnetic cell manipulation. *Lab on a Chip*, *19*(14), 2444-2455.

[130] Civelekoglu, O., Liu, R., Boya, M., Chu, C. H., Wang, N., & Sarioglu, A. F. (2017, June). A microfluidic device for electronic cell surface expression profiling using magnetophoresis. In *2017 19th International Conference on Solid-State Sensors, Actuators and Microsystems (TRANSDUCERS)* (pp. 480-483). IEEE.

[131] Civelekoglu, O., Wang, N., Boya, M., Ozkaya-Ahmadov, T., Liu, R., & Sarioglu, A. F. (2019, June). Quantitative Measurement of Cell Surface Expression Via Magnetophoretic Cytometry. In *2019 20th International Conference on Solid-State Sensors, Actuators and Microsystems & Eurosensors XXXIII (TRANSDUCERS & EUROSENSORS XXXIII)* (pp. 975-978). IEEE.

[132] Civelekoglu, O., Wang, N., Boya, M., Ozkaya-Ahmadov, T., Liu, R., & Sarioglu, A. F. (2018, November). HIGH DYNAMIC RANGE ELECTRICAL PROFILING OF SURFACE EXPRESSION VIA FLOW-RATE-MODULATED-MAGNETOPHORESIS. In *Proc. 22nd International Conference on Miniaturized Systems for Chemistry and Life Sciences*.

[133] Weinstein, S. & Ebert, P. (1971). Data transmission by frequency-division multiplexing using the discrete Fourier transform. *IEEE transactions on Communication Technology*, *19*(5), 628-634.

[134] Spirit, D. M., Ellis, A. D., & Barnsley, P. E. (1994). Optical time division multiplexing: Systems and networks. *IEEE Communications Magazine*, *32*(12), 56-62.

[135] Jagtiani, A. V., Carletta, J., & Zhe, J. (2011). A microfluidic multichannel resistive pulse sensor using frequency division multiplexing for high throughput counting of micro particles. *Journal of Micromechanics and Microengineering*, *21*(6), 065004.

[136] Slimane, M. B., Hafaiedh, I. B., & Robbana, R. (2017). Formal-based design and verification of SoC arbitration protocols: A comparative analysis of TDMA and round-robin. *IEEE Design & Test*, *34*(5), 54-62.

[137] Salonidis, T., & Tassiulas, L. (2004). Asynchronous TDMA ad hoc networks: Scheduling and Performance. *European transactions on telecommunications*, *15*(4), 391-403.

[138] Choi, G., Murphy, E., & Guan, W. (2019). Microfluidic Time-Division Multiplexing Accessing Resistive Pulse Sensor for Particle Analysis. *ACS sensors*, *4*(7), 1957-1963.

[139] Cimini, L. (1985). Analysis and simulation of a digital mobile channel using orthogonal frequency division multiplexing. *IEEE transactions on communications*, *33*(7), 665-675.

[140] Ciciora, W. S., Ciciora, W., Large, D., Adams, M., & Farmer, J. (2004). *Modern cable television technology*. Morgan Kaufmann.

[141] Attar, A., Holland, O., Nakhai, M. R., & Aghvami, A. H. (2008). Interference-limited resource allocation for cognitive radio in orthogonal frequency-division multiplexing networks. *IET communications*, *2*(6), 806-814.

[142] Mollah, M. B., & Islam, M. R. (2012, January). Comparative analysis of Gold Codes with PN codes using correlation property in CDMA technology. In *2012 International Conference on Computer Communication and Informatics* (pp. 1-6). IEEE.

[143] Tsai, S. H., Lin, Y. P., & Kuo, C. C. (2006). MAI-free MC-CDMA systems based on Hadamard–Walsh codes. *IEEE Transactions on Signal Processing*, *54*(8), 3166-3179.

[144] Tseng, S. M., Zheng, Y., Hsu, Y. T., & Chang, M. C. (2002, April). Fuzzy adaptive parallel interference cancellation and vector channel prediction for CDMA in fading channels. In *2002 IEEE International Conference on Communications. Conference Proceedings. ICC 2002 (Cat. No. 02CH37333)* (Vol. 1, pp. 252-256). IEEE.

[145] Sheikh, A. U., Ali, M. A., & Zerguine, A. (2013). Adaptive Successive Interference Cancelation Using Fuzzy Derived Weights. *Arabian Journal for Science and Engineering*, *38*(8), 2179-2187.

[146] Cho, J., Good, P., Kamat, M., McCarthy, E., Rampmeier, K., Cops, W., ... & Lloyd, S. (2003, June). A dual-band tri-mode CDMA IF receiver with programmable channel-match filter. In *IEEE Radio Frequency Integrated Circuits (RFIC) Symposium, 2003* (pp. 391-394). IEEE.

[147] Patel, P., & Holtzman, J. (1994). Analysis of a simple successive interference cancellation scheme in a DS/CDMA system. *IEEE journal on selected areas in communications*, *12*(5), 796-807.

[148] Shibano, T., Lizuka, K., Miyamoto, M., Osaka, M., Miyama, R., & Kito, A. (1997, February). Matched filter for DS-CDMA of up to 50 MChip/s based on sampled analog signal processing. In *1997 IEEE International Solids-State Circuits Conference. Digest of Technical Papers* (pp. 100-101). IEEE.

[149] Cardoso, J. F. (1998). Blind signal separation: statistical principles. *Proceedings of the IEEE*, *86*(10), 2009-2025.

[150] Kitamura, D., Ono, N., Sawada, H., Kameoka, H., & Saruwatari, H. (2018). Determined blind source separation with independent low-rank matrix analysis. In *Audio source separation* (pp. 125-155). Springer, Cham.

[151] Wang, Y. & Guo, Y. (2019). A hierarchical independent component analysis model for longitudinal neuroimaging studies. *NeuroImage*, *189*, 380-400.

[152] Mejia, A. F., Yue, Y., Bolin, D., Lindgren, F., & Lindquist, M. A. (2020). A Bayesian general linear modeling approach to cortical surface fMRI data analysis. *Journal of the American Statistical Association*, *115*(530), 501-520.

[153] Lukemire, J., Wang, Y., Verma, A., & Guo, Y. (2020). HINT: A hierarchical independent component analysis toolbox for investigating brain functional networks using neuroimaging data. *Journal of neuroscience methods*, *341*, 108726.

[154] Zavala-Fernández, H., Sander, T. H., Burghoff, M., Orglmeister, R., & Trahms, L. (2006, March). Comparison of ICA algorithms for the isolation of biological artifacts in magnetoencephalography. In *International Conference on Independent Component Analysis and Signal Separation* (pp. 511-518). Springer, Berlin, Heidelberg.

[155] Oja, E., Kiviluoto, K., & Malaroiu, S. (2000, October). Independent component analysis for financial time series. In *Proceedings of the IEEE 2000 Adaptive Systems for Signal Processing, Communications, and Control Symposium (Cat. No. 00EX373)* (pp. 111-116). IEEE.

[156] Han, X. H., Chen, Y. W., Nakao, Z., & Lu, H. (2003, September). ICA-domain filtering of Poisson noise images. In *Third International Symposium on Multispectral Image Processing and Pattern Recognition* (Vol. 5286, pp. 811-814). International Society for Optics and Photonics.

[157] Rao, C. R. (1964). The use and interpretation of principal component analysis in applied research. *Sankhyā: The Indian Journal of Statistics, Series A*, 329-358.

[158] Mudrova, M., & Procházka, A. (2005, November). Principal component analysis in image processing. In *Proceedings of the MATLAB technical computing conference, Prague.*

[159] Back, A. D., & Weigend, A. S. (1997). A first application of independent component analysis to extracting structure from stock returns. *International journal of neural systems*, *8*(04), 473-484.

[160] López, M., Ramírez, J., Górriz, J. M., Álvarez, I., Salas-Gonzalez, D., Segovia, F., ... & Alzheimer's Disease Neuroimaging Initiative. (2011). Principal component analysis-based techniques and supervised classification schemes for the early detection of Alzheimer's disease. *Neurocomputing*, *74*(8), 1260-1271.

[161] Gerbrands, J. J. (1981). On the relationships between SVD, KLT and PCA. *Pattern recognition*, *14*(1-6), 375-381.

[162] Lee, D. D., & Seung, H. S. (1999). Learning the parts of objects by non-negative matrix factorization. *Nature*, *401*(6755), 788-791.

[163] Guillamet, D., Vitria, J., & Schiele, B. (2003). Introducing a weighted non-negative matrix factorization for image classification. *Pattern Recognition Letters*, *24*(14), 2447-2454.

[164] Pauca, V. P., Shahnaz, F., Berry, M. W., & Plemmons, R. J. (2004, April). Text mining using non-negative matrix factorizations. In *Proceedings of the 2004 SIAM International Conference on Data Mining* (pp. 452-456). Society for Industrial and Applied Mathematics.

[165] Wang, B., & Plumbley, M. D. (2005, July). Musical audio stream separation by non-negative matrix factorization. In *Proc. DMRN summer conf* (pp. 23-24).

[166] Hu, Y. H., Tompkins, W. J., Urrusti, J. L., & Afonso, V. X. (1993). Applications of artificial neural networks for ECG signal detection and classification. *Journal of electrocardiology*, *26*, 66-73.

[167] Srinivasan, V., Eswaran, C., & Sriraam, N. (2007). Approximate entropy-based epileptic EEG detection using artificial neural networks. *IEEE Transactions on information Technology in Biomedicine*, *11*(3), 288-295.

[168] Arunkumar, N., Mohammed, M. A., Mostafa, S. A., Ibrahim, D. A., Rodrigues, J. J., & de Albuquerque, V. H. C. (2020). Fully automatic model-based segmentation and classification approach for MRI brain tumor using artificial neural networks. *Concurrency and Computation: Practice and Experience*, *32*(1), e4962.

[169] Sánchez-Reolid, R., García, A. S., Vicente-Querol, M. A., Fernández-Aguilar, L., López, M. T., Fernández-Caballero, A., & González, P. (2018). Artificial neural

networks to assess emotional states from brain-computer interface. *Electronics*, *7*(12), 384.

[170] Bo, X., Guo-lin, L., Jing-jing, X., & Jing, Y. (2006, October). Blind Signal Separation Based on Feed-forward and Feedback Neural Network. In *2006 CIE International Conference on Radar* (pp. 1-4). IEEE.

[171] Côté-Allard, U., Fall, C. L., Drouin, A., Campeau-Lecours, A., Gosselin, C., Glette, K., ... & Gosselin, B. (2019). Deep learning for electromyographic hand gesture signal classification using transfer learning. *IEEE Transactions on Neural Systems and Rehabilitation Engineering*, *27*(4), 760-771.

[172] Bodapati, J. D., Veeranjaneyulu, N., Shareef, S. N., Hakak, S., Bilal, M., Maddikunta, P. K. R., & Jo, O. (2020). Blended multi-modal deep convnet features for diabetic retinopathy severity prediction. *Electronics*, *9*(6), 914.

[173] Ross-Howe, S., & Tizhoosh, H. R. (2019, May). Atrial Fibrillation Detection Using Deep Features and Convolutional Networks. In *2019 IEEE EMBS International Conference on Biomedical & Health Informatics (BHI)* (pp. 1-4). IEEE.

[174] Chandna, P., Miron, M., Janer, J., & Gómez, E. (2017, February). Monoaural audio source separation using deep convolutional neural networks. In *International conference on latent variable analysis and signal separation* (pp. 258-266). Springer, Cham.

[175] Simpson, A. J., Roma, G., & Plumbley, M. D. (2015, August). Deep karaoke: Extracting vocals from musical mixtures using a convolutional deep neural network. In *International Conference on Latent Variable Analysis and Signal Separation* (pp. 429-436). Springer, Cham.

[176] Salloum, R., & Kuo, C. C. J. (2017, March). ECG-based biometrics using recurrent neural networks. In *2017 IEEE International Conference on Acoustics, Speech and Signal Processing (ICASSP)* (pp. 2062-2066). IEEE.

[177] Übeyli, E. D. (2009). Combining recurrent neural networks with eigenvector methods for classification of ECG beats. *Digital Signal Processing*, *19*(2), 320-329.

[178] Kumar, S. D., & Subha, D. P. (2019, April). Prediction of depression from EEG signal using long short term memory (LSTM). In *2019 3rd International Conference on Trends in Electronics and Informatics (ICOEI)* (pp. 1248-1253). IEEE.

[179] Vidyaratne, L., Glandon, A., Alam, M., & Iftekharuddin, K. M. (2016, July). Deep recurrent neural network for seizure detection. In *2016 International Joint Conference on Neural Networks (IJCNN)* (pp. 1202-1207). IEEE.

[180] Michielli, N., Acharya, U. R., & Molinari, F. (2019). Cascaded LSTM recurrent neural network for automated sleep stage classification using single-channel EEG signals. *Computers in biology and medicine*, *106*, 71-81.

[181] Luo, Y., Chen, Z., & Yoshioka, T. (2020, May). Dual-path rnn: efficient long sequence modeling for time-domain single-channel speech separation. In *ICASSP 2020-2020 IEEE International Conference on Acoustics, Speech and Signal Processing (ICASSP)* (pp. 46-50). IEEE.

[182] Li, C., Luo, Y., Han, C., Li, J., Yoshioka, T., Zhou, T., ... & Chen, Z. (2021, January). Dual-Path RNN for Long Recording Speech Separation. In *2021 IEEE Spoken Language Technology Workshop (SLT)* (pp. 865-872). IEEE.

[183] Tan, K., Xu, B., Kumar, A., Nachmani, E., & Adi, Y. (2020). SAGRNN: Self-Attentive Gated RNN for Binaural Speaker Separation with Interaural Cue Preservation. *IEEE Signal Processing Letters*.

[184] Hu, W., Liu, R., Lin, X., Li, Y., Zhou, X., & He, X. (2017, November). A deep learning method to estimate independent source number. In *2017 4th International Conference on Systems and Informatics (ICSAI)* (pp. 1055-1059). IEEE.

[185] Wang, D., & Chen, J. (2018). Supervised speech separation based on deep learning: An overview. *IEEE/ACM Transactions on Audio, Speech, and Language Processing*, *26*(10), 1702-1726.

[186] Drossos, K., Magron, P., Mimilakis, S. I., & Virtanen, T. (2018, September). Harmonic-percussive source separation with deep neural networks and phase recovery. In *2018 16th International Workshop on Acoustic Signal Enhancement (IWAENC)* (pp. 421-425). IEEE.

[187] Fan, Q., Yang, J., Hua, G., Chen, B., & Wipf, D. (2017). A generic deep architecture for single image reflection removal and image smoothing. In *Proceedings of the IEEE International Conference on Computer Vision* (pp. 3238-3247).

[188] Toner, M. & Irimia, D. (2005). Blood-on-a-chip. *Annu. Rev. Biomed. Eng.*, *7*, 77-103.

[189] Zborowski, M. & Chalmers, J. J. (2011). Rare cell separation and analysis by magnetic sorting, *Analytical chemistry*, 83 (21), 8050-8056.

[190] Yu, M., Stott, S., Toner, M., Maheswaran, S., & Haber, D. A. (2011). Circulating tumor cells: approaches to isolation and characterization. *Journal of Cell Biology*, *192*(3), 373-382.

[191] Gold, R., (1967). Optimal binary sequences for spread spectrum multiplexing (Corresp.). *IEEE Transactions on information theory*, *13*(4), 619-621.

[192] Liu, R., Wang, N., Chu, C. H., & Sarioglu, A. F. (2017, June). The effect of the electrode resistance on the performance of code-multiplexed resistive pulse sensing. In *2017 19th International Conference on Solid-State Sensors, Actuators and Microsystems (TRANSDUCERS)* (pp. 2115-2118). IEEE.

[193] Liu, R. Wang, N., Asmare, N., & Sarioglu, A. F. (2018). Scaling code-multiplexed electrode networks for distributed Coulter detection in microfluidics. *Biosensors and Bioelectronics*, *120*, 30-39.

[194] Liu, R., Wang, N., & Sarioglu, A. F. (2018, November). BIT ERROR RATE ANALYSIS OF CODE-MULTIPLEXED COULTER SENSOR NETWORKS. In *Proc. 22nd International Conference on Miniaturized Systems for Chemistry and Life Sciences.*

[195] Hamming, R.W., (1950). Error detecting and error correcting codes. *The Bell system technical journal*, *29*(2), 147-160.

[196] Tasadduq, B., Lam, W., Alexeev, A., Sarioglu, A. F., & Sulchek, T. (2017). Enhancing size based size separation through vertical focus microfluidics using secondary flow in a ridged microchannel. *Scientific reports*, *7*(1), 1-10.

[197] Bezdek, J. C., Chuah, S. K., & Leep, D. (1986). Generalized k-nearest neighbor rules. *Fuzzy Sets and Systems*, *18*(3), 237-256.

[198] Zhou, J., Kondylis, P., Haywood, D. G., Harms, Z. D., Lee, L. S., Zlotnick, A., & Jacobson, S. C. (2018). Characterization of virus capsids and their assembly intermediates by multicycle resistive-pulse sensing with four pores in series. *Analytical chemistry*, *90*(12), 7267-7274.

[199] Liu, Z., Zhu, D., Rodrigues, S. P., Lee, K. T., & Cai, W. (2018). Generative model for the inverse design of metasurfaces. *Nano letters*, *18*(10), 6570-6576.

[200] Liu, W., Anguelov, D., Erhan, D., Szegedy, C., Reed, S., Fu, C. Y., & Berg, A. C. (2016, October). Ssd: Single shot multibox detector. In *European conference on computer vision* (pp. 21-37). Springer, Cham.

[201] Chen, M., Hao, Y., Hwang, K., Wang, L., & Wang, L. (2017). Disease prediction by machine learning over big data from healthcare communities. *Ieee Access*, *5*, 8869-8879.

[202] LeCun, Y., Bengio, Y., & Hinton, G. (2015). Deep learning. *nature*, *521*(7553), 436-444.

[203] Ignatov, A., (2018). Real-time human activity recognition from accelerometer data using Convolutional Neural Networks. *Applied Soft Computing*, *62*, 915-922.

[204] Kiranyaz, S., Ince, T., & Gabbouj, M. (2015). Real-time patient-specific ECG classification by 1-D convolutional neural networks. *IEEE Transactions on Biomedical Engineering*, *63*(3), 664-675.

[205] Zhang, Y., Chan, W., & Jaitly, N. (2017, March). Very deep convolutional networks for end-to-end speech recognition. In *2017 IEEE International Conference on Acoustics, Speech and Signal Processing (ICASSP)* (pp. 4845-4849). IEEE.

[206] Tang, L., Tian, Y., & Pardalos, P. M. (2019). A novel perspective on multiclass classification: Regular simplex support vector machine. *Information Sciences*, *480*, 324-338.

[207] Murugan, P., (2018). Implementation of deep convolutional neural network in multi-class categorical image classification. *arXiv preprint arXiv:1801.01397*.

[208] Jones, D. R., Schonlau, M., & Welch, W. J. (1998). Efficient global optimization of expensive black-box functions. *Journal of Global optimization*, *13*(4), 455-492.

[209] Li, C., Zhang, K., Wang, X., Zhang, J., Liu, H., & Zhou, J. (2018). Feedback control system for large scale 2D digital microfluidic platforms. *Sensors and Actuators B: Chemical*, *255*, 3616-3622.

[210] Miller, E., Rotea, M., & Rothstein, J. P. (2010). Microfluidic device incorporating closed loop feedback control for uniform and tunable production of micro-droplets. *Lab on a Chip*, *10*(10), 1293-1301.

[211] Kim, Y., Lee, K. S., Kim, Y. E., Lee, K. J., Lee, S. H., Kim, T. S., & Kang, J. Y. (2009). Rapid exchange of oil-phase in microencapsulation chip to enhance cell viability. *Lab on a Chip*, *9*(9), 1294-1297.

[212] Soenksen, L. R., Kassis, T., Noh, M., Griffith, L. G., & Trumper, D. L. (2018). Closed-loop feedback control for microfluidic systems through automated capacitive fluid height sensing. *Lab on a Chip*, *18*(6), 902-914.

[213] Lake, J. R., Heyde, K. C., & Ruder, W. C. (2017). Low-cost feedback-controlled syringe pressure pumps for microfluidics applications. *PLoS One*, *12*(4), e0175089.

[214] Lao, A. I. , Lee, T. M., Hsing, I. M., & Ip, N. Y. (2000). Precise temperature control of microfluidic chamber for gas and liquid phase reactions. *Sensors and Actuators A: Physical*, *84*(1-2), 11-17.

[215] Cladé, P., (2018). PyDAQmx: a Python interface to the National Instruments DAQmx driver. *URL http://pythonhosted. org/PyDAQmx*.

[216] Ang, K. H., Chong, G., & Li, Y. (2005). PID control system analysis, design, and technology. *IEEE transactions on control systems technology*, *13*(4), 559-576.

[217] Backer, J. A., Lowe, C. P., Hoefsloot, H. C. J., & Iedema, P. D. (2005). Poiseuille flow to measure the viscosity of particle model fluids. *The Journal of chemical physics*, *122*(15), 154503.

[218] Maul, T. M., Chew, D. W., Nieponice, A., & Vorp, D. A. (2011). Mechanical stimuli differentially control stem cell behavior: morphology, proliferation, and differentiation. *Biomechanics and modeling in mechanobiology*, *10*(6), 939-953.

[219] Li, X., Dao, M., Lykotrafitis, G., & Karniadakis, G. E. (2017). Biomechanics and biorheology of red blood cells in sickle cell anemia. *Journal of biomechanics*, *50*, 34-41.

[220] Bhoola, S. & Hoskins, W. J. (2006). Diagnosis and management of epithelial ovarian cancer. *Obstetrics & Gynecology*, *107*(6), 1399-1410.

[221] Zhou, Y., Yang, D., Zhou, Y., Khoo, B. L., Han, J., & Ai, Y. (2018). Characterizing deformability and electrical impedance of cancer cells in a microfluidic device. *Analytical chemistry*, *90*(1), 912-919.

[222] Lekka, M., (2016). Discrimination between normal and cancerous cells using AFM. *Bionanoscience*, *6*(1), 65-80.

[223] Huang, N. T., Chen, W., Oh, B. R., Cornell, T. T., Shanley, T. P., Fu, J., & Kurabayashi, K. (2012). An integrated microfluidic platform for in situ cellular cytokine secretion immunophenotyping. *Lab on a Chip*, *12*(20), 4093-4101.

[224] Ozkumur, E., Shah, A. M., Ciciliano, J. C., Emmink, B. L., Miyamoto, D. T., Brachtel, E., ... & Toner, M. (2013). Inertial focusing for tumor antigen–dependent and–independent sorting of rare circulating tumor cells. *Science translational medicine*, *5*(179), 179ra47-179ra47.

[225] Pamme, N. & Wilhelm, C. (2006). Continuous sorting of magnetic cells via on-chip free-flow magnetophoresis. *Lab on a Chip*, *6*(8), 974-980.

[226] McCloskey, K. E., Chalmers, J. J., & Zborowski, M. (2000). Magnetophoretic mobilities correlate to antibody binding capacities. *Cytometry: The Journal of the International Society for Analytical Cytology*, *40*(4), 307-315.